Australian Government
Department of Agriculture

RMIT UNIVERSITY

mla
MEAT & LIVESTOCK AUSTRALIA

final report

Project code:	B.CCH.6220
Prepared by:	Prof. Kourosh Kalantar-zadeh
	RMIT University
Date published:	August 2015
ISBN:	9781741919417

PUBLISHED BY
Meat & Livestock Australia Limited
Locked Bag 991
NORTH SYDNEY NSW 2059

Development of gas selective membranes for intra-ruminal capsules

Meat & Livestock Australia acknowledges the matching funds provided by the Australian Government to support the research and development detailed in this publication.

Acknowledgements

We would like to thank Prof. Kourosh Kalantar-zadeh, Prof. Andy Ball, Dr. Chris McSweeney, Dr. Julian Hill, Dr. Jian Zhen Ou, Dr. Eric Adetutu, Mr. Kyle Berean, Dr. Majid Nour, Mr. Nam Ha, Mr. Asaf Robart, Dr. Leslie Overs, Dr. David Paull, Dr. Philip Valencia, Dr. Greg Bishop-Hurley, Dr. Jess Mcleod and Dr. Peter Moate for their contribution to this project.

Executive summary

In this project, nanostructured gas selective membranes for intra-ruminal capsules, as well as for protecting any field gas sensing measurement systems, were successfully developed. These membranes incorporated nanomaterials including multiwall carbon nanotubes (MWCNT), graphene nanosheets, molybdenum disulphide (MoS_2) nanosheets and silver (Ag) nanoparticles as the nanofillers into porous polymeric metrics. Their morphological and structural properties were comprehensively investigated and they were tuned to adjust their permeation properties towards important enteric gases for carbon farming including methane (CH_4), carbon dioxide (CO_2) hydrogen (H_2) and hydrogen disulphide (H_2S). Additionally, we successfully demonstrated that the addition of catalytic nanomaterials such as Ag could efficiently slow microbial growth on the surface of membranes and increase their longevity in the rumen environment. Altogether, our developed nanocomposite membranes proved to be ideal candidates for improving the measurement accuracy and extending the operation life of intra-ruminal capsules in the harsh rumen environment. We also fully investigated membranes in rumen liquid both *ex situ* and *in situ* using which we were able to associate the type and number of microbial consortia to CH_4production.It is envisaged that these *ex situ* and *in situ* gas measurement systems with their embedded membranes, developed in this project, will be further expanded for ruminants, and also be utilised for human healthcare and medical sectors. We are now pursuing commercialisation pathways, which shouldpotentially help in mitigating CH_4 effect in farming sectors.

Table of Contents

1. Background

Reducing methane emissions is a major priority in the “Carbon Farming Futures - Filling the Research Gap” program. The first step in addressing methane emission from ruminants is to develop an accurate, selective and reliable procedure for measurement of the gas, especially in animals under normal grazing conditions. This project is designed to develop membranes for an intra-ruminal capsule used to measure changes over time in the concentrations of gases released from the stomach of animals. The membranes developed need rapid permeability to methane, carbon dioxide and hydrogen, while restricting the permeability of hydrogen sulphide which can corrode the gas sensing devices within the capsule. Colonisation of the capsule membranes with microorganisms within the rumen may also alter their permeability to gases. Thus, a second objective of the project is to use bioinformatic analysis of the microbial community adhering to the membranes and within the rumen to allow real-time assessment of the activity and diversity of those microbial communities. Microbes adhering to the membranes may alter their functionality while identifying microbial types within the rumen may assist identifying those responsible for producing a quantified level of methane.

Carbon farming requirements for reducing methane emissions are specific to the measurement condition and environment. The commercial methane gas sensing systems currently available suffer from low measurement range for rumen gas constituent measurements, lack of compatibility with rumen environment and/or are expensive. The project is also identifying and using cheap, small gas measuring devices that can be held within the intra-ruminal capsule. A digital microchip and appropriate software has been developed in a collaborating project to allow information from these gas measuring devices to be recorded remotely from the animal.

It is also imperative that the microbial community associated with methanogenesis is sampled at the time of measurement to enable the methane production levels to be directly linked to the microbial community. Through the use of metagenomics and subsequent bioinformatic analyses for the first time the microbial community can be directly linked to methane production. This project addresses such requirements by developing selective and sensitive polymeric/nanomaterial composite membranes to methane gas and coupling this with metagenomic analysis of the microbial community. This low cost and reliable sensor coupled to metagenomic analysis will allow successful assessment and eventually management of the target gas species.

Methane gas mitigation requires the coupling of *in situ* (e.g. inside the rumen) and *ex situ* (e.g. in the field) methane measurement and microbial analyses. No commercial methane gas sensor has been customised for optimum continuous sensing of the gas released from the rumen of animals. In this project, low cost polymeric/nanomaterial composite membranes, which are based on MWCNT, graphene nanosheets, MoS_2 nanosheets and Ag nanoparticles, were successfully developed to tackle the challenges of sensing systems in order to (1) the selectivity to specific gases in the methane gas measurement environment and (2) the diffusion rates of specific gases, and (3) allow simultaneous sampling for microbial analyses.

2. Methodology

2.1. Development of nanocomposite membranes

2.1.1 MWCNT-PDMS nanocomposite membranes

PDMS (Sylgard 184, Dow Corning Corporation) and MWCNT with outer diameter of 20–40 nm and length of 10–30 µm (Cheap Tubes, Inc.) were utilised. Beside pure PDMS membrane, three different MWCNT-PDMS nanocomposite membranes were prepared with MWCNT weight percentages including 1%, 5%, and 10%. First, MWCNT’s were dispersed in toluene, to facilitate effective and uniform dispersion of MWCNT within the PDMS viscous matrix. The suspension was added to PDMS followed by vigorous manual mixing. The mixture was then again sonicated in an ultrasonic bath for more than 10 min before being mechanically stirred for 1 h at elevated temperatures to evaporate the toluene solvent. Allowing the

mixture to cool to room temperature, PDMS curing agent was added at a weight ratio of 1:1 to PDMS pre-polymer. The mixture was stirred for 10 min before drop casting and levelling on petri dishes with dimensions of 100 mm diameter and 15 mm depth. These petri dishes were placed in vacuum oven for 1 h at 70 °C to degas and allowed to cure at room temperature for a period of 2 days. The resultant membranes had similar thicknesses of approximately 120 µm.

2.1.2 Graphene-PDMS nanocomposite membranes

Nanocomposite membranes were fabricated using PDMS and a proprietary cross-linker (Sylgard 184, Dow Corning Corporation) to provide the base polymer. Non-functionalized graphene flakes (70160-100ML, Cheap Tubes Inc.), was added as the filler to make the nanocomposites. A reference PDMS membrane was made as well as multiple weight ratios of graphene-PDMS nanocomposites which included: 0.125 wt%; 0.25 wt%; 0.5 wt%; and a 1 wt%. The exfoliation of the graphene flakes occurred in 20 mL of p-xylene using an ultrasonic bath for 1 h. This allowed time for the π-π interaction of the aromatic ring in the solvent and in the carbon matrix to facilitate maximum dispersion of the flakes in solution. The mixture was then added to 20 g of the PDMS oligomer and stirred before being returned to the ultrasonic bath for 30 min.

This mixture was then mechanically stirred at 100 rpm on a hotplate at 120 °C for approximately 1 h to allow for the evaporation of the majority of the solvent. After cooling to room temperature the proprietary crosslinking agent was added and thoroughly mixed in. All membranes were prepared utilizing a 10% weight ratio of base PDMS to the crosslinker. The solution was degassed for 30 min before being spun onto a silicon wafer and crosslinked at 75 °C. The membranes were then carefully peeled from the wafer. The membrane thickness lies within 120 ± 4 µm range. This thickness was found to be unaffected by the quantity of graphene added.

2.1.3 MoS_2-PDMS nanocomposite membranes

One gram of MoS_2 powders (99% purity, Sigma Aldrich) was added to 0.5 mL of solvent: N-methylpyrrolidinone (NMP, 99% anhydrous, Sigma Aldrich) or 0.25 mL H_2O and 0.25 mL ethanol solution, in a mortar and ground for 30 min. The mixture was then dispersed into 10 mL of the appropriate solvent (NMP or H_2O/ethanol solution). The slurry was then probe-sonicated (Ultrasonic Processor GEX500) for 120 min at 125 W sonication power and finally centrifuged for 45 min at 4000 rpm. The supernatant containing 2D MoS_2 nanoflakes was collected.

Nanocomposite membranes were fabricated using PDMS and a proprietary cross-linker (Sylgard 184, Dow Corning Corporation) to provide the base polymer. A reference PDMS membrane was made as well as two weight ratios of the two solvent exfoliated MoS_2 flakes. The supernatant containing the MoS_2 was dried in a vacuum oven for 72 h to remove the solvent. Para-xylene, was then added to the dried flakes and the mixture was then probe-sonicated for another 90 minutes. The suspension was then added to 20 g and 40 g of the PDMS oligomer to create the two separate concentrations. This mixture was then mechanically stirred at 100 rpm on a hotplate at 120 °C for approximately 1 h to allow for the evaporation of the majority of the solvent. After cooling to room temperature the proprietary crosslinking agent was added and thoroughly mixed in. All membranes were prepared utilizing a 10 wt.% ratio of base PDMS to the crosslinker. The solution was degassed for 30 minutes before being spun onto a porous PAN support and cured at 75°C. This method was chosen as it has been shown to maximize the gas permeability in pristine PDMS.[24] The membranes were then used for permeation measurements as well as structural and spectroscopic characterization. The membrane thickness, as determined using SEM imaging, lies within the 20 ± 3 µm range.

2.1.4 Ag-PDMS nanocomposite membranes

The polymeric nanocomposite membranes were fabricated utilizing PDMS (Sylgard 184, Dow corning corporation) and Ag nanopowder (Sigma-Aldrich Pty Ltd., 99.5% trace metal basis containing polyvinylpyrrolidone (PVP) as dispersant) with a particle size of less than 100 nm. An unfilled PDMS membrane and four different Ag-PDMS nanocomposite membranes with Ag nanoparticle weight percentages of 0.125%, 0.25%, 0.5% and 1%, were synthesized. Membranes with concentrations above 1% Ag could not be synthesized due to the heavy agglomeration of Ag particles in the process. The solvent p-xylene was added to the viscous PDMS elastomer to facilitate the distribution and achieving homogenous dispersion of Ag nanoparticles within the polymer matrix. The mixture was mechanically stirred for 20 min before sonication using a Cole-Parmer 500-W ultrasonic homogenizers for 1 h. After that the Ag-PDMS nanocomposite was precipitated in a methanol bath, while magnetically stirred to prevent the agglomeration of the nanoparticles. Next, the PDMS crosslinking agent was mixed into the nanocomposite with a ratio of 10:1 (base:crosslinking agent) and allowed to degas in a vacuum for 30 min. Finally, the composite mixture was spin-coated onto optically polished silicon wafers and placed in a 75 °C oven to crosslink for 40 min. The produced membranes had the thickness of 135±15 µm.

2.2. Characterization of nanocomposite membranes

2.2.1 Morphological characterization

Before being dispersed in PDMS, the dimensions of nanofillers were investigated using transmission electron microscopy (TEM), atomic force microscopy (AFM) and dynamic light scattering (DLS) system. In particular, A JEOL 2100 TEM was used with a lacey formvar/carbon grid for determining the quality of the graphene and dimensions of Ag nanoparticles. A Bruker D3100 AFM was used to determine the distribution graphene thickness operated in tapping mode. 200 flakes were assessed to obtain the distribution of graphene thickness. An ALV fast DLS particle sizing spectrometer was employedto understand the graphene lateral dimension and size distribution.

Membrane morphological characterizations were conducted using Scanning electron microscopy (SEM). FEI Nova NanoSEM imaging was utilized to evaluate the cross-sectional thickness of the membranes as well as the distribution of nanofillers into the PDMS matrix. AFM was also used to determine the nanofiller distribution after dispersion into the PDMS matrix using a Bruker D3100 in tapping mode on the surface of the material. 200 samples were assessed on the surface to obtain the distribution.

2.2.2 Structural characterization

A Thermo Nicolet 6700 spectrophotometer was used for recording the fourier transfer infrared spectroscopy (FTIR) of the PDMS and nanocomposites. Micro-Raman characterization of the samples was performed using a Renishaw Raman spectrometer at a wavelength of 514 nm. X-ray diffraction (XRD) data were collected on a D8 Advance Bruker AXS X-ray diffractometer with GADDS (General Area Detector Diffraction System). X-ray photoelectron spectroscopy (XPS) was performed using a Thermo Scientific K-alpha instrument with an Al Kα source. Water contact angle measurements were performed using a KSV 101 system. The height of each drop was confirmed using a CCD camera prior to each measurement to ensure consistency in the drop volume. Drop volumes of approximately 8 µL were employed.

Solvent swelling measurements were carried out using pre weighed dry membranes of various weight concentrations of nanofillers and the PDMS membranes. The membranes were totally immersed in pure toluene until equilibrium swelling was reached. The membranes were then pat dried and immediately weighed. This was carried out four times for each membrane to ensure repeatability.

Tensile testing was carried out using an Instron 4467 Universal testing machine fitted with a 100N load cell. Bluehill software was used to control the tensile test and to calculate the various tensile properties

reported. The testing speed was set to 10mm per minute. The tests were performed using ASTM D638 as a guide. Tensile test specimens used were not in accordance with the requirements of the standard, but were a close approximation to a type IV specimen. As it was not possible to attach an extensometer to the specimens and as a result the modulus figure reported were calculated using the movement of the crosshead as the extension measurement. This results in a lower a than actual tensile modulus figure.

Density measurements were performed using a density determination kit employing the hydrostatic weighing method. For the determination of density of the membranes, ethanol was used as the auxiliary liquid. The theoretical densities of the composite membranes are determined based on simple consideration of the relevant densities:

$$\frac{m_{composite}}{\rho_{theory}} = \frac{m_{nanofiller}}{\rho_{nanofiller}} + \frac{m_{PDMS}}{\rho_{PDMS}} \quad (1)$$

where *m* is the mass of the relevant species, $\rho_{nanofiller}$ is taken as that of graphite (2.267 g/cm^3) or Ag (10.49 g/cm^3) and ρ_{PDMS} is 1.033 g/cm^3. The additional fractional free volume (FFV) and thus the total FFV could then be determined by a comparison between the theoretical and the experimentally determined densities:

$$TotalFFV = FFV_{PDMS} + \frac{\frac{1}{\rho_{exp}} - \frac{1}{\rho_{theory}}}{\frac{1}{\rho_{theory}}} \quad (2)$$

Positron annihilation lifetime spectroscopy (PALS) was performed using a positron source of 30 µCi NaCl sealed in a Mylar film at room temperature. Free standing samples were stacked to 4 mm thick bundles with the positron source placed in the middle. A minimum of 5 measurements each with 1×10^6 integrated counts per measurement were made using an automated EG&G Ortec fast-fast coincidence system with a timing resolution of 260 ps. The data was analysed using LT (version 9.0) using a source correction of 1.740 ns and 3.014%. The data was fitted to 3 components including a *para*-positronium component, fixed at 125 ps, a free positron annihilation component, ~400 ps and the *ortho*-positronium (*o*-Ps) component. The *o*-Ps component's intensity and the lifetime were employed to determine the relative number of free volume elements and the average size of the free volume elements within the sample respectively. The Tao-Eldrup Equation was used for calculating the average size of the free volume elements.

The surface properties of the nanocomposite membranes were also investigated by measuring their hydrophobicities. Water contact angle measurements were performed using a KSV 101 system. The height of each drop was confirmed using a CCD camera prior to each measurement to ensure consistency in the drop volume. Drop volumes of approximately 8 µL were employed.

For Ag-PDMS nanocomposite membranes, there were two extra characterization methods to be utilized for evaluating their antimicrobial properties:

*Catalysis:*The catalytic ability of the Ag nanoparticles embedded within the PDMS films were performed by studying the model reaction involving metal-induced reduction of ferricyanide by thiosulfate ions. The catalysis experiments were performed by immersing equally sized Ag-PDMS films in an aqueous solution (10 mL) containing 0.1 M thiosulphate and 1 mM potassium ferricyanide. The reaction was held at 20 ± 2 °C with continuous stirring at 200 rpm. The conversion of ferricyanide to ferrocyanide was analysed by UV-vis absorbance spectroscopy (Cary 50 Bio spectrophotometer) in a cell of 1 cm path length by taking aliquots from the reaction.

Ag^+ Ion Leaching: Leaching of Ag^+ ions from Ag-PDMS was determined by immersing the films in deionized water (pH 6.2) for 1 month at room temperature, and analysing the supernatant using an inductively coupled plasma optical emission spectrometer (ICP-OES, PerkinElmer Optima 4300 DV).

2.2.3 Gas permeation studies of nanocomposite membranes

A series of experiments were conducted to assess the gas permeability of the membranes. A constant pressure variable volume (CPVV) system (Fig. 1a) was used to measure the permeability of CH_4, N_2,Ar and CO_2 (99.99%, Core Gas Australia) through the PDMS and nanofillers-PDMS nanocomposite membranes. The membranes for testing were mounted within a permeation cell with a constant pressure on the upstream boundary, while the downstream side was kept at the atmospheric pressure. The pressures tested to ensure repeatability were of 200, 300 and 400 kPa. Both sides of the permeation cell were purged with the penetrant gas prior to each experiment. To maintain a constant temperature the permeation cell was housed in an environmental chamber with all measurements conducted at 37 °C. The membranes' permeability was measured in the following order: CH_4, N_2, Ar, CO_2. The flow rate was acquired every ten seconds for two minutes once a steady-state was achieved and the values were averaged and converted into permeability values given in Barrer (1 Barrer = 1×10^{-10}.cm^3.(STP).cm/cm^2.s.cmHg).

As the CPVV apparatus is only suitable for pure gas permeability measurements, a modified setup (Fig. 1b) was employed to evaluate the removal efficiency of the H_2S mixed gas through the Ag-PDMS nanocomposite membranes. The chamber held the membranes to be evaluated against a commercial H_2S electrochemical sensor (EC4-100-H_2S, e2v technologies). The H_2S mixed gas flow was controlled using a mass flow controller (MKS Instruments, Inc, USA) with a constant pressure maintained in the chamber *via* a back pressure regulator to 120.68 kPa and an atmospheric pressure (100 kPa) at the permeate side of the membrane. All measurements were housed and conducted in an environmental chamber with a temperature of 37 °C. For the initial experiment, nanocomposite membranes were exposed to H_2S gas for 3 h. The corresponding sensor response curves, including the sensor lag time, were analysed to reveal the H_2S gas permeation kinetic through the membranes. After the first run, the exposed membranes were then purged with N_2 gas for 24 h to ensure the complete desorption of H_2S gas molecules. Subsequently, the membraneswere re-exposed to H_2S gas for 70 h to confirm the establishment of equilibrium between the nanocomposite membranes and H_2S gas molecules.

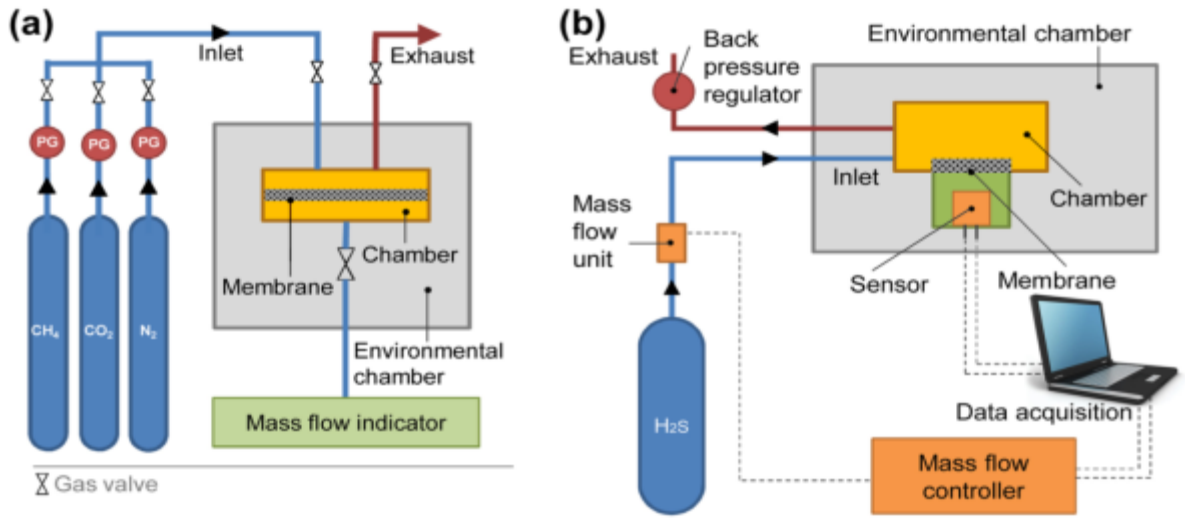

Figure 1. (a) Schematic of the constant pressure variable volume (CPVV) single gas permeation apparatus (not to scale). (b) Schematic of the H_2S mixed gas sensing (not to scale).

Similar experimental setup was also applied to the gas permeation measurements of MWCNT-PDMS and MoS_2-PDMS nanocomposite membranes towards mixed gas in zero air balance (with humidity < 5%R.H.). For MWCNT-PDMS nanocomposites, the CH_4 and H_2 gas sensors utilized in the system were commercially available from Figaro Japan Inc (TGS2611). For MoS2-PDMS nanocomposites, a commercial electrochemical NO_2 (EC4-250-NO, e2v technologies) sensor was used.

2.3. *In vitro*microbialstudies on the surface of nanocomposite membranes

Culturing Procedure: Luria-Bertani (LB) broth powder (US Biological) (100 mL) was prepared as instructed and sterilized by autoclaving at 121°C for 40 min. An aliquot (10 mL) of the LB broth was decanted and used to culture a stock solution of *E. coli* (ATCC strain, Sigma Aldrich), where the culture was incubated for 12h at 37 °C with rotation and stored at 4 °C. The pristine PDMS and the nanocomposites with varying Ag concentrations of 0.125, 0.25, 0.5 and 1 *wt*% were repeated 4 times, first sterilised using UV light, for 30 mins on each side in a glass Petri dish. Each membrane was then transferred into a vial containing 5 mL of LB broth to give 20 vials with membranes and 4 vials without, as a control. Each vial was then seeded with 0.5 µL of the stock *E. coli* solution and incubated with rotation at 37 °C for 5 h.

Measurement Procedure: UV-vis (600 nm) was performed on 4 mL aliquots of the broth after incubation on a Varian Cary 50 Bio UV-Vis Spectrophotometer. Quantitative fluorescence microscopy was performed on the pristine PDMS (control), 0.25 and 1 *wt*% nanocomposites. Two fluorescent dyes were used in combination: SYTO9 (Invitrogen AG, Basel, Switzerland), and PI (Invitrogen). Stock solutions from the LIVE/DEAD BacLight kit (Invitrogen) were prepared as instructed by the manufacturer. Samples were incubated in the dark at room temperature for 25 min before analysis. Cell counts and area coverage were calculated using ImageJ software.

2.4. *In vivo*microbialstudieson the surface of nanocomposite membranes

All experiments involving ruminants were undertaken within the procedure outlined and approved by the CSIRO FD McMaster Laboratory Chiswick Animal Ethics Committee. The control PDMS and the Ag-PDMS nanocomposites that were synthesized were cut into 2 × 2 cm squares. Twenty squares of each type of material, PDMS control, 0.125 wt% 0.25 wt% Ag-PDMS, 0.5 wt% Ag-PDMS and 1 wt% Ag-PDMS nanocomposites, were made and labeled.

One of each Ag concentration square was placed into a nylon mesh bag, measuring 10 × 24 cm, and each sewn into place using a 6 pound KATO fishing braid and superfine needle to keep them separated during the experiment and prevent occlusion of the surface area to the rumen fluid. Once all 20 bags were finished (80 membranes in total), 4 bags were selected at random and tied together.Each group of bags was bound together with 0.8mm fishing line, with a 200g brass weight attached to approximately 20 cm length of line. There were 5 groups of 4 bags created in total, each weighted, tied together and placed into the rumen of a fistulated 3 year old Jersey steer. Each group of bags was retrieved from the steer at successive time intervals. The first was removed 4, 7, 14, 21 and 28 days. The steer grazed on native pasture throughout the experiment, plus ~500 g of lucerne pellets during retrieval of each bag.

Once a randomly selected group of 4 bags was removed from the steer the PDMS and nanocomposite material was rinsed before each being cut into two. Half of each square was placed into jars, one containing glutaraldehyde for electron microscopy studies and the other into a phosphate buffered saline (PBS) solution for DGGE and PCR analysis. The glutaraldehyde jars were stored at room temperature while the PBS Jars were stored in a freezer at -20 °C.

Electron Microscopy: Once removed from the glutaraldehyde, each square went through a series of ethanol rinses slowly increasing the concentration of ethanol up to 100%. The samples were then dried in a critical point dryer before being coated with a thin layer of gold (2.5 nm). An FEI Nova NanoSEM was employed to evaluate the morphologies and relative surface growth on the control PDMS and nanocomposite materials.

DNA Extraction and Purification: DNA was extracted from duplicate control (pristine PDMS, 0 wt% Ag nanoparticle content) and test membranes (0.125 wt%, 0.25 wt%, 0.5 wt% and 1wt% Ag nanoparticle content) retrieved from the rumen of fistulated animals over 28 days using a phenol-chloroform-isoamyl alcohol bead beating method. Each membrane was added to a 2 mL Eppendorf tube which contained 0.5 mL of Tris equilibrated phenol-chloroform-isoamyl alcohol (24:24:1), 0.5 mL of sterile phosphate buffer (100 mM, pH 8) and 0.5 g of sterile glass beads (150-212 µm; Sigma-Aldrich, Castle Hill, NSW, Australia).

The mixture was then subjected to bead beating using a mini-bead beater K9, (Biospec, USA) for 30 s twice, stored on ice in-between the bead beating sessions before being centrifuged at 10,000 × g for 10 min. The aqueous layer was then aseptically removed into a fresh sterile Eppendorf tube and an equal volume of phenol-chloroform-isoamyl alcohol added to it, followed by a quick vortex and centrifuging at 10,000 × g for 10 min. This process was repeated twice to obtain the crude DNA of microorganisms. The crude DNA was purified using GENECLEAN^{R} Turbo kit (MP Biomedicals, USA). Three hundred microliters of crude DNA was added to a sterile Eppendorf tube to which 5 × volume of Gnomic Turbo solution was added. The mixture was vortexed for 5 s after which 600 µL of this mixture was added to GENECLEAN filter and centrifuged at 10,000 × g for 5 s and the flow through discarded. The remaining manufacturer protocol was then followed.

PCR and Denaturing Gradient Gel Electrophoresis (DGGE): Universal eubacterial primers 341FGC and 518R were used for PCR assay of purified DNA obtained from control and Ag nanoparticle impregnated membranes. The thermocycling program used was: 1 cycle at 95 ^{o}C for 5 min, 30 cycles of 95 ^{o}C for 30 s, 55 ^{o}C for 30 s and 72 ^{o}C for 60 s and a final extension at 72 ^{o}C for 10 min. PCR amplicons were analysed on a Universal Mutation Detection System D-Code apparatus (BioRad, CA, USA) with a 9% acrylamide gel. The denaturing gradient used was 40-60% and the DGGE gel was run for 20 h at 60 V and at 60 ^{o}C. The DGGE gels were Ag stained, scanned and saved as TIFF files. For ease of analysis, cumulative DGGE gels were prepared and loaded with an equal mixture of duplicate samples per DGGE lane.

Statistical Analysis: All measurements were repeated **four** times (n=4) with all errors shown in this study are given in standard deviations. The digitized images were analysed with TL 120 D advance analysis package (Totallab, U.K.) for similarity relationships and diversity values. The relatedness of the microbial community on the control and Ag nanoparticle impregnated membranes was expressed as similarity clusters using the unweighted paired group method with mathematical averages (UPGMA). The microbial community diversity of the membrane samples was evaluated with Shannon Weaver diversity (*H'*) index using the equation:

$$H' = -\sum p_i \times \ln p_i \qquad (3)$$

where p_i is the proportion of the community that is made of species *i* (intensity of the band *i*/total intensity of all bands in the lane) and ln p_i is the natural log of p_i. Principal component analyses were carried out on the matrix data obtained from DGGE profiles using SPSS version 21 software.

2.5. Associate the micro-organisms to the gas constituents of the environment

Rumen liquor samples are the starting materials and collected from a fistulated cow in a farm (DPI Victoria – provided by Dr. Peter Moat). As soon as collected, the rumen liquor samples are stored in vacuum flasks surrounded by dry ice for transportation. When arrived at the analysis facility at RMIT University, the samples are stored at –80 ºC to maintain the integrity of microbial colonizers. Upon gas measurement experiments, the defrosted samples are mixed with the oxygen-free Menke buffer at the volume ratio of 1:2 to provide the necessary nutrition for the microbial colonizers. Our Menke buffer consists of 13.2 g $CaCl_2 \cdot 2H_2O$, 10.0 g $MnCl_2 \cdot 4H_2O$, 1.0 g $CoCl_2 \cdot 6H_2O$, 8.0 g $FeCl_3 \cdot 6H_2O$ and made up to 100 ml of H_2O. The liquid mixture is then quickly placed into a sealed headspace vial at the sample-to-volume ratio of 1:25 at an incubation temperature of 40 ºC to simulate the rumen environment. The ratio is optimised to avoid the situations of either too much gas production to saturate the gas sensor response or small gas production that is below the detection limit of the gas sensors. In order to simulate the rumen environment for the microbial culture, oxygen-free environment was needed and produced by flushing the vial with nitrogen gas. Eventually, a non-dispersive infrared (NDIR) sensor that is capable to measure the CH_4 and CO_2 gas concentration ranging from 0-100 vol% was placed into the headspace of the vial to perform the real-time measurements. A 0.25%wt Ag/PDMS membrane was placed in front of the sensor. It should be noted that the pressure inside the vial is kept constantly at 1 psi to exclude the pressure effect interference with the sensor.

DNA was extracted from rumen samples using MoBio UltraClean Fecal DNA isolation kit according to the manufacturer's description. Briefly, 300 µl of a selected rumen sample was added to a dry bead tube followed by the addition of 550 µl of Bead solution to the mixture in the 2 mL dry bead tube. Solutions S1 (60 µl) was added to this tube and the tube was briefly vortexed to mix the content. Solution IRS (Inhibitor Removal Solution) (200 µl) was added to the mixture which was then subject to two rounds of bead beading (30 s × 2). The rest of the protocol, as described by the manufacturer, was then followed.

Universal Eubacterial primers 341FGC and 518R were used for PCR assays of purified DNA obtained from rumen samples. The thermocycling program used was: 1 cycle at 95 ^{o}C for 5 min, 30 cycles of 95 ^{o}C for 30 s, 55 ^{o}C for 30 s and 72 ^{o}C for 60 s and a final extension at 72 ^{o}C for 10 min. PCR assays for methanogens were carried out *via* a nested PCR reaction. The initial PCR was carried out with Met 86F and Met1340R primers after which a second round of PCR (nested) was carried out with primer pair 0357FGC and 0691R.

Quantitative PCR assays were carried out on Rotor-Gene Q qPCR equipment. The total population of methanogens was quantified in rumen samples by using primer pair UniMet1-F and UniMet1-R. qPCR was performed using SYBR green chemistry with KAPA SYBR FAST one-step qRT-PCR kit with appropriate standards and selected rumen samples. Each qPCR reaction contained; KAPA SYBR® FAST qPCR Kit Master Mix (10 µL), RNase-free sterile water (8.2 µL), Forward primer (0.4 µL, 10 pmol/µL), Reverse primer (0.4 µL, 10 pmol/µL) and DNA template (1 µL). The following program was used; 1 cycle at 95 ^{o}C for 10 min, 40 cycles of 95 ^{o}C for 30 s, 60 ^{o}C for 30 s and 72 ^{o}C for 60 s with signal acquisition at 80 ^{o}C for 10 s and a final extension at 72 ^{o}C for 5 min. For melting curve detection, the temperature was increased every 5 s by 0.3 ^{o}C from 50 ^{o}C to 95 ^{o}C. Standard curves were constructed from a serial dilution of DNA from a methanogenic bacteria and population of methanogens expressed as gene copy numbers ml^{-1}.

Replicate PCR amplicons were analysed on a Universal Mutation Detection System D-Code apparatus (BioRad, CA, USA) with a 9% acrylamide gel. The denaturing gradient used was 45-60% and the DGGE gel was run for 20 h at 60 V and at 60 ^{o}C. The DGGE gels were silver stained, scanned and saved as TIFF files.

The digitized images were analysed with TL 120 D advance analysis package (Totallab, U.K.) for similarity relationships. The relatedness of the microbial communities (in total bacteria and methanogens community profiles) was expressed as similarity clusters using the unweighted paired group method with mathematical averages (UPGMA).

3. Results

3.1 Characteristics of nanocomposite membranes

3.1.1 MWCNT-PDMS nanocomposite membranes

The nanocomposite MWCNT/PDMS membranes were characterized using SEM, vibrational spectroscopy techniques and XPS to determine their properties at different CNT concentrations.In order to examine the dispersion of MWCNT throughout the polymer and the morphology of the composites, SEM was used. To prevent charging of the nanocomposites under the microscope, the 1% sample was coated with platinum and all of the other samples images were captured at relatively low beam voltages.

Fig. 2 shows the SEM images of the fabricated MWCNT/PDMS composites. It was observed that particle dispersion was reasonably homogenous for all samples. However, some MWCNT dense areas bundles were still present in the membranes. Visually as the concentration of MWCNT increases in the membrane, its structure transformed further to a composite structure. No exceptional morphological behaviour was observed after the addition of MWCNT particles at different concentrations.

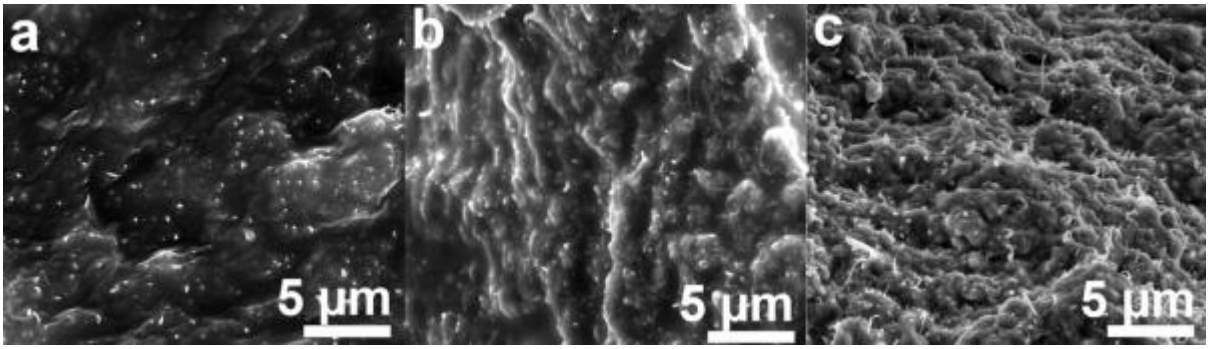

Figure 2. Cross sectional SEM images of MWCNT/PDMS nanocomposite membranes of different concentrations, showing the bundle distributions for MWCNT weight concentrations of: (a) 1%; (b) 5%; and (c) 10%.

Fig. 3 illustrates the FTIR spectra of pristine PDMS and MWCNT/PDMS composites of different concentrations. The peaks between 1400–1420 cm^{-1} and between 1240–1280 cm^{-1} correspond to $–CH_3$ deformation vibration in PDMS. The Si–O–Si stretching multi-component peaks for PDMS are observed in the range between 930 to 1200 cm^{-1}. The significant difference between pure PDMS and MWCNT/PDMS composite FTIR spectra is observed at 905 cm^{-1} for which the peak becomes sharper and gains a notably lower intensity as the concentration of MWCNT increase in PDMS. This could be due to the formation of Si–C bond. It has been previously reported that Si–C bands and $Si(CH_3)_2$ rocking peaks appear in the region of 825–865 cm^{-1} and 785–815 cm^{-1}, respectively, which are also seen in our FTIR spectra for composites. The peaks that appear between 2100–2200 cm^{-1} is due to the formation of SiH bond in the matrix. The symmetric and asymmetric peaks that appear at 2906 cm^{-1} and 2950–2970 cm^{-1} are due to the $–CH_3$ stretching in $≡Si–CH_3$.

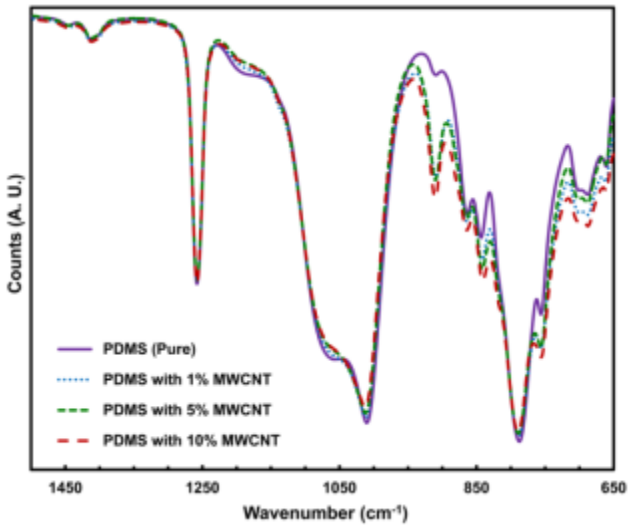

Figure 3. FTIR spectra for the pure PDMS and MWCNT-PDMS nanocomposite membranes.

The pure PDMS membrane Raman spectrum presented in Fig. 4 (continuous line), contains the typical PDMS peaks, concurring with the spectra presented in previous works [30]. It comprises of a Si–O–Si symmetric peak at 488 cm^{-1} and at 607 cm^{-1} appears the $Si–CH_3$ symmetric rocking peak. The Si–C symmetric stretching appears at 708 cm^{-1} and CH_3 asymmetric rocking appears at 787 cm^{-1}. At 862 and 1262 cm^{-1}, CH_3 symmetric rocking and symmetric bending are seen, respectively. Following the

dispersion of MWCNT' within the MMM, we observe that the Si–CH_3 symmetric rocking band shift peak decreases as the concentration of MWCNT increases.

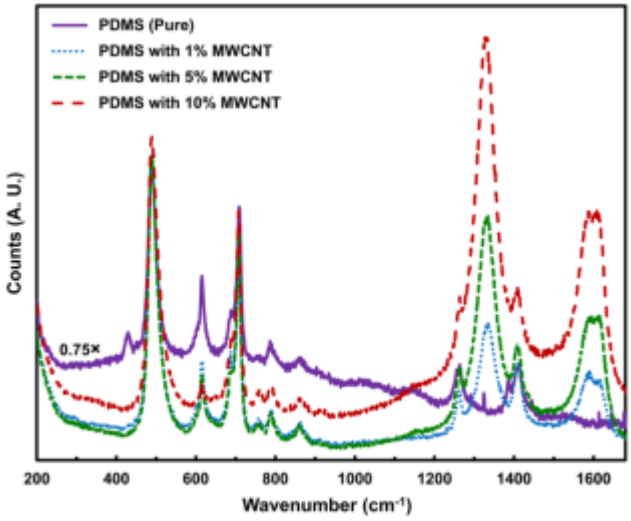

Figure 4. Micro-Raman spectra for pure PDMS and three different MWCNT concentrations in MWCNT-PDMS nanocomposite membranes.

MWCNT's Raman spectra have been thoroughly studied, and have band assignments that are well established. The Raman spectra of the MWCNT-PDMS nanocomposites show the first order carbon bands as the *D* band (disorder band) at around 1330 cm^{-1} and a wide *G* band (TM-tangential mode or graphite band) at around 1605 cm^{-1}. The two bands can be clearly seen in Fig. 4 with the *D* band showing the disorder in the graphitic structure of MWCNT. The wide peak observed in the *G* band can be explained by the disentanglement of the MWCNT and subsequent dispersion in the PDMS matrix as an outcome of polymer infiltration into the MWCNT bundles. The intensity ratio of *D* and *G* bands has been shown to be a strong indicator of the structural arrangement. The intensity ratios of *D* band to the *G* band ($I_D//I_G$) in the composites ranged from 1% to 10% increased from 1.59 to 1.72, respectively, showing the reduction in the order as the amount of MWCNT increases.

Figs. 5a and d show the C(1s) XPS spectra of the PDMS membrane and the PDMS+1% MWCNT composite, respectively. Curve fitting reveals a singular peak centred around a binding energy of approximately 284 eV, which corresponds to C–C, C=C, and C–H bonds. It is important to note that the C–Si bond also lies within this peak at 283.8 eV. The C(1s) peak within the pure PDMS membrane resulted in 44% of the overall binding energy, while in the nanocomposite membrane was responsible for 48% of all binding energy. This was expected with the addition of the MWCNT within the polymer matrix. The O(1s) spectrum of the PDMS and the 1% MWCNT-PDMS composite presented in Fig. 5(b) and (e) show a singular peak fitted to approximately 532 eV that match up to those found in past studies.

It was also important to examine the Si(2p) XPS spectrum for the pure PDMS and the PDMS nanocomposite as shown in Fig. 5c and f, respectively, to assess the type of bonds that Si atoms establish. The deconvolution of the Si(2p) spectrum results in two peaks, one occurring at 102 eV (peak *A* in Fig. 5c and f) ,which can be attributed to Si-O bonds within PDMS and the other at and 103.7 eV (peak *B* in Fig. 5c and f), which corresponds to silicon bonding to three oxygen atoms, which compares to those found in earlier reports. The figures show a clear reduction in the occurrence of the higher binding energy peak within the nanocomposite, when compared to the pure PDMS spectrum. This suggests that the reduction in quantity of silicon to three oxygen bonds is in response to this increase in the number of Si–C bonds occurring with the addition of MWCNT.

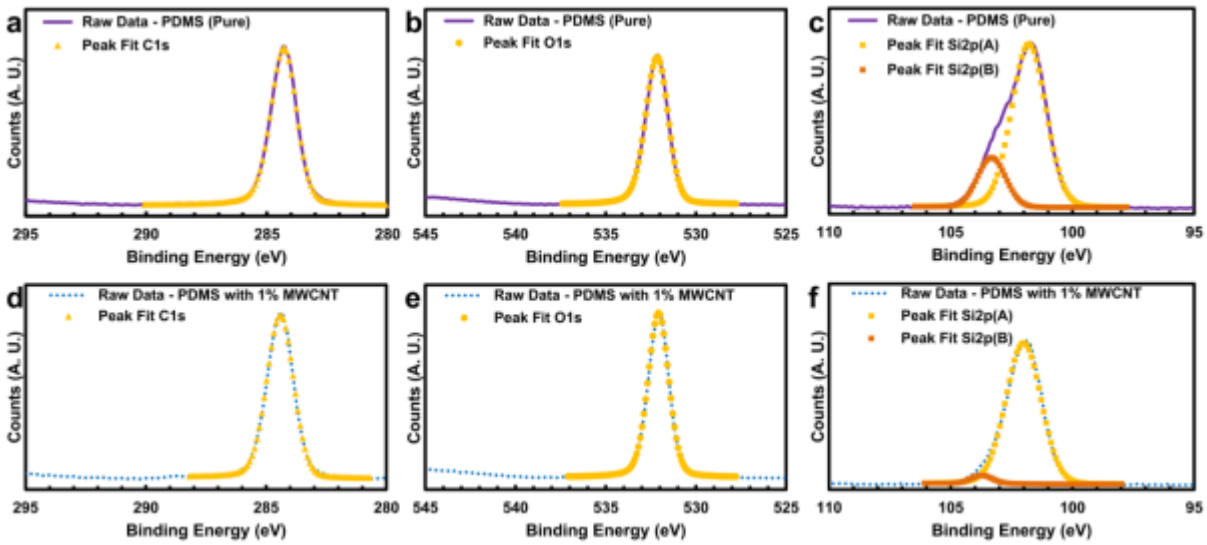

Fig. 5. XPS analysis results: (a)-(c) show C, O, and Si peaks for the pure PDMS, respectively. (d)-(f) show C, O, and Si peaks for the 1% MWCNT-PDMS, respectively.

The gas selectivity and permeability of the composite membranes were inspected at several concentrations of CH_4 and H_2 in ambient air, pumped through the mass flow controller setup that was presented in Section 4.2.3. The sensor's resistance was sampled every 10 s during the gas exposure. In order to evaluate the cross-talk and gas permeability for the composites, several gas streams of varying concentrations of H_2 and CH_4 mixtures in ambient air were pumped into the chamber *via* the mass flow controller. First, H_2 gas streams were pumped with concentrations of 0.5% and 1.0% in ambient air, and to facilitate sensor recovery ambient air was pumped following the two gas cycles. Afterwards, the chamber was filled with streams of 0.5% and 1.0% CH_4 (also in ambient air), similarly followed by ambient air after gas cycles for sensor recovery. Finally, to examine the behaviour of the sensor and the membrane in mixed gas environment, the mass flow controlled pumped a mixture of 0.5% H_2 and 0.5% CH_4 into the chamber.

Due to the different permeability of the gas species through the membranes exposure times were varied. For the relatively fast gas permeability of H_2,the exposure time was 10 min with a 25 min ambient air recovery in between exposures. CH_4 gas diffusion was relatively slower, and required a longer exposure time of 20 min and 40 min ambient air recovery between exposures.

As the chamber was filled with these gases, the concentrations of the analyte gases that permeated through the different membranes were measured by the commercial sensor. Utilizing the different MWCNT/PDMS membranes in conjunction with the commercial sensor, when exposed to the different concentrations of gas species, the relative normalized permeability ratios for the various composite membranes for different gas species were obtained and demonstrated in Fig. 6. In this graph, all measurements were acquired at room temperature as mentioned previously. The dynamic response of sensing system at different concentrations of gases, used to extract the data presented in Fig. 6, is presented as Fig. 7.

As can be seen in Fig. 6, for different wt% MWCNT/PDMS composites, the response magnitudes and their trends were fairly similar upon exposure to both 0.5% and 1.0% H_2. The permeation of H_2 through the membranes decreased as the concentration of MWCNT increased within the polymer matrix. The permeation of the 0.5% H_2 in ambient air dropped by around 21%, 60%, and 77% through the 1%, 5%, and 10% MWCNT-PDMS composites, respectively. In addition, the permeation of the 1.0% H_2 decreased by approximately 11%, 53%, and 57% through the 1%, 5%, and 10% MWCNT/PDMS composites, respectively.

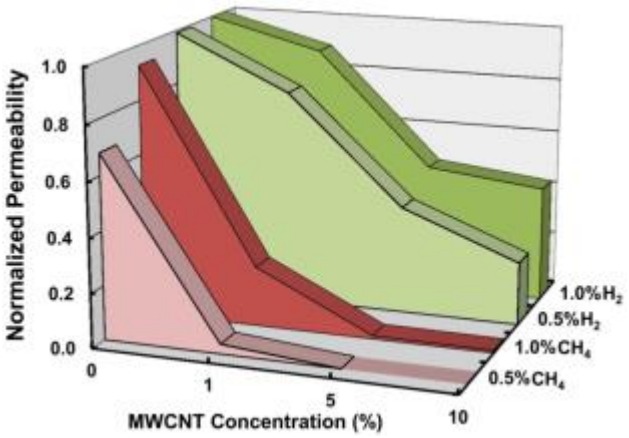

Figure 6. Normalized relative permeability of MWCNT-PDMS membranes to various concentrations of CH_4 and H_2 in ambient air.

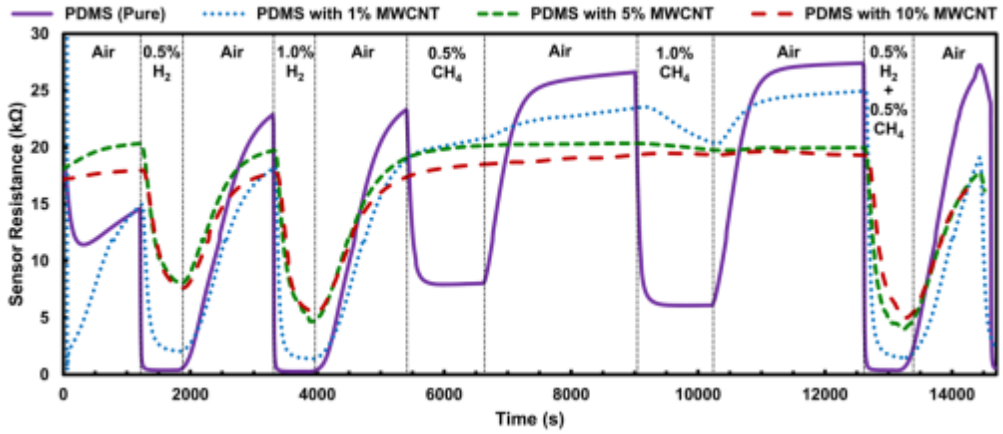

Figure 7. Dynamic response of the sensor-membrane system upon exposure to different gas concentrations and mixtures.

Conversely, embedding MWCNT in PDMS considerably attenuated the permeability of the membranes to CH_4. As the concentration of MWCNT increased beyond 1% within the composite material, the membrane almost completely blocked CH_4 diffusion, while allowing the passage of H_2. For the 0.5% CH_4 in ambient air the permeation was attenuated by 96% through 1% MWCNT-PDMS composite and was almost completely blocked at 5% and 10% MWCNT-PDMS composites. The permeation through the 1% MWCNT/PDMS composite of 1% CH_4 dropped by 77% and by around 99% through the 5% and 10% MWCNT/PDMS composites.

It is important to consider that CH_4 molecules are much larger and heavier than H_2 molecules, and as a result their permeations through the membranes take longer. Consequently, CH_4 molecules spend longer time in the membranes, and hence, have a higher chance to interact with the content of the membranes. Additionally, their larger size also increases their chance of interaction with the surroundings. This means that the change in the polymerization and increase in the filler concentration, affect them more significantly than H_2 molecules. It is fascinating to observe that even H_2 molecules permeation experience a decrease at higher concentrations of MWCNT. Moreover, it would be interesting to report the concentration of MWCNT at which a complete blockage of H_2 molecules permeation would occur. However, it is actually not possible to increase the MWCNT concentration in the MWCNT-PDMS membrane composite further than 10% due to the dominance of MWCNT over the PDMS part of the

membrane which cannot be made continuous anymore. As a result, the membrane will have sub-micron or micro-pores that allow the passage of all gases indiscriminately.

As revealed from our FTIR analysis (Fig. 3), the intensity of the peak observed at 905 cm^{-1} decreased as the concentration of MWCNT increased in the composite, which corresponds to the formation of Si–C bond. Moreover, with the increase of MWCNT in PDMS, the $Si(CH_3)_2$ rocking peaks appear to decrease due to the breaking of $Si\text{-}CH_3$ which lead to an increase in the intensity of SiH peaks. This suggests that these bonds play a significant role in blocking CH_4 through the composite membranes. Similarly, micro-Raman spectra (Fig. 4), demonstrates the decrease of the $Si–CH_3$ symmetric rocking band as the concentration of MWCNT increases which agrees with the results obtained from FTIR. Additionally, the XPS analysis shows a decrease in the number of silicon to three oxygen bonds occurring, allowing the increased formation of the Si–C bonds.

We have seen a similar behaviour in the Raman and FTIR spectra of the composites after increasing the concentration of carbon black (CB) fillers. However, there is a striking difference between the behaviour of MWCNT-PDMS and CB-PDMS membranes. CB-PDMS membranes showed blocking of CH_4 only at 6% of CB but the membranes with the higher concentration of CB could not block CH_4. This was associated to the decrease in the number of non-polymerized Si−O and $Si–CH_3$ bonds. Interestingly, the concentration of these bonds increased at higher concentrations of CB in the membranes.

We see the same trend for MWCNT-PDMS composites at low concentration of MWCNT, a decrease in the number of $Si–CH_3$ and Si–O bonds and increase in the number of Si−C bonds. However, for MWCNT composites, increasing the MWCNT concentration above 1% also enhance the blocking of CH_4 even further. This is in agreement with characterization outcomes which confirm that the prevalence of Si−C bonds remain high, even at high concentrations of MWCNT. The most significant difference between CB and MWCNT is the large surface area of MWCNT. While at high concentrations of CB the polymerization of the PDMS onto the surface of carbon was reduced, the same trend was not seen for MWCNTs composites due to the fact that MWCNT have much smaller dimensions, much higher surface activity, and better dispersion in the polymer matrix. These observations confirm our initial hypothesis predicting better performance of MWCNT as a filler for gas separation membranes.

3.1.2. Graphene-PDMS nanocomposite membranes

To understand the properties of the graphene flakes, as well as their morphology (Fig. 8), DLS, AFM and TEM were performed on the flakes after the exfoliation process but before being added into the nanocomposite. AFM revealed the thickness distribution of the graphene flakes, with the majority of flakes containing less than 10 layers (less than 4 nm). To understand the distribution of the flake dimensions, DLS was performed. This revealed that the lateral dimensions of the majority of flakes lie within 0.1 to 4 µm. This results in an average aspect ratio of 110 for the graphene flakes used in the composite membranes. TEM was used for assessing the morphology of the graphene flakes after the exfoliation process.

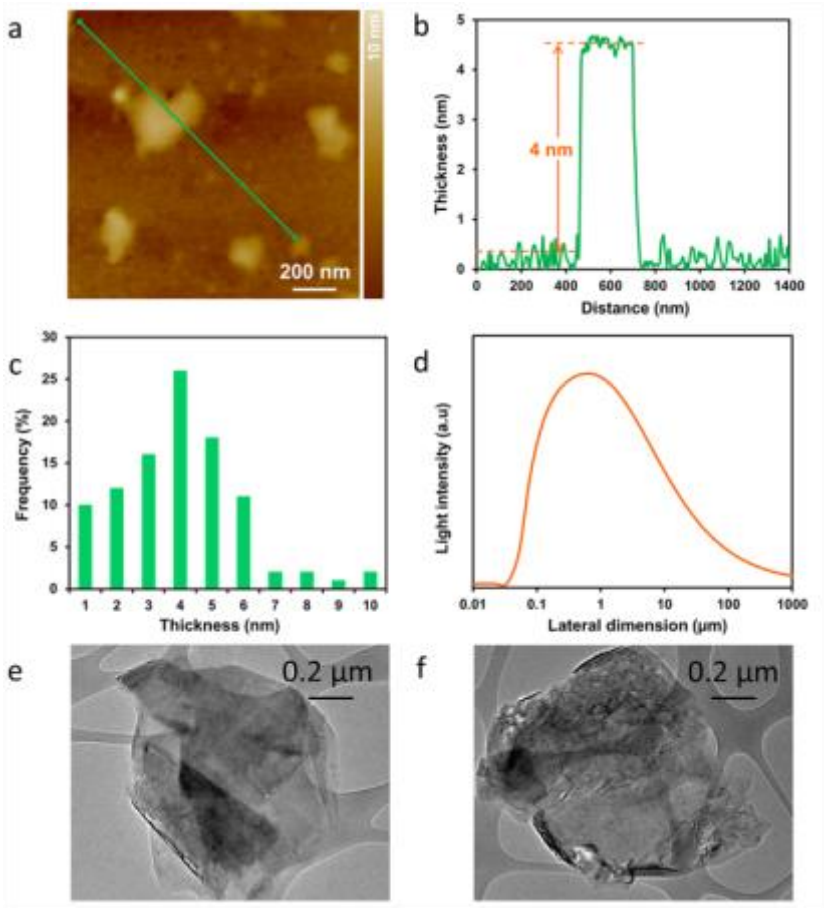

Figure 8. (a) AFM image of graphene flakes. (b) Corresponding height profile of graphene flake along the green line. (c) Distribution of graphene flake thickness taken from the analysis of 100 flakes with the AFM. (d) Distribution of graphene flake lateral dimensions obtained from the DLS. (e) and (f) TEM image of typical graphene sheets.

To understand and evaluate the alterations that graphene is providing to the nanocomposite different characterization techniques were employed with an emphasis on studying the physiochemical properties that relate directly to gas permeation. Graphene-PDMS composite membranes with the graphene concentration of 0.125 wt%, 0.25 wt%, 0.5 wt% and 1 wt% graphene were synthesized. Due to the formation of interconnected interfacial voids above

1 wt% graphene loading (which will be described later) thus creating defects within the membrane. This allows gas species to pass freely and hence providing no selectivity, rendering the membranes ineffective. A very important factor in dictating gas molecule permeation through rubbery polymers like PDMS is the FFV. This can fundamentally change the diffusion of the gas molecules through the membranes. To understand the impact that the addition of graphene has on FFV, both density measurements and PALS were carried out. The polymer density is commonly associated with FFV and it is known that PALS can be used to determine the average size of the free volume elements, and the concentration, or relative number of free volume elements in the sample.

The density of the various weight concentrations of graphene composite membranes are shown in Fig. 9a. It can be seen that adding graphene reduces the density of all of the composite membranes, relative to that of the predicted theoretical calculations. The lowest density for all of the different membranes is found at 0.25 *wt*% graphene in PDMS. This data can be used for assessing the additional free volume that possibly results from the weak interaction between the graphene flakes and the polymer (Fig. 9b). Such increases in FFV are well known and are often referred to as the ‘sieve in a cage’ phenomenon.

The PALS data for different membranes are presented in Figs. 9c and d. As can be seen from Fig. 9c, the o-Ps lifetime (τ_3) parameter does not show any significant difference in the size of the free volume elements, revealing the average pore diameter to be approximately 0.8 nm, with all variance between the different nanocomposites lying within the range of uncertainty. With the addition of graphene into the polymeric matrix, the intensity parameter (I_3) (Fig. 9d) nevertheless does demonstrate an initial decrease in the number of free volume elements (0.125 and 0.25 *wt*%). This number then increases with increasing graphene concentration (0.5 and 1 *wt*%). While the calculations from the density measurements show an increase in FFV in the nanocomposites, the PALS intensity parameter reveals only a minor decrease in free volume elements within the range of detection. As a result, there must be a formation of voids that lie outside the detection limit of PALS (approximately ≤20 nm).

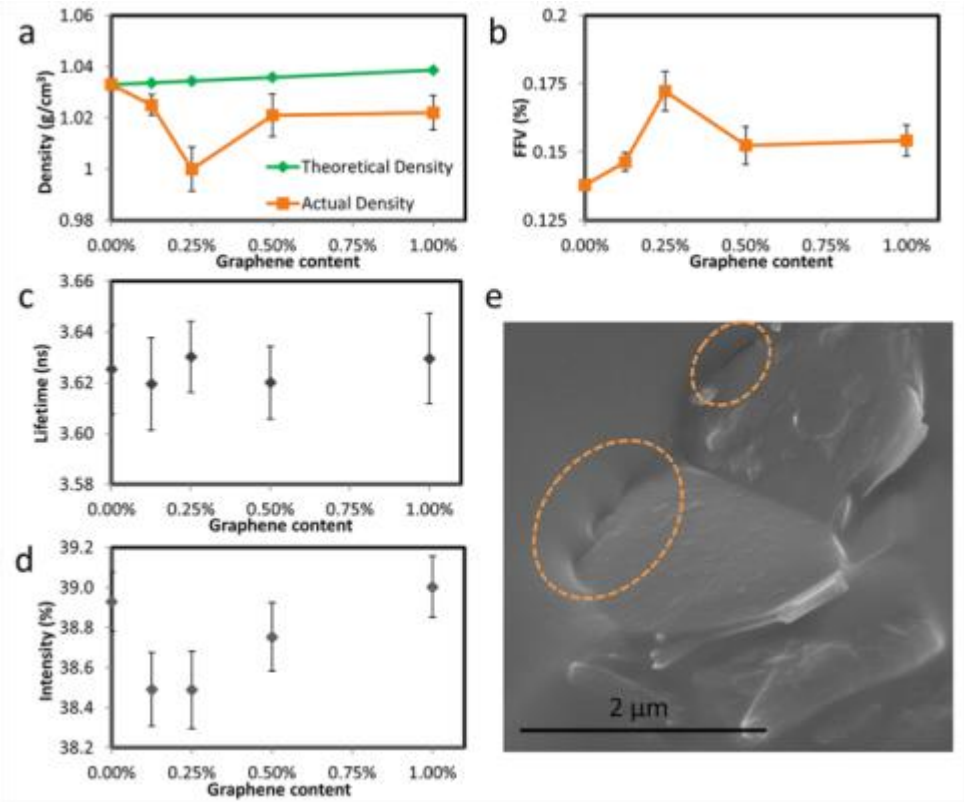

Figure 9. Density andFFV study of the membranes. The effect of various weight amounts of graphene on (a) the density, relative to that calculated from simple mixing of the respective components (b) the resulting total FFV based on density measurements (c) PALS o-Ps lifetime (τ_3) parameters (d) PALS o-Ps intensity (I_3) parameters of the composite membranes. (e) Example SEM image of the 0.25 *wt*% nanocomposite membrane showing the formation of nano- to meso-sized voids around the flakes and that the polymer does not efficiently make strong bonds with the surface of the flakes.

To investigate the formation of voids greater than 20 nm in dimension, SEM was employed. The membranes were prepared for SEM observations using liquid nitrogen fracturing to give an accurate representation of the morphology of the cross-sections and a 20 Å thick coating of platinum was employed to prevent charging of the non-conductive membranes. An important observation to make from the example SEM image in Fig. 9e is what happens at the interface between the graphene and the PDMS. It can be seen that there is a creation of a void present at this interface. These nano- to meso-sized voids occur in the range of 25 to 250 nm, which are outside the detection limit of PALS and can be the reason for the discrepancy between the calculated FFV from density measurements and the PALS data. Another major observation from the SEM images is that the PDMS does not make strong bonds with the surface of the flakes during the polymerization process, reinforcing the lack of interaction between the materials

that is driving the formation of these voids. Such an effect is likely due to graphene's surface energy and intrinsic low wettability of individual flakes.

From example SEM images in Figs. 10a-d it can be seen that the best graphene flake dispersion is attained at 0.25 *wt*% graphene-PDMS (Fig. 10b). It appears that with the addition of graphene beyond this concentration, an increased agglomeration is found with multiple flakes forming bundles. Another key aspect to gain from the sample SEM images is understanding the orientation of the flakes within the membranes, which can greatly affect the diffusion path and therefore the permeation of the gas molecules. From Fig. 10b, it can be seen that the majority of flakes lie close to perpendicular to the diffusion path (parallel to the membrane's surface) for 0.25 *wt*% graphene-PDMS samples (highlighted by the dotted lines). However, such an effect is not seen for other concentrations (Figs. 10c, d).

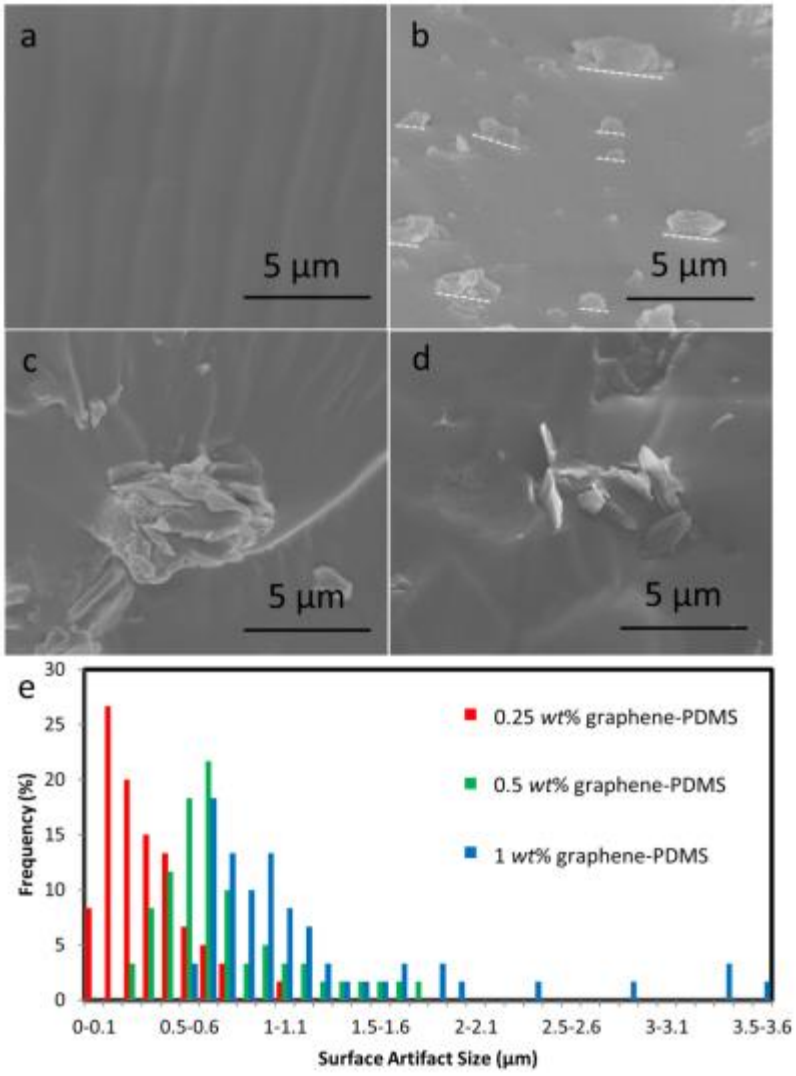

Figure 10. Cross-sectional SEM images of (a) pristine PDMS (b) 0.25 *wt*% graphene-PDMS (c) 0.5 *wt*% graphene-PDMS and (d) 1 *wt*% graphene-PDMS nanocomposite (e) Graphene flake size distribution, as a function of the artifacts seen on the surface, based from AFM analysis of membrane surface.

AFM at the surface of the membranes gives insight into the surface roughness and therefore relative surface artifact size distribution on the membranes (Fig. 10e). With the graphene samples being prepared using the same method before adding into the polymer, it can be assumed that any increase in the size of

surface artifacts is due to agglomeration of flakes. At 0.25 *wt*% the majority of surface artifacts' dimensions lie below 300 nm and increasing the graphene loading causes agglomerates to form larger artifacts where at 0.5 *wt*% the majority lie between 400 and 800 nm.

Equilibrium swelling measurements of the composite membranes was investigated and compared to a pristine PDMS reference to evaluate any changes in crosslinking density. The solvent uptake, or mass swelling degree (MSD), is presented in Fig. 11a. An increase in the chain length between the cross-links reduces the elastic resistance to the swelling stress and therefore increases the degree of swelling. The pristine PDMS complies with other studies for PDMS. It can be seen that all of the composites have a higher degree of swelling than that of pristine PDMS. Even with the addition of 1 *wt*% of graphene an increase in swelling of approximately 10% is observed, with the 0.25 *wt*% graphene to PDMS showing the lowest crosslinking density with a maximum chain length between crosslinks within the polymer. This minimum crosslinking density could represent an optimal dispersion of graphene flakes, allowing maximum interaction with the PDMS matrix and interfering with the normal crosslinking structure of the polymeric matrix.

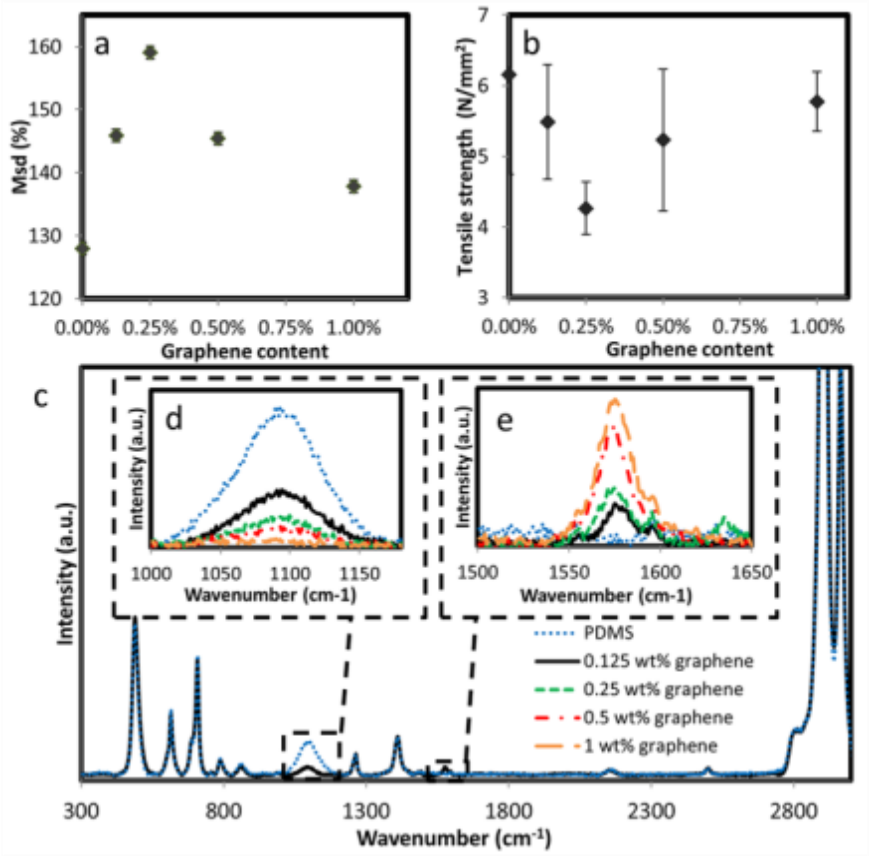

Figure 11. The effect of various weight amounts of graphene on the nanocomposites. (a) Crosslinking density study of the nanocomposites based on MSD. (b) Maximum tensile strength of the nanocomposite membranes. (c) Raman spectra of pristine PDMS and 0.125 *wt*% graphene-PDMS composite membranes. Inset: (d) comparison of the second order Si–O bond and (e) comparison of the G band.

The decrease of crosslinking density, shown in the MSD results, is also confirmed through tensile strength measurements (Fig. 11b). The reduction in elastic resistance and tensile strength are seen with the same trend as the swelling measurements, with most variance lying within the range of uncertainty. The graphene flakes affect the polymerization process, inhibiting the crosslinking bonds created and therefore producing a looser polymeric matrix with less tensile strength.

An investigation into the different bonds formed by the pristine PDMS and nanocomposite membranes was undertaken using micro-Raman spectroscopy. All membranes contained similar PDMS peaks regardless of the concentration of graphene added, with all the peaks in agreement with typical signatures reported in previous work. The composite materials however, also show the addition of Raman shift peaks representative of graphene. These include a clear G band and a 2D band that is almost non distinguishable in our samples. These peaks have been widely studied and occur at approximately 1570 and 2700 cm^{-1},respectively. The whole Raman spectra for the pristine PDMS and the 0.125 *wt*% graphene-PDMS membranes are shown in Fig. 11c.

Two major changes to the overall spectra of the composite materials are observed with the addition of graphene into the PDMS matrix. The first and most obvious is the addition of the sharp and distinctive graphene associated G graphitic band shown in Fig. 11e. This peak is formed from the fundamental resonance of the sp^2 carbon hybridization, which is not present in PDMS, and increases as the amount of graphene within the polymeric matrix is increased. However, the addition of graphene also has an influence on the alteration of the polymeric matrix, which can be seen when studying the second order Si–O peak occurring at approximately 1090 cm^{-1}(Fig. 11d). This weak, broad peak that occurs in pristine PDMS reduces in intensity as the amount of graphene in the polymer increases, vanishing at 1 *wt*% of graphene in PDMS. This represents a reduction in rigidity of the Si–O bond and probably the formation of irregular chains and decreased crosslinking density, which establishes the backbone of the PDMS polymer chain. No apparent change is seen for the first order Si–O bond peak at 488 cm^{-1}, which hints at the fact that the number of these bonds has not been reduced. FTIR, XRD and XPS were also employed to assess the bonding characteristics within the PDMS and nanocomposite membranes.

The FTIR spectra for the graphene-PDMS nanocomposites and the reference membranes (Fig. 12) comply with those typically reported for PDMS. It has been previously reported that Si–H bonds, which is located at 910 cm^{-1} and $Si(CH3)_2$ rocking peaks appear in the region of and 785–815 cm^{-1}. The Si–O–Si stretching multi-component peaks for PDMS is observed in the range between 930 to 1200 cm^{-1}.The peaks between 1400–1420 cm^{-1} and between 1240–1280 cm^{-1} corresponds to $–CH_3$ deformation vibration in PDMS.

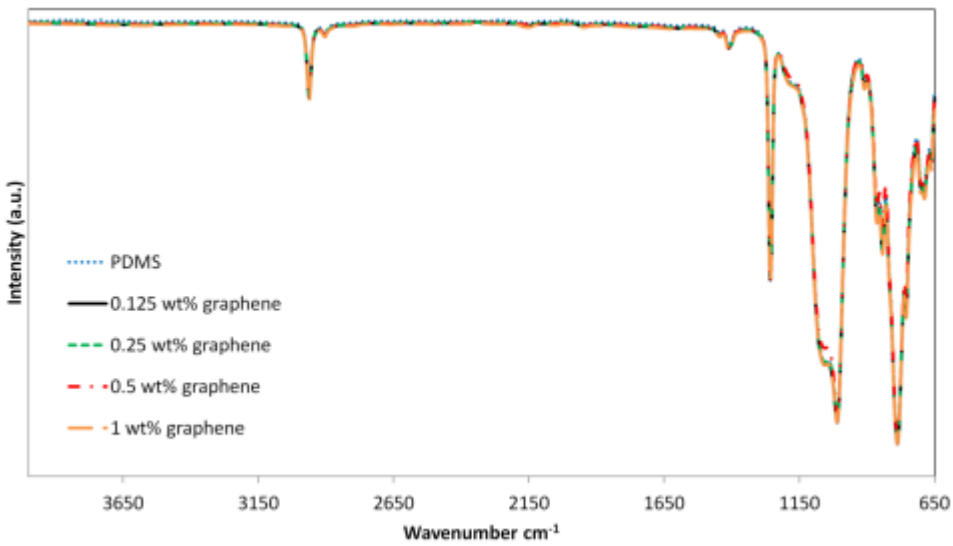

Figure 12. FTIR spectra of pristine PDMS and the graphene-PDMS nanocomposite membranes.

XRD was utilized to understand the changes in the polymeric structure of PDMS as a function of the concentration of graphene impregnated within the nanocomposite membranes (Fig.13). XRD data shows that graphene loading affected three key diffraction features of pristine PDMS film, observed at 7.1°,

8.5° and 14.1 2θ that correspond to a *d*-spacing of 14.45, 12.07 and 7.29 Å, respectively. These *d*-spacing's may be considered as large, medium and small chain spacing's, respectively, within the PDMS matrix. The change in the size of these polymeric structures can be directly associated with the changes in the structure of the polymer chains due to graphene impregnation.

It is evident that even with the smallest amount of graphene loading in PDMS, the distribution of the chain spacing shifts remarkably. In particular the average chain spacing in the PDMS polymer appears to shift from 7.3 Å in the pristine polymer to 7.8 Å at 0.125 *wt*% graphene and 8.1 Å at 1 *wt*% graphene, suggesting that the PDMS crosslinks formed in the presence of the graphene flakes are extended, relative to the pristine polymer. A further interesting change is also observed for the large spacing of 14.45 Å, where at 0.25 *wt*% graphene-PDMS there is no occurrence of this spacing. This is likely due to an increased dispersion where there are fewer larger agglomerates that are able to produce this larger spacing and therefore alter the polymer chain stacking.

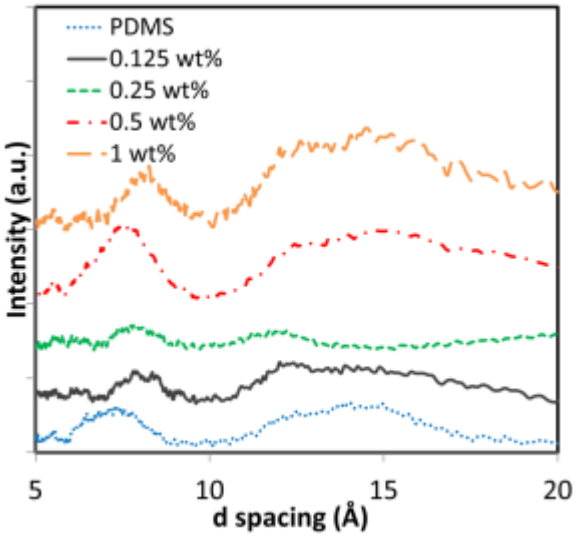

Figure 13. XRD patterns for PDMS and graphene-PDMS nanocomposites with *x* axis converted from 2θ to *d* spacing using Braggs law.

The pure gas permeation rates of the pristine PDMS and composite graphene-PDMS membranes were investigated under exposure to CO_2, N_2, Ar and CH_4 (99.99%) using the CPVV experimental setup described in the methodology section.

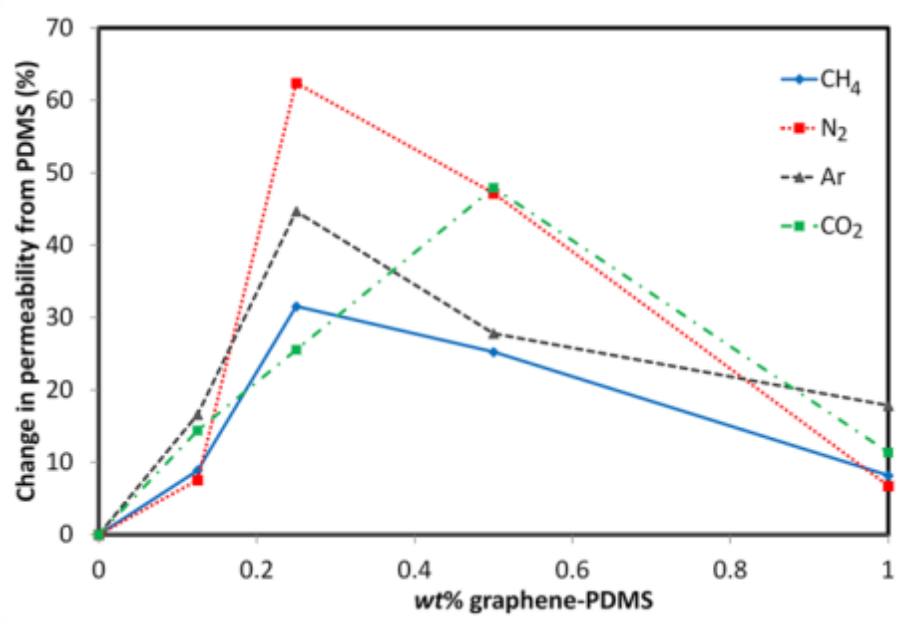

Figure 14. Change in permeability for each gas species with respect to the change graphene concentration.

As can be seen in both Table 1 and Fig. 14, the permeation of all gas species significantly increases with the addition of graphene as a filler to the PDMS matrix. The permeability of the pristine PDMS membrane are similar and correspond to the permeability found in the literature.

Table 1. Gas separation performance of PDMS membranes with different graphene concentrations.

	Percentage weight of graphene in the composite membrane					
	Penetrant	PDMS	0.125 *wt*%	0.25 *wt*%	0.5 *wt*%	1 *wt*%
Permeability (Barrer)	CH_4	850 ± 20	930 ± 15	1120 ± 18	1070 ± 17	920 ± 19
	N_2	380 ± 15	400 ± 18	610 ± 12	550 ± 14	400 ± 22
	Ar	710 ± 17	830 ± 19	1030 ± 16	910 ± 17	840 ± 20
	CO_2	3020 ± 16	3450 ± 21	3790 ± 12	4460 ± 18	3360 ± 18
Selectivity	CO_2/N_2	7.9 ± 0.37	8.6 ± 0.46	6.2 ± 0.14	8.1 ± 0.24	8.4 ± 0.53
	CO_2/CH_4	3.6 ± 0.10	3.7 ± 0.08	3.4 ± 0.06	4.2 ± 0.08	3.7 ± 0.10

A maximum permeability for Ar, N_2 and CH_4 was found at 0.25 *wt*%graphene loading, providing a greatly enhanced flux of over 60% in the case of N_2 for the composite membranes. A maximum permeability for Ar, N_2 and CH_4 was found at 0.25 *wt*%graphene loading, providing a greatly enhanced flux of over 60% in the case of N_2 for the composite membranes. However, at this condition, there is some minor loss of selectivity, consistent with the Robeson trend of falling selectivity when permeability increases. Interestingly for CO_2, while the 0.25 *wt*% graphene-PDMS membrane showed an increase in permeation,

it was the 0.5 *wt*% membrane that provided the greatest flux. This difference in the behavior of CO_2, with greater permeation at 0.5 *wt*%, whilst the other gas species maximum permeation occurs at 0.25 *wt*%, may be ascribed to the high affinity of graphene towards CO_2. Importantly, this increase in permeability at 0.5 *wt*% is achieved with no loss of CO_2/N_2 selectivity. It appears that CO_2/CH_4 selectivity increase slightly rising from 3.6 for pristine PDMS to 4.2 for the 0.5 *wt*% composite. In general, it can be seen that most of the changes in selectivity lie within the error range, revealing that the increase in permeability has come without major loss in selectivity. This is an important factor in the application of these membranes for gas separation.

Gas permeation through a rubbery polymer is dictated by the solution-diffusion mechanism. This mechanism comprises three steps: (1) adsorption at the upstream boundary, (2) diffusion through the membrane and (3) desorption on the downstream boundary. The increase in permeation for all gases is due to the change in diffusion of the gas molecules through the composite material. When referring back to the solution-diffusion model for gas permeation, the kinetic diameter of the penetrant and the FFV have direct effects on the diffusion coefficient. Ar, N_2, CO_2 and CH_4 kinetic diameters are 3.4, 3.64, 3.3 and 3.8 Å, respectively. The diffusion of gas molecules through the membranes depends on the molecules' ability to undertake diffusive jumps within the polymer, the smaller the molecule or the larger the free volume, the more rapid these diffusive jumps will occur. These diffusive jumps take place when the polymer chains dynamically form temporary voids, large enough to accommodate the penetrant, only in the immediate area of the gas molecule. A change in diffusivity and therefore permeation in a rubbery polymer is often attributed to an increase in FFV.

The presence of graphene in the PDMS matrix has the ability to create permanent voids at these interfaces facilitating diffusion, where the distance between the oligomers and the graphene flakes is different than the distance between the oligomers themselves under normal crosslinking conditions. Therefore the introduction of graphene into the PDMS matrix increases the amount of free volume within the polymer and thus giving rise to an increase in permeation.

The gas permeation mechanisms through the graphene-PDMS nanocomposite membranes differ from other carbon nanomaterial composites previously reported. In reality, the surface energies of other forms of carbon are very different from those of graphene with no dangling bonds. Carbon fillers, other than graphene, have been used for making permeable composite membranes, generally they have been shown to reduce permeability.

Carbon black has been generally shown to reduce the gas permeability. While nanocomposites containing CNT's have been demonstrated to either decrease or increase the permeation base on the type of gas species, the surface treatment used and also the orientation of the CNTs in the composite. In many of these reports the increase in permeation has been ascribed to a tunneling effect and the reduction in permeation to a sieving effect bestowed upon by the added CNTs. However, most of these works have ignored the possible effect of the interfacial voids formation. The lack of interaction between the graphene flakes, which was presented in our work, and PDMS has not been reported in CNT-PDMS composite materials.

Three dimensional (3D) carbon nanoparticle fillers, such as buckyballs, have been shown to increase FFV within the composite membrane thus increasing gas permeation through the composite. However, such increases has only been seen in functionalized buckyballs, which are well distributed within the polymer matrix and disrupting the polymer chains by making bonds with them. This is the opposite of what we presented in this work.

There are just a few studies of graphene loaded composites in regard to gas permeation. However they have only reported decreases in gas permeation, this is most likely due to the relatively large quantity of graphene used in their studies, causing a greater increase in the diffusion path length from the non-permeable graphene flakes. With most studies choosing to functionalize the graphene flakes to maximize interaction and compatibility between the base polymer and the flakes, therefore not allowing the formation of any interfacial void.

There are several reports on the incorporation of functionalized graphene flakes into PDMS at different aspect ratios and various concentrations of the flakes. For example, Adamson et.al. and Ozbas *et. al*.

demonstrated a decrease in the overall gas permeation of the graphene-PDMS nanoscomposites at high concentrations of functionalized graphene flakes and also showed that a larger aspect ratio (aspect ratio of 1000 in comparison to 400 at the same concentration of 1 *wt*%) resulted in a decrease of ~20% in gas permeation. At 1 *wt*% of functionalized graphene loading they observed a ~50% reduction in gas permeation compared to pristine PDMS. The outcomes however, are in contrast with the increase in the gas permeability of our non-functionalized graphene-PDMS nanocomposites presented in this work.

Some studies of PDMS and PDMS nanocomposite membranes have also reported an increase in gas permeability, although moderate. An ideal crosslinking temperature was found to increase the FFV in the polymeric matrix and therefore enhancing the permeation of all gas species tested against. Silicatite particles have also been shown to enhance CO_2's permeation through PDMS, increasing the permeability from the base 3000 to 3835 Barrer. However, the permeability of all other gases tested was found to decrease due to a molecular sieving effect. Of these membranes none show an ability to improve gas permeation to the degree demonstrated in this study.

For describing the permeation performance of the composite membranes two competing factors should be considered. The introduction of extra FFV, through interfacial voids, drives an increase in permeability. In contrast, gas transport across the added impermeable graphene flakes is harder, which naturally increases the diffusion path length for the gas molecules (Fig. 15a). This interfacial void created between the polymer and the graphene is similar to that was found by Cong *et. al*. where it was observed that gas permeation through poly(2,6-diphenyl- 1,4-phenylene oxide) (BPPOdp) increased when silica nanoparticles were dispersed through the polymer. This increase in permeation was attributed to the introduction of what they referred to as a nanogap. Where, the interaction between the nano-filler and the polymer caused the introduction of permanent voids at the filler-polymer interface, thus increasing FFV and permeability.

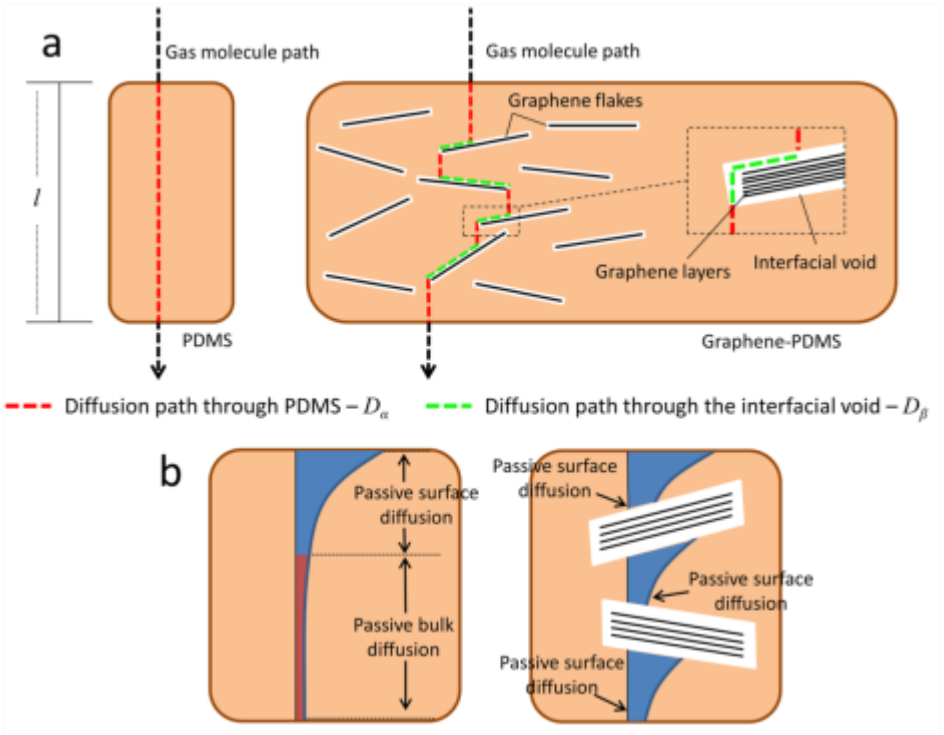

Figure 15. (a)A schematic of the diffusion paths for PDMS and graphene-PDMS nanocomposites of thickness *l*. The total path length for pristine PDMS membrane is *l*. In the graphene-PDMS nanocomposite membrane, the diffusion path through PDMS (D_α) shown in red and diffusion path through the interfacial void (D_β) shown in green, where, $\sum D_\alpha < l$ but $\sum D_\alpha + D_\beta > l$. (b) A schematic depicting the difference between passive surface and bulk diffusion of the gas molecules in pristine PDMS and graphene-PDMS nanocomposite membranes.

The 2D planar morphology of the graphene with its intrinsically high specific surface area results in an alteration of the polymeric matrix. As shown in the Raman spectra (Fig. 11d) a decrease in the second order vibration of the Si–O bonds due to the reduction in crosslinking density, resulting in a more relaxed polymeric matrix as shown with tensile strength (Fig. 11b) and swelling tests (Fig. 11a) as well as increasing the FFV through the formation of nano- and meso-sized voids (Figs. 9b and e). The change in polymeric matrix acts to alter the oligomer chains in relation to the graphene flakes changing the regular crosslinking structure within PDMS. The PALS intensity data (Fig. 9d) therefore strengthens the case that higher graphene content is not as well dispersed within the PDMS matrix due to agglomeration resulting in less inhibition with the PDMS crosslinking therefore improved mechanical properties (increased tensile strength and reduced swelling).

The maximum formation of these voids was found to occur at 0.25 *wt*% graphene-PDMS which was ascribed to an increased dispersion of graphene flakes found at this concentration. This could effectively increase the number of interfaces between the graphene and PDMS where at concentrations higher than 0.25 *wt*% the graphene flakes start to agglomerate and therefore reducing the number of interfaces. The introduction of additional interfaces after the graphene loading can directly impact upon the gas permeability by producing nano- to meso-sized along the surface of the flakes, facilitating the gas transport. The total gas molecules diffusion path length increases by adding graphene flakes. However, as these molecules spend most of their time in the interfacial voids, their diffusion rate is much higher, which results in a higher permeability than the pristine PDMS. The maintaining selectivity with the increase in permeability implies the interfacial voids do not create an interconnected pore through the membrane and thus remain defect free.

When implementing the membranes into a commercial gas sensing system, the performance of the graphene membranes in comparison with PDMS and no membrane present is shown in Figs. 16a and b. As can be seen, the sensor response for the graphene-PDMS nanocomposite membrane is almost the same as that of not having a membrane present at all. There is a slight attenuation and a delay of approximately 20 seconds. However, when comparing it to the PDMS reference membrane the composite material offers a far superior performance with less attenuation and a far quicker response. This effectively means the membranes are almost transparent to gas molecules and can offer effective solutions when monitoring gases while keeping the sensor isolated from the surrounding environmental contaminants. Interestingly, the Barrer number for CO_2 permeation (Table 1) reveals an increase of 50% but in the sensing experimental setup, the results show a response that appears greater than this number. It is important to consider that the measurements to obtain the Barrer number were performed using a high, fixed pressure difference across the membranes. However, the sensor measurements are conducted with negligible pressure difference across the membranes. As a result, an effective passive gas diffusion that is not necessarily driven by pressure is the reason for the enhanced performance of the membranes for sensing applications. It is known that such passive diffusion follows Ficks second law of diffusion, where near the surface the diffusion of gas molecules occurs more facile and can be approximated using:

$$C(x,t) = \mathrm{C_s}\left(1 - \frac{2}{\sqrt{\pi}}\mathrm{erf}\left(\frac{x}{2\sqrt{Dt}}\right)\right) \qquad (4)$$

where C is the concentration at distance x from the surface at time t, Cs is the fixed concentration of gas molecules at the surface, D is the diffusion constant and erf is the error function. This approximation is only valid near the surface boundary while the diffusion far from the surface, in the bulk, reduces to a constant rate. By producing voids using the graphene flakes, more of this surface effect is produced and the passive surface diffusion, which has a much higher rate, according to the Fick's second law becomes the dominant effect of the gas molecule diffusion. While in only PDMS membranes the constant rate which is equal to that one obtained by the Barrer measurements dominate the system (Fig. 15b).

To evaluate the membranes' capability for effective phase separation, CO_2 was dissolved into DI water with the membranes placed in between the liquid and the sensor directly at the sensor head. As can be seen from comparing Figs. 16c and d as well as Table 2, the addition of graphene into the PDMS matrix

has made the membrane more hydrophobic. PDMS itself is known as a hydrophobic material and so is graphene.

Through this added hydrophobicity and increased gas permeability, the graphene nanocomposites act as a high throughput phase separating membranes, as can be clearly seen in Fig. 16e. This allows for efficient transfer of gas molecules, while stopping the liquid from permeating.

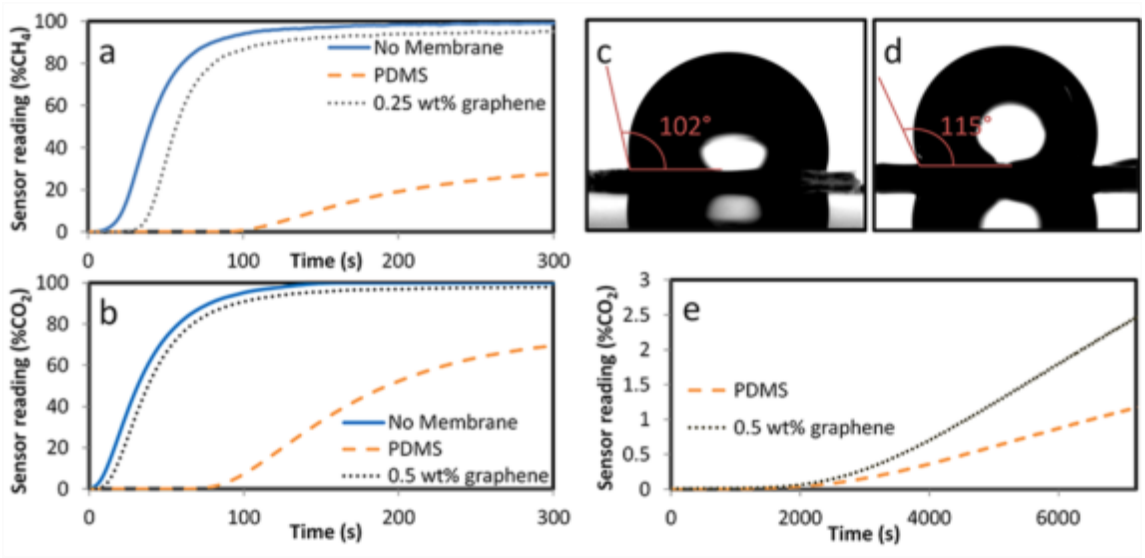

Figure 16. Applications of nanocomposite membranes.Sensor reading for (a) CH_4 and (b) CO_2 permeation. (c) Water droplets contact angle for PDMS. (d) Water droplets contact angle for 0.5 *wt*% graphene-PDMS. (e) Sensor reading for dissolved CO_2 in deionized water (DI), phase separation through PDMS and 0.5 *wt*% graphene-PDMS.

Table 2. Water contact angles for pristine PDMS and the graphene-PDMS nanocomposite membranes.

Material	Contact Angle (°)
PDMS	102
0.125 *wt*% graphene-PDMS	118
0.25 *wt*% graphene-PDMS	116
0.5 *wt*% graphene-PDMS	115
1 *wt*% graphene-PDMS	115

3.1.3 MoS_2-PDMS nanocomposite membranes

2D MoS_2 flakes were prepared from MoS_2 bulk powder using a grinding-assist liquid phase exfoliation technique with the composites synthesized via in situ polymerization method using N-Methyl-2-pyrrolidone (NMP) and ethanol/water ($EtOH/H_2O$) solution.For the MoS_2 flakes exfoliated in NMP the average lateral dimensions are approximately 53 nm and the average thickness ranges below 3 layers and for the flakes exfoliated in $EtOH/H_2O$ the average lateral dimensions are approximately 55 nm and the average thickness ranges below 4 layers (Fig. 17). High-resolution transmission electron microscopy

(HRTEM) shown in Fig.18a reveals the crystal structure with a lattice spacing of 0.27 nm assigned to the (100) plane.

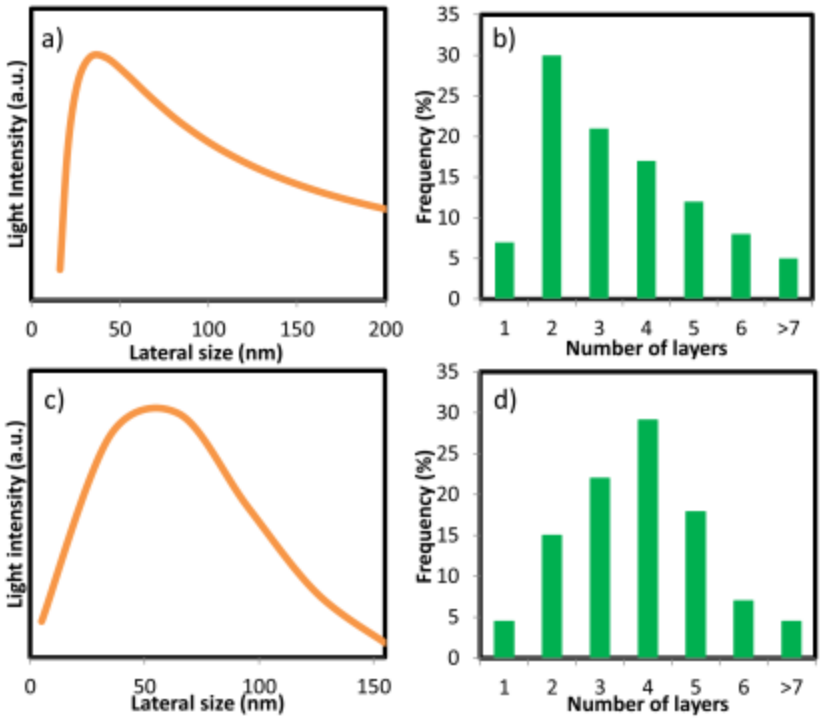

Figure 17.(a) Distribution of MoS_2 nanoflakes exfoliated in NMP based on DLS assessment. (b) Distribution of MoS_2 nanoflakes exfoliated in NMP thickness taken from the analysis of 100 flakes using AFM. (c) Distribution of MoS_2 nanoflakes exfoliated in EtOH/H_2O using DLS. (b) Distribution of MoS_2 nanoflakes exfoliated in EtOH/H_2O thickness taken from the analysis of 100 flakes using AFM.

Raman spectroscopy is also utilized to further investigate the crystal structure and thickness of the 2D MoS_2 flakes. From Fig. 18b, two distinguished Raman shift peaks can be found at ~381 and ~408 cm^{-1} for the MoS_2 bulk powder, corresponding to in-plane (E^1_{2g}) and vertical plane (A_{1g}) vibrations of Mo–S bonds in MoS_2, respectively. By normalizing both the Raman spectra taken from the bulk powder and flakes with the E^1_{2g} mode, it is found that the 2D flakes have a smaller Raman shift difference between E^1_{2g} and A_{1g} modes (Δ = ~20 cm^{-1}) in comparison with Δ = ~27 cm^{-1} from their bulk counterpart. Using information provided by Li *et. al.*, the Raman spectra indicate that the thicknesses of 2D MoS_2 flakes lie in between one to two layers thick where this is also supported through AFM (Fig.17).

The UV-Vis absorbance spectra from the composite materials were used to analyze yield and concentration of distributed MoS_2 within the composite material (Fig.18d). The concentration of the membranes using the absorbance measurements as described by O'Neill *et.al.*, found that the MoS_2-PDMS composites where the flakes were exfoliated in NMP were approximately 0.011 and 0.021 wt% and the composites where the flakes were exfoliated in an ethanol and water solution were 0.0051 and 0.01 wt.% for the low and high concentrations respectively. Revealing that the low concentration of MoS_2 exfoliated in NMP shows almost the same as the high concentration of MoS_2 exfoliated in ethanol water solution. The peak at 490 nm is characteristic of PDMS where the MoS_2 absorbance peaks are not present due to the small concentrations within the composites. However the enhancement of this peak in the composites is due to the presence of 2D MoS_2. The inherent PDMS bonds are not affected by the low concentrations of MoS_2 added within the composite where only Van der Walls forces are present between the oligomers and flakes themselves based on FTIR assessments and Raman of the composites (Figs.19 and 20).

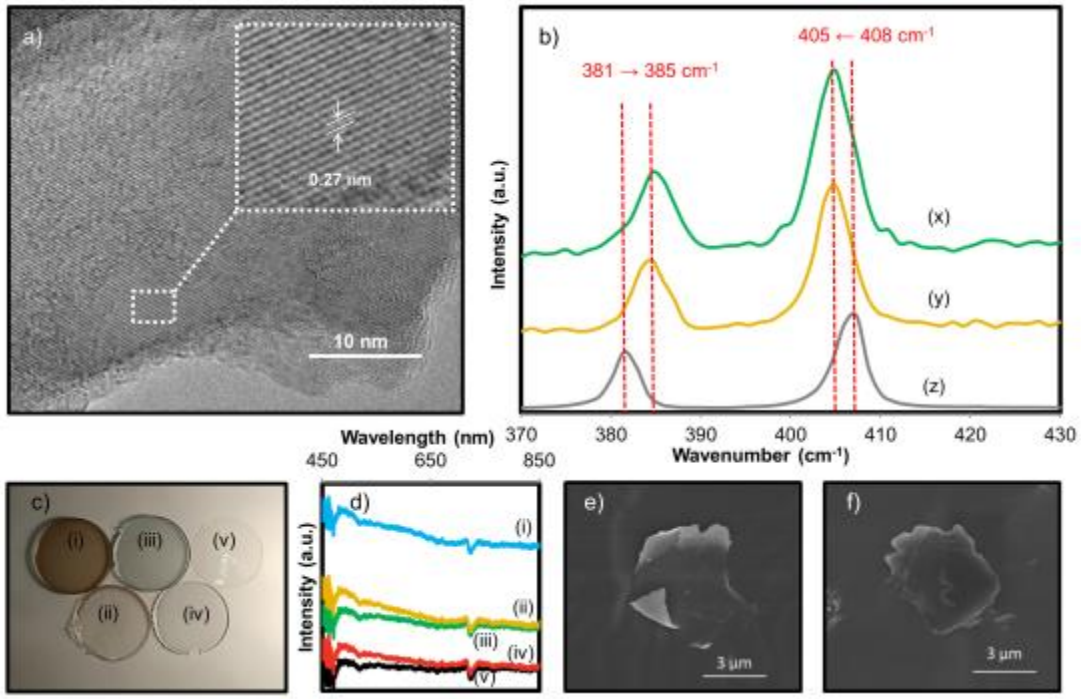

Figure 18. MoS_2 flake morphology and dispersion within the nanocomposite membranes. (a) TEM image of MoS_2 flake. (b) The Raman spectra of(*x*) MoS_2 exfoliated in NMP (*y*) MoS_2 exfoliated in EtOH/H_2O (*z*) Bulk MoS_2 (c) Images of the polymer composites and (d) The effect of various solvents used for exfoliation of MoS_2 on the UV-Vis spectra of the nanocomposites showing relative loading concentration of the different membranes. (*i*) MoS_2 exfoliated in NMP high concentration (*ii*) MoS_2 exfoliated in NMP low concentration (*iii*) MoS_2 exfoliated in EtOH/H_2O high concentration (*iv*) MoS_2 exfoliated in EtOH/H_2O low concentration (*v*) Pristine PDMS (e) SEM image of MoS_2 dispersion and morphology in PDMS exfoliated in NMP(f) SEM image of MoS_2 dispersion and morphology in PDMS exfoliated in EtOH/H_2O.

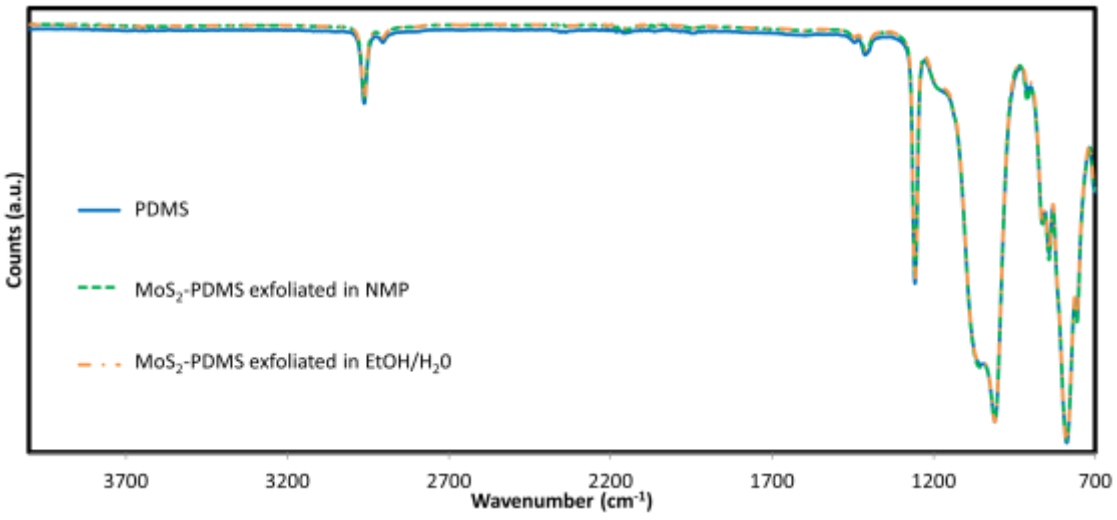

Figure 19. FTIR spectra comparing pristine PDMS with the MoS_2-PDMS nanocomposites

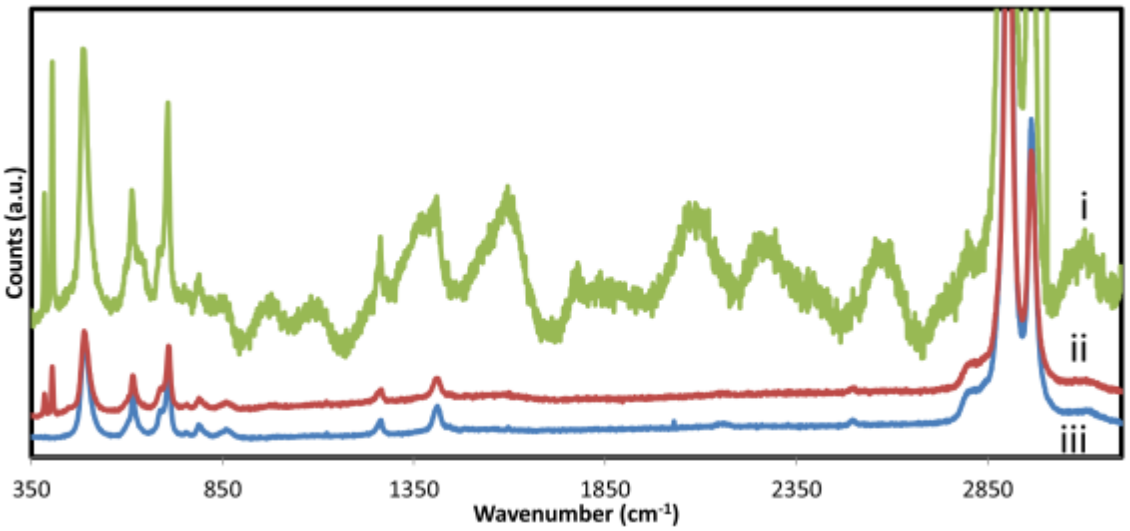

Figure 20. Raman spectra of (i) 2D MoS_2-PDMS with 2D MoS_2 exfoliated in NMP (ii) 2D MoS_2-PDMS with 2D MoS_2 exfoliated in EtOH/H_2O (iii) pristine PDMS

The pure gas permeation rates of the pristine PDMS and composite MoS_2-PDMS membranes were investigated under exposure to CO_2, N_2, and CH_4 (99.99%) using the CPVV experimental setup.

As can be seen in and Fig. 21, the permeability of the pristine PDMS membrane is similar and correspond to the permeability found by Merkel *et al.* that also used a CPVV experimental set up. A key aspect of these results shows that the addition of MoS_2 at these low concentrations has had no significant penalty to the permeation of CH_4 and N_2. However, permeation of CO_2 is significantly decreased with the addition of MoS_2 into the PDMS matrix with permeability being inversely but proportional to concentration. While the concentration of MoS_2 flakes within the MoS_2-PDMS composite membranes did not affect the permeation of CH_4 or N_2 it did significantly decrease the permeation of CO_2 gas molecules due to its calculated higher adsorption energy to single layer MoS_2.

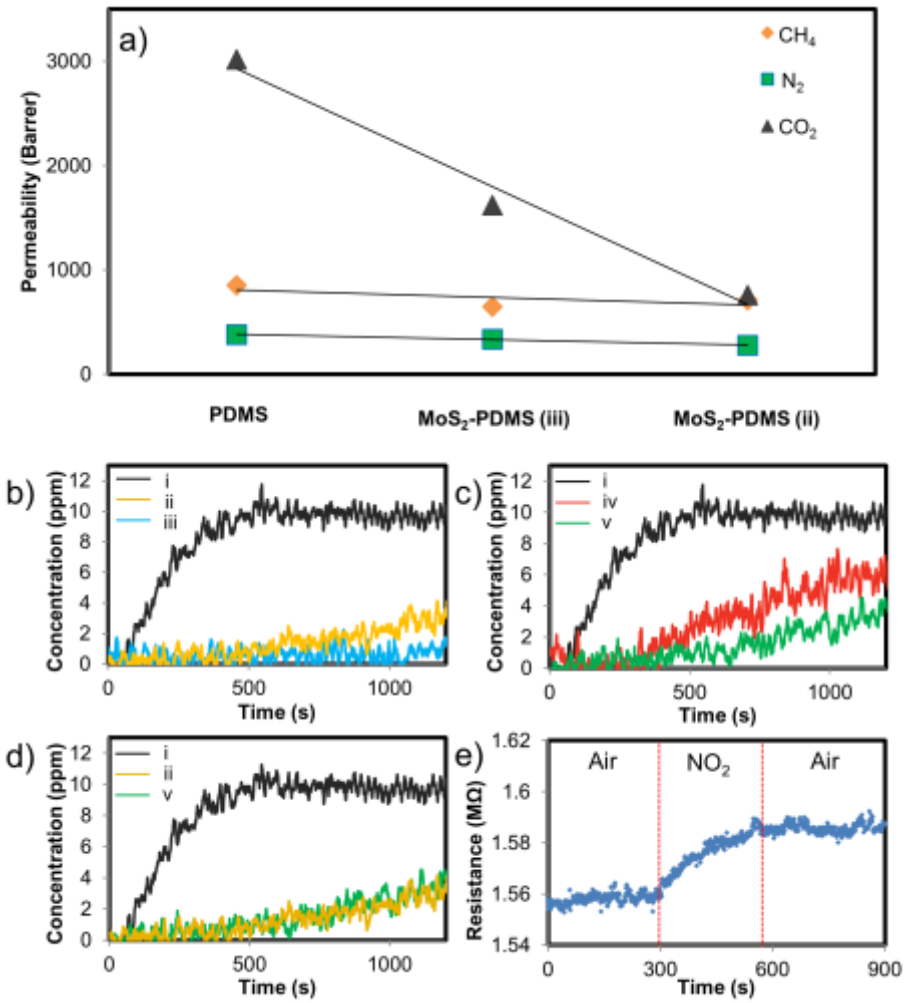

Figure 21. (a) Pure gas permeation results for composites with the MoS_2 exfoliated in NMP.(b) NO_2 permeation: PDMS vs NMP exfoliated MoS_2 nanocomposites (c) NO_2 permeation: PDMS vs Ethanol and water exfoliated MoS_2 nanocomposites (d) NO_2 permeation: PDMS vs similar concentrations of MoS_2 exfoliated in different solvents, where: i-PDMS membrane; ii-MoS_2-PDMS (exf. NMP low concentration); iii-MoS_2-PDMS (exf. NMP high concentration); iv-MoS_2-PDMS (exf. EtOH/H_2O low concentration); v-MoS_2-PDMS (exf. EtOH/H_2O high concentration) (d) MoS_2 resistance before, during and after NO_2 exposure.

The experimental method shown by Nour *et al.* for H_2S separation was employed for the NO_2 separation experiments. As seen in the dynamic responses of the NO_2 sensor shown in Figs. 21b-d there was a major effect on the NO_2 gas permeation through the addition of 2D MoS_2 flakes. The change in NO_2 permeation kinetics through analysis of response curves can be divided into two phases. The first phase represented by the delay in the sensor response curve reflects the gas molecules solubility and often referred to as the time lag method. Pristine PDMS shows a much faster NO_2 sensor response with a delay of less than 100 s compared to approximately 400 s for the lower concentration composite membranes. This indicates a decreasing NO_2 solubility for the nanocomposite membranes. It was noticed that as the concentration of MoS_2 flakes increased, the sensor delay was prolonged, which indicates an increase in the NO_2 solubility.

In the second phase, the gradient of the sensor response gives an indication of NO_2 gas molecules diffusivity through the composite membranes. It can be seen that the NO_2 molecules permeation kinetics, at this stage, were strongly dependent on the MoS_2 concentration in the membrane, in which higher MoS_2 concentrations resulted in lower diffusion. At the highest concentration of MoS_2 the permeation of NO_2

gas molecules is almost totally stopped. Although it has been shown that NMP residue is retained on the surface of the flakes after exfoliation if the drying process does not exceed 200 °C, this is also visible in the Raman spectrum shown in Fig.20. However, it appears that NO_2 adsorption is not affected by NMP present on the flake surface and therefor diffusion is not dependent on the exfoliation solvent (Fig. 22d). Since higher adsorption energy gives rise to a strong binding between adsorbate and the host, we can see stronger interaction between NO_2, CO_2 and MoS_2 monolayer compared to N_2 or CH_4. This is especially true when van der Waals interactions between the weakly bonded gas adsorption system is considered. However, there have been no thorough experimental studies regarding the adsorption of gas molecules on MoS_2 monolayers, thus all the adsorption energies are based on first principle calculations.

$$E_{ad} = E_{Gas+MoS2} - E_{MoS2} - E_{Gas} \quad (5)$$

Zhao *et. al.* calculated the highest adsorption energy to MoS_2 was held by NO_2 (Equation 5) in correspondence with our results. This strong adsorption energy is apparent in Fig.18e, during exposure to NO_2 the gas molecule act as an electron acceptor from the MoS_2 causing the resistance of the flake to increase, however after exposure there is no sign of recovery indicating the NO_2 gas molecules are still present adsorbed to the surface.

It is suggested that the NO_2 gas molecules adsorbed (as schematically shown in Fig. 22a) on the surface of the MoS_2 act as p-type dopants (electron acceptors). Theoretically this should cause an increase in the photoluminescence (PL) intensity, however, as seen in Figs 22b and c, PL quenching is observed after NO_2 adsorption. This could possibly be related to the effects seen by nonuniform doping profiles due to the induced defects during the exfoliation process of the flakes that may play a role in suppressing exciton formation and/or its radiative recombination. It is interesting to see that the intensity decreases by over 60% for the composite containing MoS_2 exfoliated in $EtOH/H_2O$ while the quenching of PL intensity only occurs by 35% for composites containing MoS_2 exfoliated in NMP. This is most likely associated with the residual NMP on the surface of the surface as previously discussed. The same experiment was run exposing the composites to ‘dry air’ as a control where a minor decrease in PL intensity is seen, approximately 15% (Fig.23).

Remarkably, at a relatively low loading concentration of 0.021 wt.% the MoS_2-PDMS composite membrane was able to completely block NO_2 gas permeation due to strong adsorption energy as depicted in Fig.22a. The PL results suggest that these composite membranes could be implemented into a device capable of not only separating NO_2 from gas streams but also monitoring the concentration of NO_2 if combined with a PL unit, offering dual functionality.

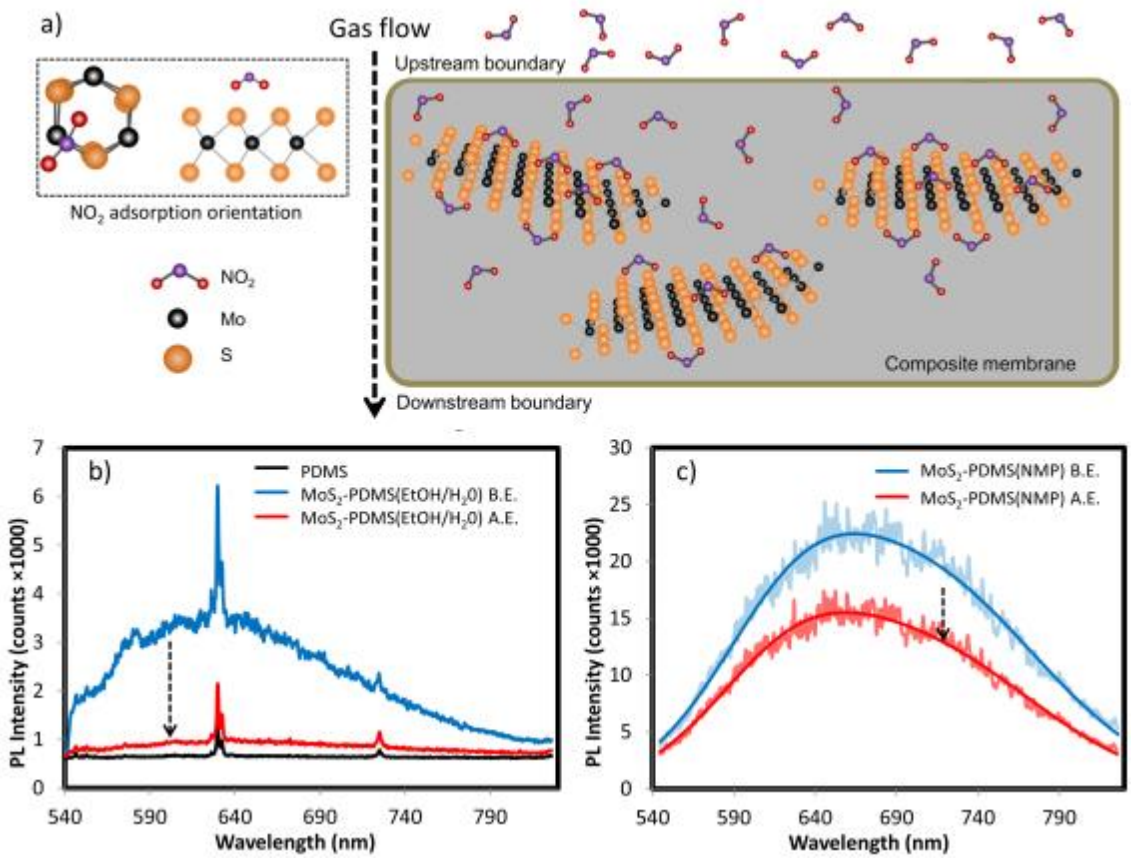

Figure 22. (a) NO_2 gas adsorption and orientationonto 2D MoS_2 flakes. (b) PL spectra of PDMS and composites exfoliated in EtOH/H_2O before NO_2 exposure (B.E.) and after NO_2 exposure (A.E.) (c) PL spectra of composites exfoliated in NMP before NO_2 exposure (B.E.) and after NO_2 exposure (A.E.)

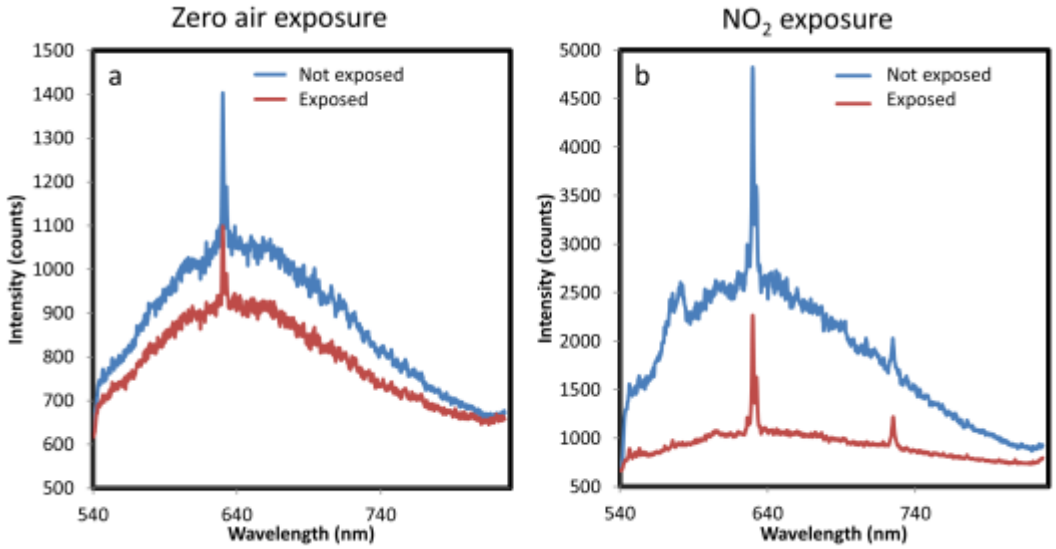

Figure 23. Photoluminescence spectra of: (a) MoS_2-PDMS composites before and after exposure to 'zero air' and (b) MoS_2-PDMS composites before and after exposure to NO_2.

3.1.4 Ag-PDMS nanocomposite membranes

The rubbery membranes were frozen in liquid nitrogen and then fractured to obtain acceptable cross sectional surfaces for SEM. Samples were then coated with a thin platinum layer of ~3 nm thickness to reduce charging effect. Fig. 24 shows a SEM image of the Ag-PDMS nanocomposite, which demonstrates the presence of dispersed nanoparticles embedded into PDMS.

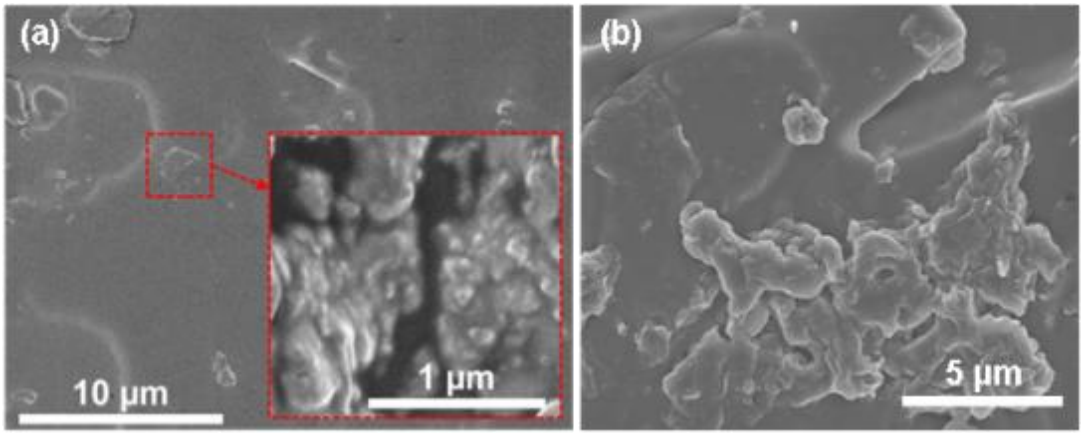

Figure 24. Cross-sectional SEM images of: (a) an Ag-PDMS nanocomposite membrane showing the dispersion of the embedded Ag nanoparticles at 0.25% concentration. (b) The agglomeration of Ag nanoparticles when their concentration in the PDMS matrix increases beyond 0.25%. Large islands of nanoparticles are formed in a 1% Ag-PDMS nanocomposite membrane which is shown as an example.

The TEM image of the pristine Ag in Fig. 25a shows the nanoparticles in the range suggested by the provider and confirms that their sizes are less than 100 nm. A very thin amorphous layer surrounding the Ag nanoparticle seen in the HRTEM image (Fig. 25b) can be identified as the PVP coating, similarly observed by other researchers. The selected area electron diffraction (SAED) pattern of the cubic phase of Ag can correspond to the planes (1 1 1), (2 0 0) and (2 2 0) (Fig. 25c). This was carried out based on calculations of the lattice spacings for the Ag nanoparticle, which is presented in Fig. 25d.

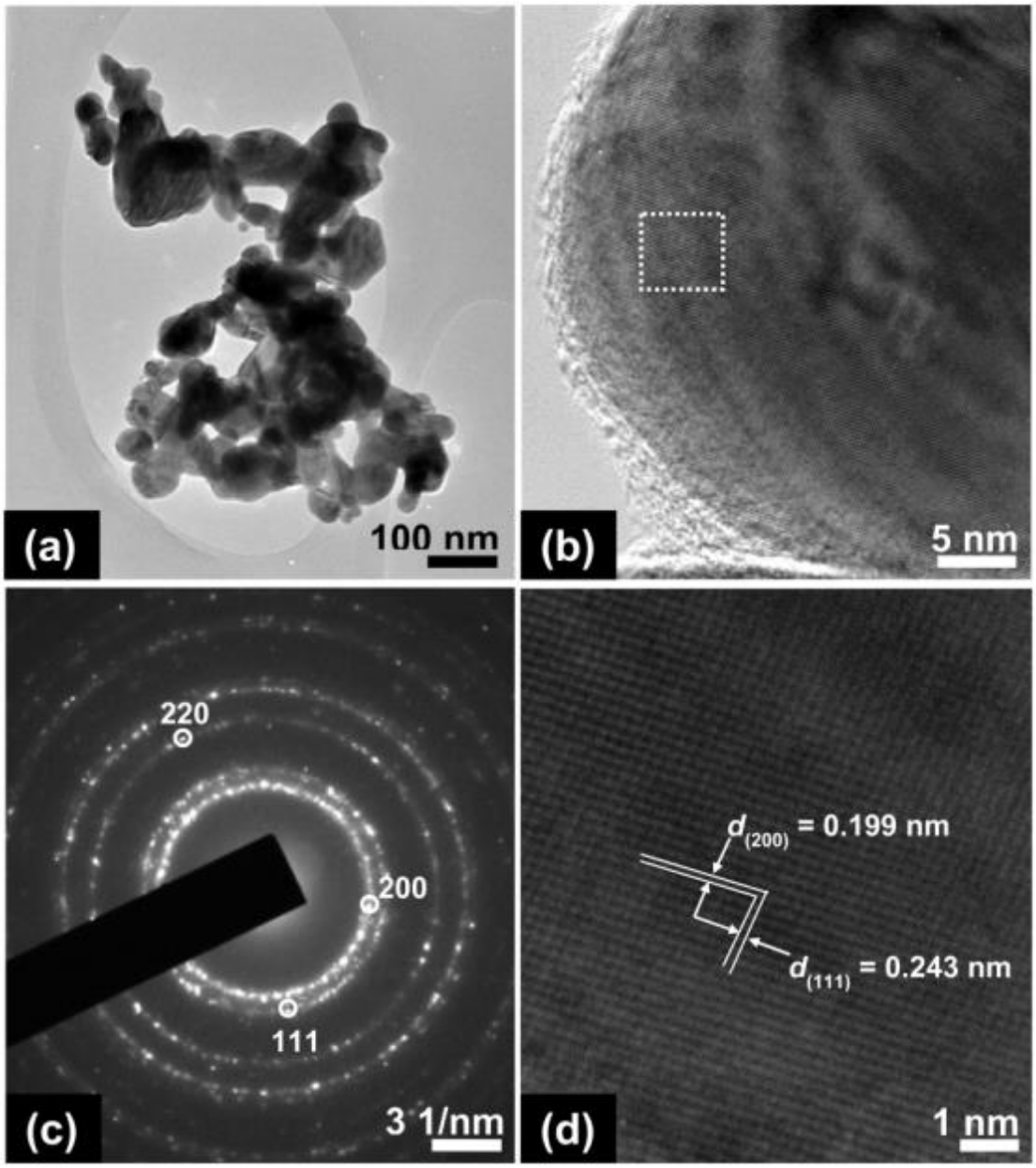

Figure25. (a) The TEM image of pristine Ag nanoparticles. (b) The HRTEM image of one pristine Ag nanoparticle. (c) The SAED pattern of pristine Ag nanoparticles. (d) The HRTEM image from the region enclosed in (b).

SEM and AFM of the membranes demonstrate that the best dispersions were obtained for 0.125 and 0.25 *wt*% Ag-PDMS nanocomposite with some agglomerations were seen for higher concentrations of Ag (Fig. 26). In addition, the sonication time during the membrane fabrication process was found to be independent to the dispersion quality of Ag within the PDMS solution (Fig. 27). This was also seen when looking at the surface hydrophobicity of the nanocomposites, where no observable change was detected with the addition Ag nanoparticles (Table 3). As a result, the change in hydrophobicity does not play a significant role in the adherence of bacteria to the surface of the control or nanocomposites.

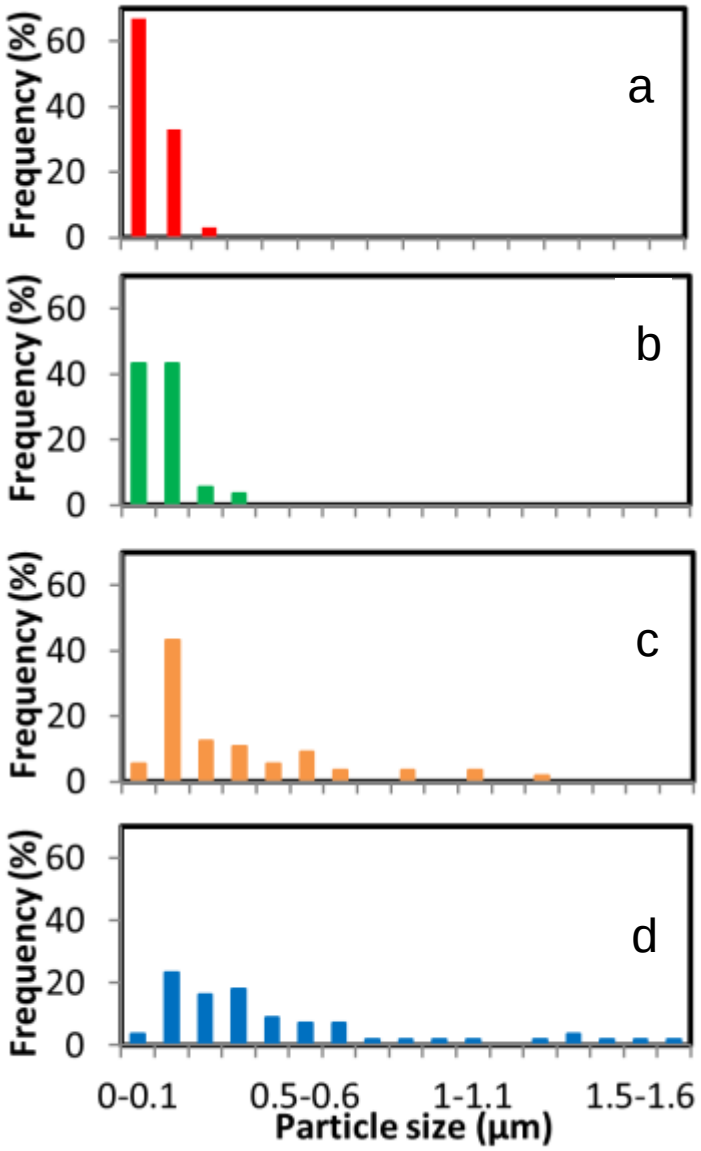

Figure 26. Particle size distribution of (a) 0.125 *wt*% Ag-PDMS, (b) 0.25 *wt*% Ag-PDMS, (c) 0.5 *wt*% Ag-PDMS and (d) 1 *wt*% Ag-PDMS based from AFM analysis of material surface.

Table 3. Water droplet contact angle of pristine PDMS and Ag-PDMS nanocomposites

Material	Contact Angle (°)
PDMS	114.2 ± 2.6
0.125 *wt*% Ag-PDMS	113.3 ± 3.5
0.25 *wt*% Ag-PDMS	112.7 ± 4.2
0.5 *wt*% Ag-PDMS	112.3 ± 1.4
1 *wt*% Ag-PDMS	113.3 ± 2.1

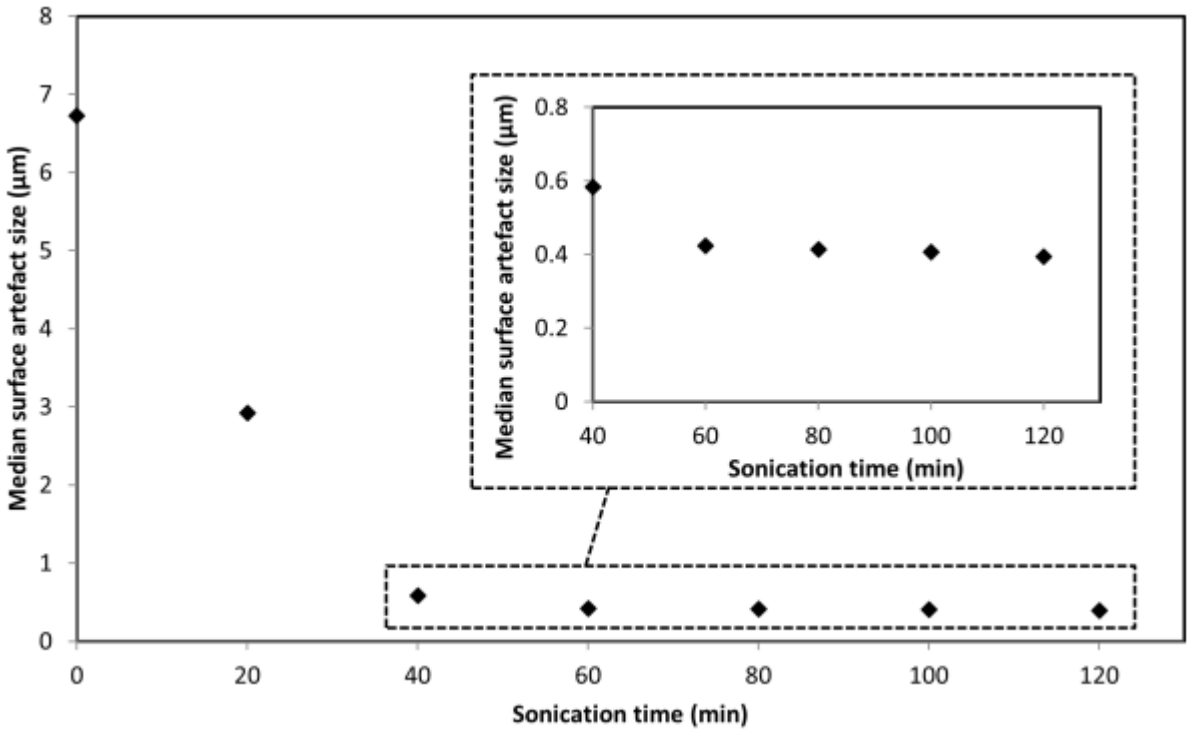

Figure 27. The effect of sonication time on particle dispersion based from AFM analysis of Ag-PDMS nanocomposite membrane surface.

Fig. 28 shows the FTIR spectra of pure PDMS and the Ag-PDMS nanocomposites membranes. Unfilled PDMS peaks comply with the typical reported values. The Si–C bands and $Si(CH_3)_2$ rocking peaks, respectively, are present in the regions of 825–865 and 785–815 cm^{-1}. Peaks that appear at 910 cm^{-1} are assigned to the Si–H bonds. The multi-component Si–O–Si stretching peaks are located between 930 to 1200 cm^{-1}. The notable difference between unfilled PDMS and different Ag/PDMS nanocomposites spectra is apparent at 1414 and 1450 cm^{-1}, which can be ascribed to C=O and C–C ring stretching bonds, respectively. Both peaks become more prominent as the concentration of Ag nanoparticles increases in the composite membranes (insert in Fig. 28). These bonds' intensity changes can be associated with the increase of the dispersant PVP coating.

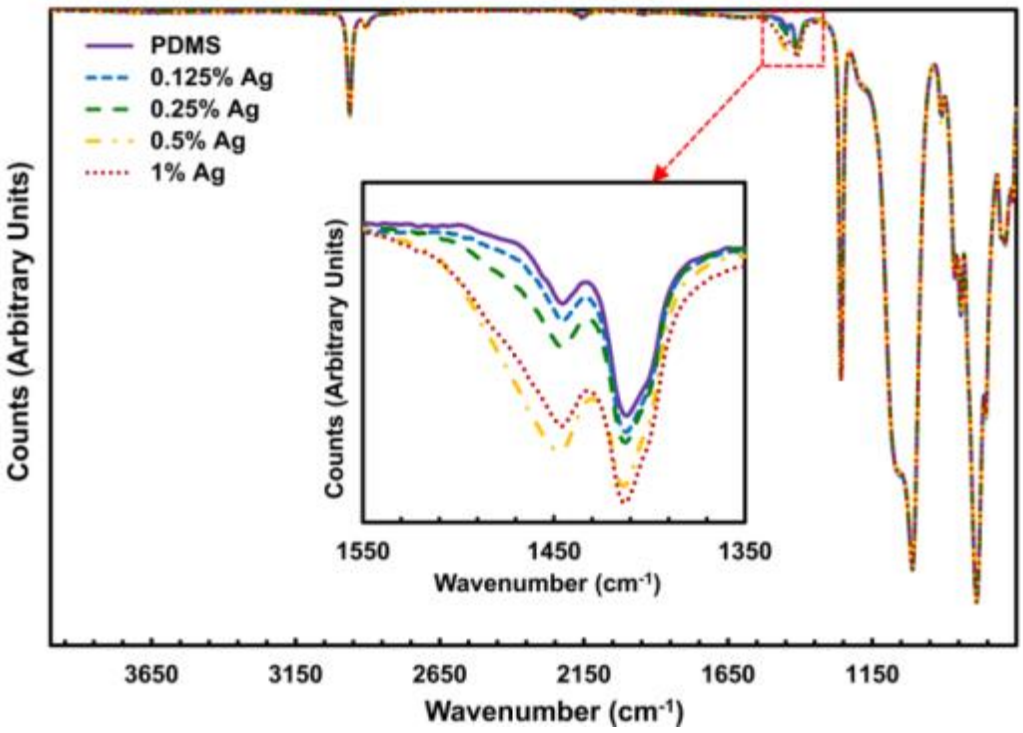

Figure 28. FTIR spectra for the unfilled PDMS and Ag-PDMS nanocomposite membranes.

Micro-Raman spectra of unfilled PDMS and different concentrations Ag-PDMS nanocomposites are presented in Fig. 29. Typical signature peaks of PDMS published in previous studies are in agreement with the obtained spectra. The spectra include a symmetric Si–O–Si peak around 488 cm^{-1}. The Si–CH_3 symmetric rocking peak appears at 615 cm^{-1}. At 707 cm^{-1}, the Si–C symmetric stretching appears. The peaks of the symmetric bending, symmetric and asymmetric rocking of –CH_3 appear at 787, 856 and 1257 cm^{-1}, respectively. The Si–CH_3 symmetric and asymmetric stretching bands appear at 2902 and 2964 cm^{-1}. The major change in spectra of nanocomposites with different Ag concentrations appear in the C–C stretching at 1567 cm^{-1}, in which intensities enhance as the concentration of Ag nanoparticles increases in the composite membranes. This can be attributed to the dispersant PVP coating, which is in agreement with the obtained FTIR results in this section.

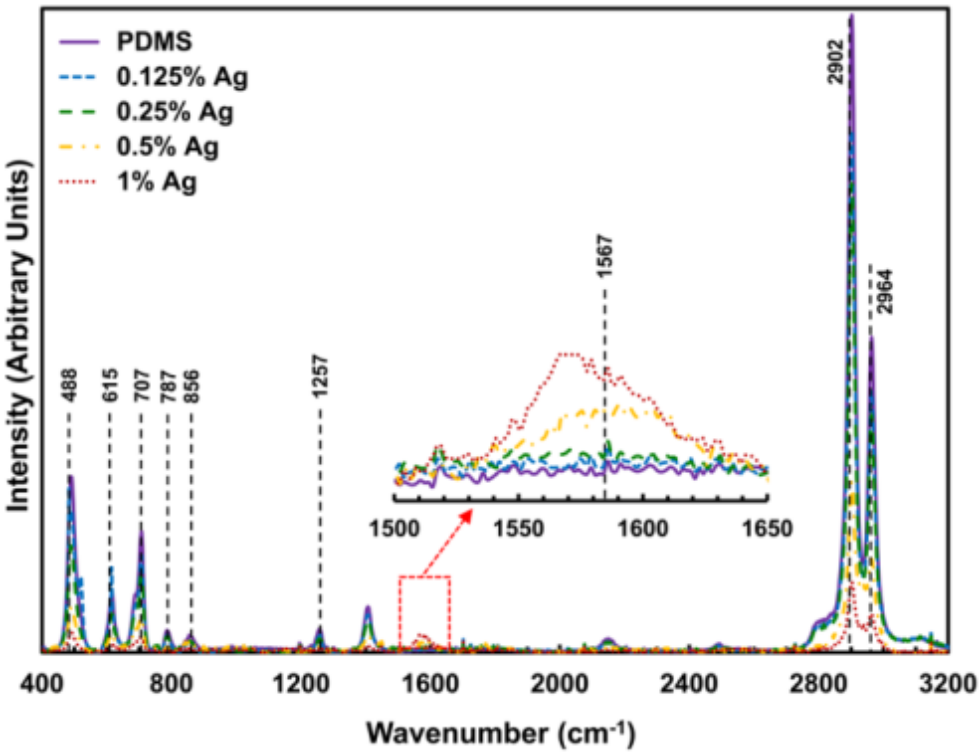

Figure 29. Micro-Raman spectra for unfilled PDMS and four different Ag concentrations in PDMS.

Before assessing the gas permeability through nanocomposite membranes, it is important to characterize their FFVs upon the addition of Ag nanoparticles, which can fundamentally change the diffusion of the gas molecules through the membranes. To understand this impact, density measurements were carried out as the polymer density is commonly associated with FFV. The density of the various weight concentrations of Ag composite catalytic membranes are shown in Fig. 30a. It can be seen that adding Ag nanoparticles up to 0.25% slightly reduces the density of the composite membrane relative to that of the predicted theoretical calculations. However, further increasing of Ag concentration does not reduce the density of membranes. This might be due to the agglomeration effect of Ag nanoparticles that starts to take place at higher concentrations (Fig.26). These density measurement results can be used for assessing the additional FFV that possibly caused by the weak interaction between the Ag nanoparticles and the base polymer (Fig. 30b). Such a weak interaction can be evident by the reduction of the ability to create crosslinks at the interface between Ag nanoparticles and PDMS. Equilibrium swelling measurements of the composite catalytic membranes was hence investigated and compared to an unfilled PDMS to evaluate any changes in overall crosslinking density. From Fig. 30c, it can be seen that all of the composites have a higher degree of swelling than that of unfilled PDMS reference even through these enhancements are within 10% of this reference value, indicating a slight reduction of the overall crosslinking densities of membranes upon the introduction of Ag nanoparticles, which is consistent with the FFV measurements.

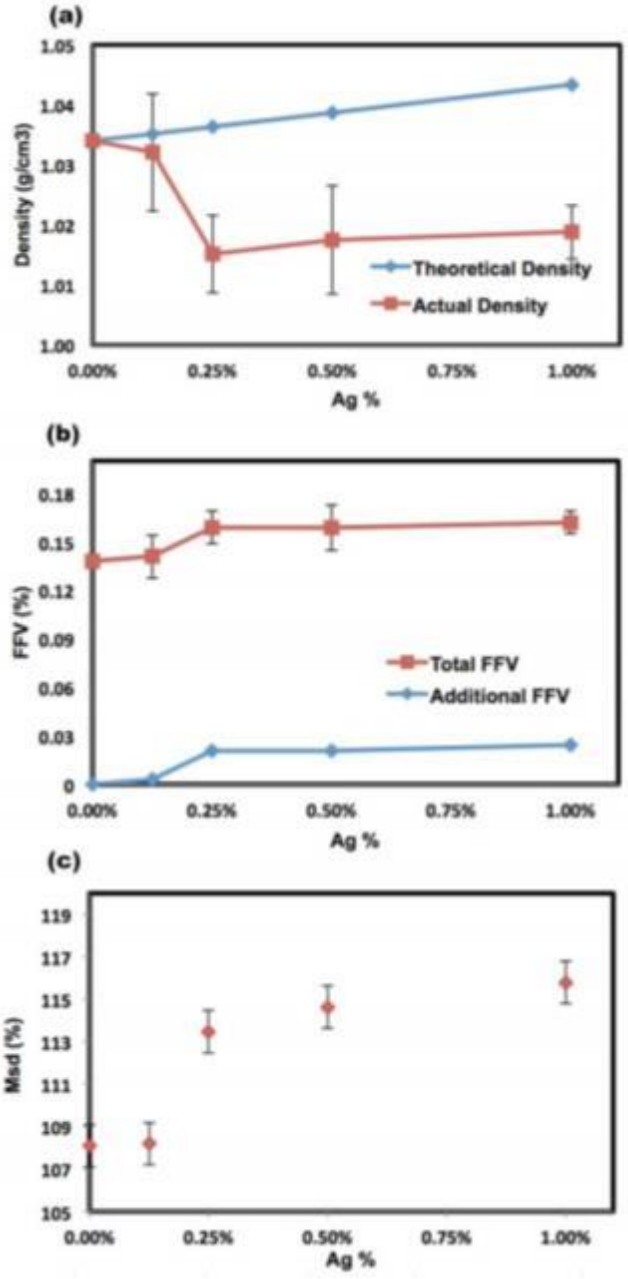

Figure 30. The effect of Ag nanoparticles concentration on (a) the density and (b) the FFV of Ag-PDMS nanocomposite membranes. (c) Swelling extent for nanocomposite membranes made of different concentrations of Ag nanoparticles.

Single gas tests using CPVV apparatus were carried out in order to reveal the effects of Ag nanoparticles in the nanocomposite membranes on pure CH_4 and CO_2 gas permeation properties. The permeability measurements of the PDMS and Ag-PDMS nanocomposite membranes are presented in Table 4.

As observed in Table 4, the variations of CH_4 gas permeability through the nanocomposite membranes and unfilled PDMS are within the measurement error (± 5%) which indicates that Ag nanoparticles have little effect on CH_4 gas permeation. However, there is an obvious reduction in the permeability of CO_2 in comparison to unfilled PDMS, which reaches a minimum at 0.25% Ag, although there is a slight increase in FFV as the concentration of Ag increases within the PDMS matrix (Fig. 30). CO_2 permeation changes could partly ascribed to the nanocomposite tortuosity, which increases the diffusion path length for gas

molecules after adding the Ag nanoparticles. Nevertheless, a similar effect on the permeation reduction was not observed for CH_4gas, suggesting tortuosity may not be the dominant effect in this case. Another possibility could be the interaction between the adsorbed CO_2 and O_2 on the surface of Ag nanoparticles, for which the Ag nanoparticles act as the catalyst. However, as the CO_2 permeation measurements are conducted in the environment in the absence of O_2, such a catalytic reaction could be inefficient. Alternatively, it is possible that Ag nanoparticles form reversible π-complexation with CO_2 gas molecules, which may contribute to the decrease of its permeability.

Table 4. The permeability (Barrer) of unfilled PDMS membrane and nanocomposite membranes

Penetrant	**PDMS**	**0.125%Ag**	**0.25%Ag**	**0.5%Ag**	**1%Ag**
CH_4	950	910	1000	950	920
CO_2	3130	2980	2330	2420	2600

The measurements for investigating the effect of Ag nanocomposite membranes on H_2S gas molecule removal was conducted with concentrations in the orders of tens of ppm. Such H_2S concentrations were chosen as they represent the magnitudes found in many real-life and industrial processes, some of which are presented in the introduction. The experiments were conducted with the setup explained in Fig. 1b with the system is exposed to 56 ppm H_2S gas in N_2 mixture.

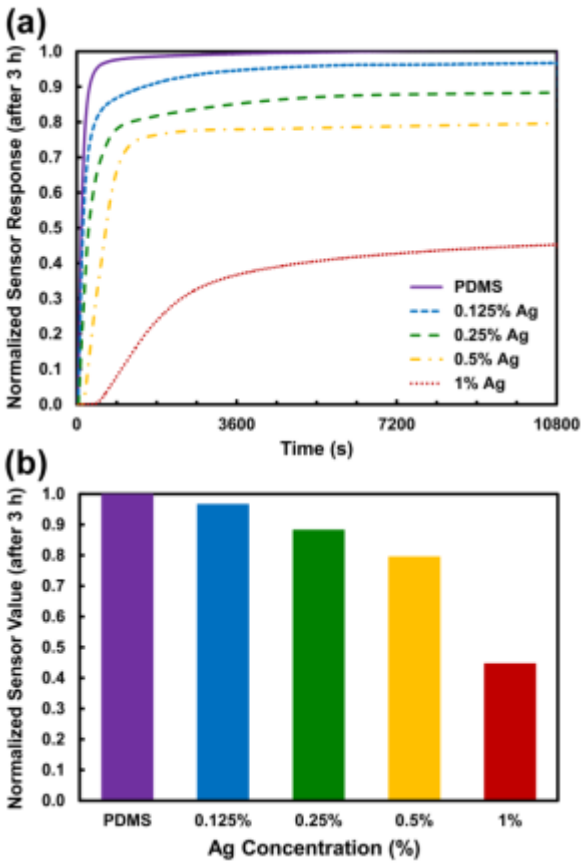

Figure31. (a) Normalized H_2S sensor dynamic responses after 3 h tests for composite membranes of different Ag concentrations; (b) Normalized values for the same responses after 3 h.

While the concentration of Ag nanoparticles within the Ag/PDMS composite membranes does not affect the permeation of CH_4 and moderately decreased the permeation of CO_2 gas molecules, it is found that there is a more significant effect on the H_2S gas. The dynamic responses of the H_2S sensor are shown in Fig. 31a and the normalized values for the same responses after 3 h are presented in Fig. 31b for comparison. The dynamic response can be divided into three phases, indicating the change in H_2S permeation kinetics through the composite membranes at different stages. The first phase is represented by the initial delay in the sensor response curve reflects the membranes solubility of H_2S gas molecules. For the unfilled PDMS membrane, the initial delay time is less than 10 s, indicating the intrinsic H_2S solubility of the membrane. As the concentration of Ag nanoparticles increased, this initial delay time was prolonged and eventually reach more than 400 s when the concentration of Ag reaching 1% (Fig. 32a), suggesting an increase in the H_2S solubility of membranes upon the addition of Ag nanoparticles. This phenomenon can be ascribed to the enhancement of available adsorption sites of Ag nanoparticles for H_2S gas molecules, therefore allowing more H_2S gas molecules to be soluble in the membrane.

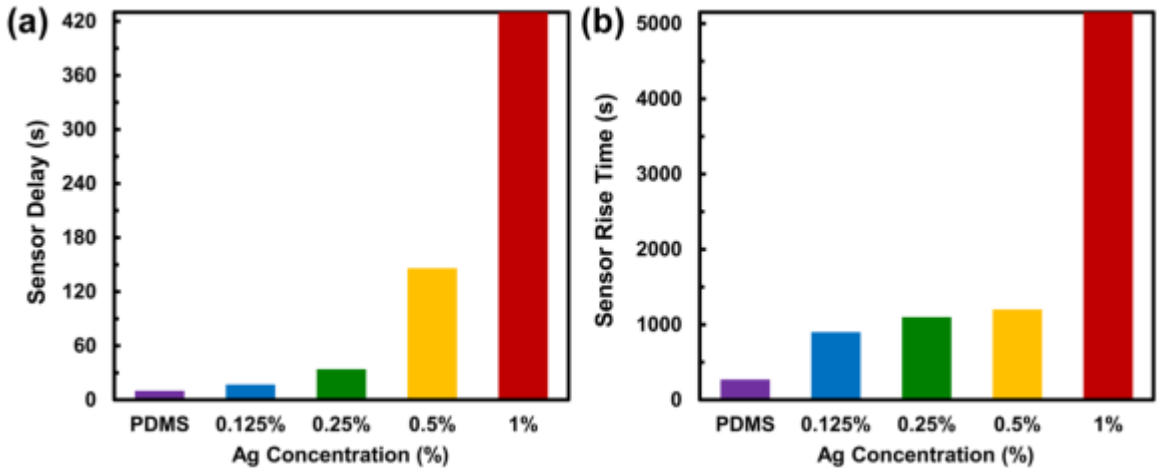

Figure 32. Sensor response (a) lags (b) rise times after the exposure to H_2S.

Interestingly for the membranes after the exposure of H_2S for a long time, this lead delay has dramatically decreased to ~100 s, revealing that a non-reversible reaction has occurred during the first exposure (Fig. 33a). Upon the adsorption of H_2S gas molecules onto surface of Ag nanoparticles, exposed parts of Ag nanoparticles undergo a chemical reaction transforming into very small amount of Ag_2S (evidence is presented in a later section).The Ag_2S acts as a protective material and prevents H_2S gas to further interact with Ag, resulting in the formation of a stable nanocompound made of Ag and Ag_2S (demonstrated as Ag/Ag_2S). The proposed interaction phase is illustrated in Fig. 34.

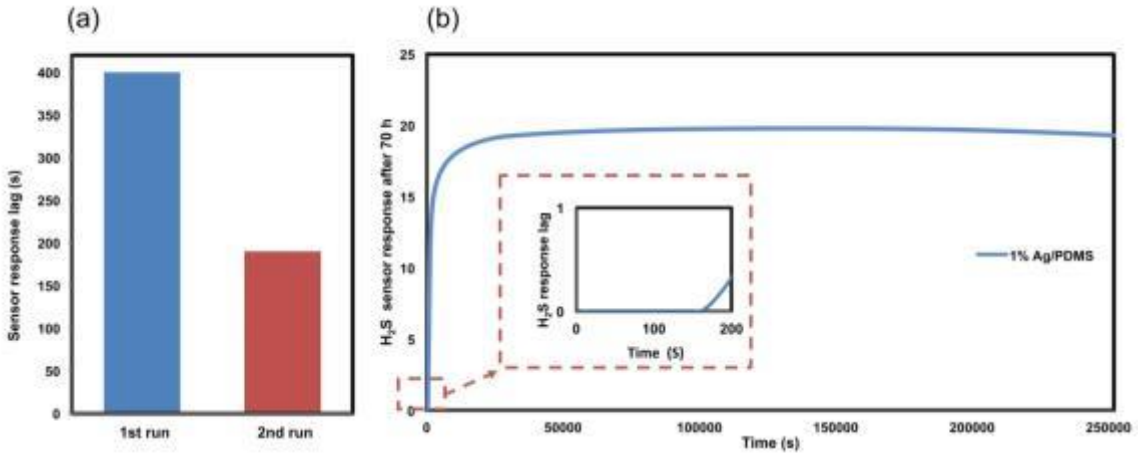

Figure 33. H_2S dynamic responses of the 1% Ag-PDMS membrane: (a) Comparison of the sensor lag time between the first and second runs; (b) After 70 h H_2S exposure test. The inset is the zoom-in figure of the H_2S sensor response curve for the first 200 s, indicating the sensor lag time during the second run of H_2S gas exposure.

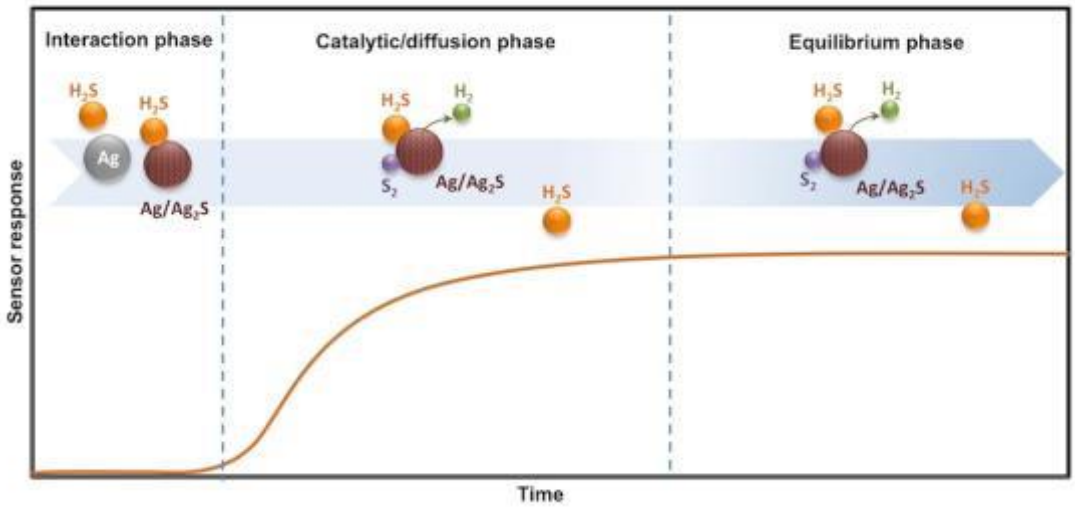

Figure34. Illustration of the proposed sensor response phases after the exposure to H_2S gas molecules.

After the delay phase, the H_2S sensor starts to show a near typical first order response. This second phase represents the competition between the diffusion of H_2S gas molecules through the composite membranes, and the catalytic decomposition of H_2S. In the presence of an internal potential in the interface of Ag/Ag_2S (the potential across the Schottky barrier), it is suggested a small amount of Ag^+ ions (or Ag atoms) are diffused to the surface of Ag_2S, catalyzing the decomposition of surface adsorbed H_2S molecules. In particular, the adsorbed H_2S molecules are first dissociated into H^+ and SH^- ions. Then the SH^- ions are further decomposed into H^+ and S^{2-} ions, which will eventually form H_2 gas molecules and adsorbed sulfur atoms. As a result, the increase of the nanoparticles (*i.e.* Ag/Ag_2S catalytic nanocompound) concentration enhances the catalytic decomposition effect of H_2S gas molecules, requiring longer time to reach the equilibrium state. This can be evident by Fig. 30b, in which the H_2S sensor against the unfilled PDMS membrane showed a relatively smaller time of 270 s to reach 90% of its saturation value when compared to the 5150 s for that of 1% Ag/PDMS composite membrane. It should

also be considered that the alteration of the gas molecule diffusivity by the nanocatalysts could play a significant role on slow permeation kinetics of H_2S gas molecules as a function of the concentration of nanocatalysts, where the diffusion path length for gas molecules is increased after the addition of nanocatalysts due to the induced tortuosity between base polymer and nanocatalysts.

In the third and final phase for the H_2S gas permeation kinetics, the response of H_2S gas sensor reached its saturation values (Figs. 31a and 32b). As can be seen, the composite membrane with 0.125% Ag only removes a small portion of H_2S gas molecules, allowing 95% of the gas to permeate in reference to the unfilled PDMS membrane. The increase of Ag nanoparticle concentration in the composite membrane results in a further reduction in the amount of permeated H_2S and it finally catalytically decomposes more than 60% of H_2S gas molecules when the Ag concentration reaches 1% even after the continuous H_2S gas exposure for more than 70 h (Fig. 33b).

A series of characterizations using XRD, XPS, FTIR, Raman spectroscopy and TEM-EDS analysis were conducted to confirm the assumption of the Ag/Ag_2S catalytic nanocompound formation in the composite membranes and the reaction stages that were presented in Fig. 34. XRD and XPS were not shown for the Ag/PDMS composite membranes as no Ag signal could be detected due to very low concentrations of the nanoparticles. Instead Ag nanoparticles were directly exposed to H_2S in order to investigate the interactions taking place. The XRD patterns, shown in Fig. 35a, represent the pristine Ag nanoparticles before and after the exposure to H_2S gas for 24 h. The pristine Ag is found to have a mixed cubic (FCC) and hexagonal (Silver-4H) structure. After the H_2S gas exposure, the XRD pattern revealed that the FCC Ag is still dominant, with a small amount of acanthine Ag_2S (monoclinic Ag_2S). The crystal structure of the Ag_2S can also be identified as possibly argentite (BCC Ag_2S) due to the presence of the corresponding XRD features. The intensities of Ag_2S peaks are weak, demonstrating that even after 24 h of exposure the Ag_2S amount is still relatively small in comparison to the bulk of the Ag nanoparticles. The HRTEM imaging was also conducted on the 24 h exposed samples. However, the SAED patterns of the nanoparticles after H_2S exposure were inconclusive in proving the existence of Ag_2S (Fig. 36)

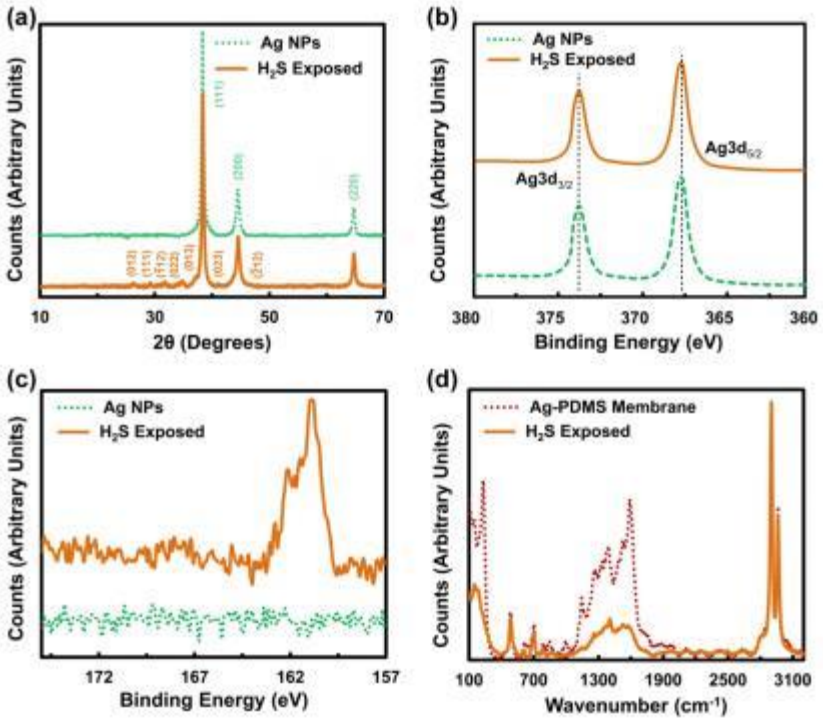

Figure35. (a) XRD for Ag nanoparticles before and after H_2S gas exposure. XPS analysis results: (b) Ag3d scan of pristine and H_2S gas exposed Ag nanoparticles; (c) S2p scan showing sculpture content on Ag nanoparticles before and after H_2S gas exposure. (d) Micro-Raman spectra for Ag/PDMS nanocomposite membrane before and after H_2S gas exposure.

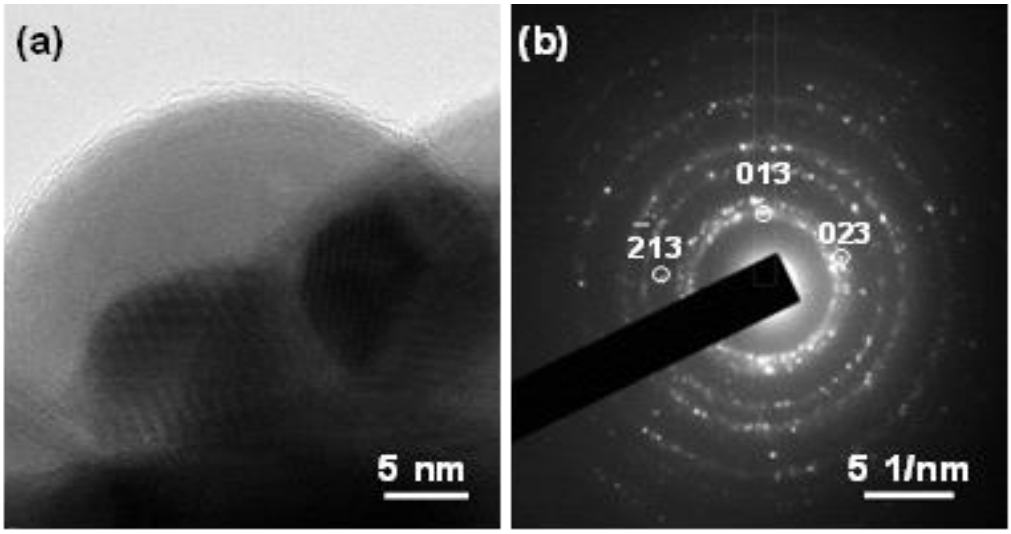

Figure36. (a) The HRTEM image of Ag nanoparticles after H_2S exposure. (b) The corresponding SAED pattern of Ag nanoparticles after H_2S exposure.

XPS studies shown in Figs. 35b and c, also provides a strong evidence to support the formation of an Ag/Ag_2S catalytic nanocompound as well as the presence of sulfur traces after the decomposition of H_2S. From Fig. 35b there is no obvious difference between the peaks binding energies of $Ag3d^{5/2}$ and $Ag3d^{3/2}$ before and after the H_2S gas exposure as the amount of Ag_2S is much smaller in comparison with the metallic Ag. However, a pronounced board peak with a binding energy of in the range of 160 to 164 eV appear after the exposure to H_2S, confirming the existence of the Ag_2S as well as adsorbed sulfur atoms.

While there was no distinguishing difference on the FTIR spectra of the Ag/PDMS composite membrane before and after the H_2S gas exposure (Fig. 37), Raman spectroscopy was able to be used for discerning the elemental change of the composite membranes under the influence of H_2S gas. This is due to the Ag nanoparticles surface enhanced Raman spectroscopy (SERS) effect that enhances the signals obtained. According to Fig. 28d, in addition to the typical PDMS peaks, a strong Ag lattice vibrational mode can be observed at 106 cm^{-1} for the Ag/PDMS composite membrane before any H_2S exposure. Furthermore, multi component peaks appear in the region between 1100 and 1600 cm^{-1}, which can be ascribed to the PVP dispersing agent of the Ag nanoparticles. In addition, the peak at 230 cm^{-1} can be assigned to the Ag-O stretching mode, suggesting that there is a small amount of Ag_2O inherently formed on the surface of Ag nanoparticles in the presence of an oxygenated environment. Interestingly, after the H_2S exposure, all aforementioned Raman peaks are weakened and a shoulder appears at 180 cm^{-1}, which can be assigned to Ag−S−Ag stretching mode. These changes confirm the formation of Ag_2S on the surface of Ag nanoparticles, which are embedded within the membranes. This also results in the reduction of the Ag SERS effect that is seen as the decrease of peaks in the 1100 to 1600 cm^{-1} region.

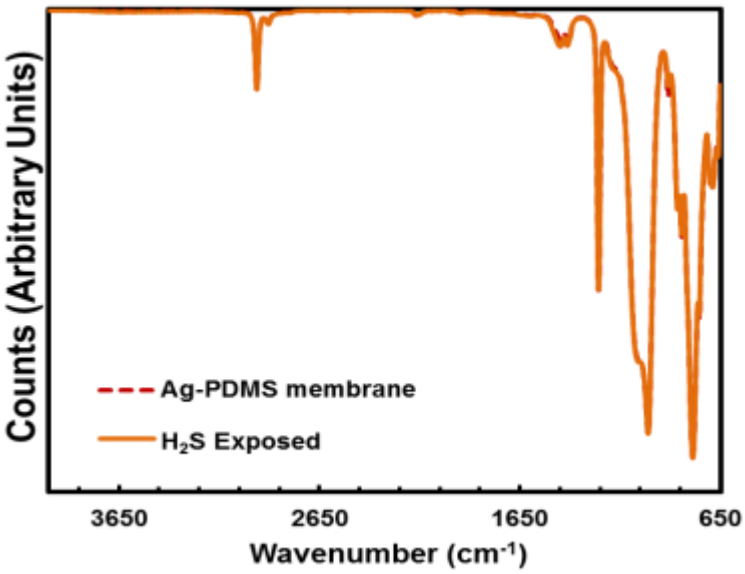

Figure 37. FTIR spectra for Ag-PDMS nanocomposite catalytic membranes before and after H_2S gas exposure.

Assessing the leaching of Ag^+ ions from the Ag-PDMS nanocomposite membranes can give an indication of their relative antimicrobial properties as they are known to be responsible for reducing microbial colonization. Fig. 38a shows the release of Ag^+ ions from the different nanocomposite materials. As can be seen, the 0.25 *wt*% Ag-PDMS releases the highest concentration of Ag^+ ions from the material and leaches approximately 60% more Ag^+ ions than the 1 *wt*% nanocomposite containing four times more Ag nanoparticles within the polymeric matrix. To understand the source of leaching difference, FFV within the polymeric matrices were assessed. A change in density (Fig. 38b) as a function of the Ag concentration in the nanocomposites was employed for evaluating the FFV within the polymer. As can be seen in Fig. 38b the 0.25 *wt*% Ag-PDMS has the lowest density. The lowest relative density and therefore highest relative FFV allowing for more efficient transportation of Ag^+ ions through the polymer matrix at this concentration.

It is known that for incorporated nanoparticles without any significant surface modification, a relatively high modification of FFV is an indication of better nanoparticle dispersion where the larger agglomeration of particles causes a lower surface to volume ratio resulting in fewer voids to be formed between the polymer chain and particle. The case is also applicable here that for Ag nanoparticle concentrations above 0.25 *wt*% agglomeration occurs. AFM analysis reveals larger particle agglomeration occurs with a shift in median surface artefact size from 200 nm for 0.25 *wt*% to over 600 nm for 1 *wt*%. More agglomeration means a less relaxed and homogenously porous polymeric matrix, inhibiting ionic release from the nanoparticle cores through the polymeric matrix and into the surrounding environment.

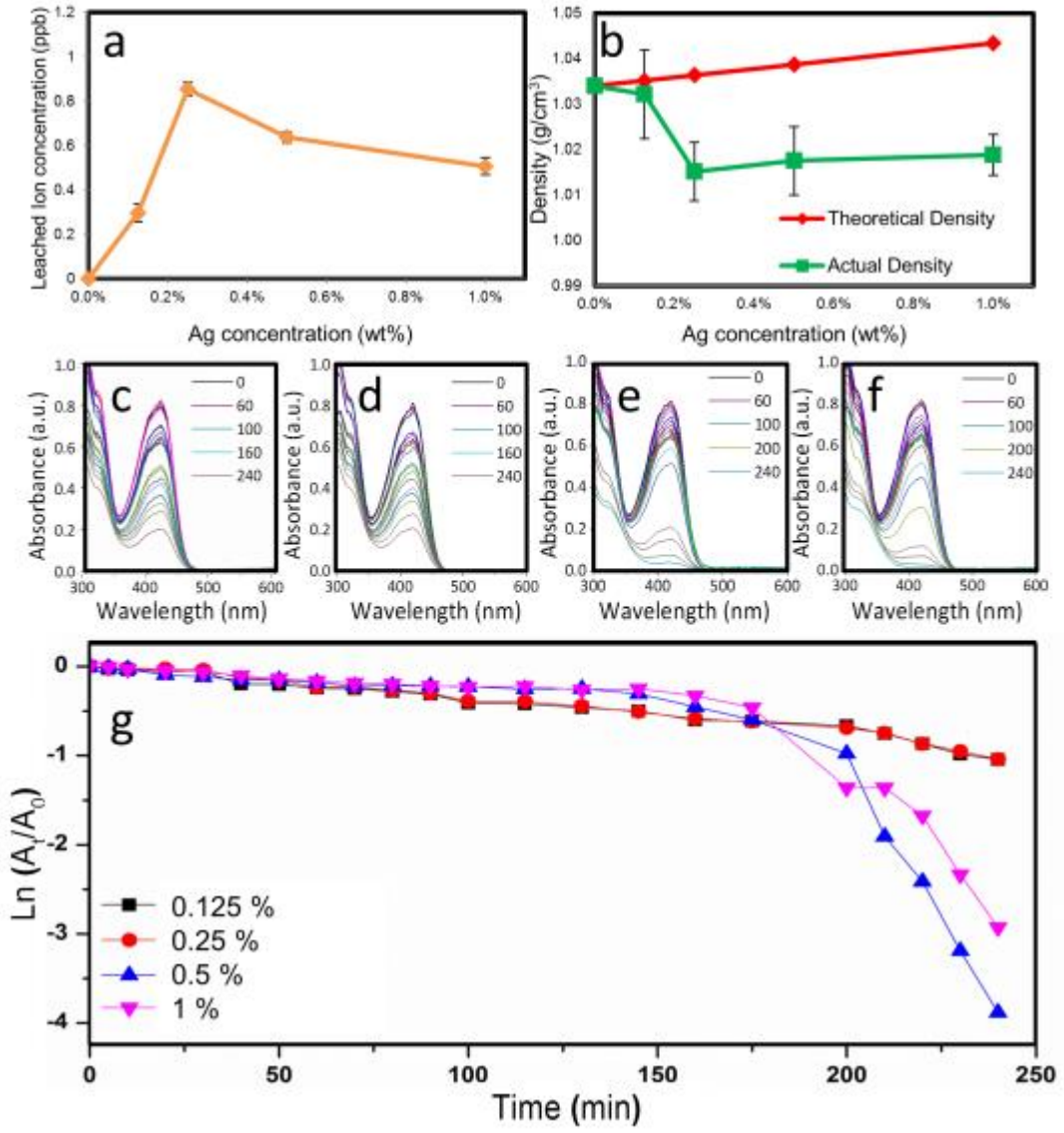

Figure 38.(a) Leached Ag^{+} ion concentration after one month and (b) change in density from different concentrations of Ag-PDMS nanocomposites.(c) Catalysis reaction data of 0.125 wt% Ag-PDMS. (d) Catalysis reaction data of 0.25 wt% Ag-PDMS. (e) Catalysis reaction data of 0.5 wt% Ag-PDMS (F) Catalysis reaction data of 1 wt% Ag-PDMS. (g) Catalysis reaction Ln plots showing rate kinetics in presence of different Ag-PDMS nanocomposites.

Evaluation of the catalytic activities of different concentrations of Ag loading within the polymer matrix highlights two separate time frames of interest (Figs. 38c-g). The first lies at the steady state value in the linear range between 60 and 160 min where 0.125 and 0.25 *wt*% Ag-PDMS shows the highest reaction rate, whereas after this time the 0.5 and 1 *wt*% show a sudden increase in reaction rate. This suggests that 0.125 and 0.25 *wt*% Ag-PDMS nanocomposite, more Ag nanoparticles are initially accessible to the reaction solution due to their uniform distribution within the matrix and the better porosity of the composite, allowing the reaction to occur at a steady rate. This steady rate is maintained over longer time periods, most likely due to a sustained Ag leaching profile. Conversely, in higher Ag-loaded nanocomposites reaction rates were initially lower than that in 0.25 *wt*% Ag-PDMS nanocomposite, followed by a notable sharp increase in catalytic activity after 160 min. This suggests that in 0.5 and 1 *wt*%, Ag nanoparticles are originally present as inaccessible clustered aggregates leading to lower activity initially, however once these clusters start to become more accessible they are able to react strongly to the penetrate. The

overall initial lower reaction rate of the 1 *wt*% Ag-PDMS compared to the 0.5 *wt*% Ag-PDMS further affirms the influence of nanoparticle clustering on reaction rates. The increased dispersion coupled with an increase in Ag^+ ion leaching from the 0.125 and 0.25 *wt*% Ag-PDMS causes this major difference in activity between them and the higher concentrations of Ag-PDMS nanocomposites.

3.2 In vitro microbial growth on the surface of nanocomposite membranes

Amongfour types of developed nanocomposite membranes, the excellent H_2S gas removal efficiency of Ag-PDMS membranes would favourably protect the sensors from the harsh rumen environment. More importantly, their outstanding CO_2 and CH_4 gas permeation properties were maintained after the addition of Ag nanofillers. Therefore, the following microbial studies would only focus on Ag-PDMS nanocomposite membranes.

In order to assess the antibacterial properties of the Ag-PDMS nanocomposites, as a combination of both catalytic and ion leaching activities, an in vitro bacterial growth test was carried out. This was done to evaluate cell adherence and viability on the surface of the nanocomposite materials. A fluorescence assay was utilized to quantify cell adherence and assess cell viability. As can be seen from both Fig. 39 and Table 4 the addition of Ag into the polymeric matrix reduced cell adherence to the surface of the material, with four to five times the number of cells found on the surface of the control PDMS compared to the surface of the nanocomposite. The well-known Ag bactericidal effect appears to have a substantial adverse effect on the viability of the cells that have attached to the surface, with the addition of Ag reducing the ratio of live to dead cells from 6.2 for the control PDMS to 1.1 for the 0.25 wt%. It is also interesting to note that the 0.25 wt% Ag-PDMS nanocomposite (Fig. 39b) shows a higher percentage of dead cells to live cells than the 1 wt% Ag-PDMS (Fig. 39c).

Table 4. Quantitative fluorescence study of the surface of the nanocomposites.

Material	Live cell surface area coverage (%)	Dead cell surface area coverage (%)	Live/dead cell count
PDMS	22.5 ± 2.1	1 ± 0.6	6.2
0.25 *wt*%	2.1 ± 0.2	3.2 ± 0.3	1.1
1 *wt*%	2.4 ± 0.1	2.3 ± 0.2	1.8

UV-Vis was performed on the media used in the growth tests to understand any inhibiting factors for proliferation and growth within the medium surrounding the material (Fig. 39d). The addition of Ag in the nanocomposites has reduced the overall growth of E. coli from the surrounding medium by approximately 60% for the 0.25 wt%, implying that the inhibiting effect of Ag not only influences those in direct contact with the surface of the material but all cells within close proximity. We see that at 0.125 wt% the surrounding media in the in vitro tests shows no difference in growth rate to the control stock containing no material. This indicates that the minimal inhibition concentration must lie in the range of 0.125 to 0.25 wt% for the composite.

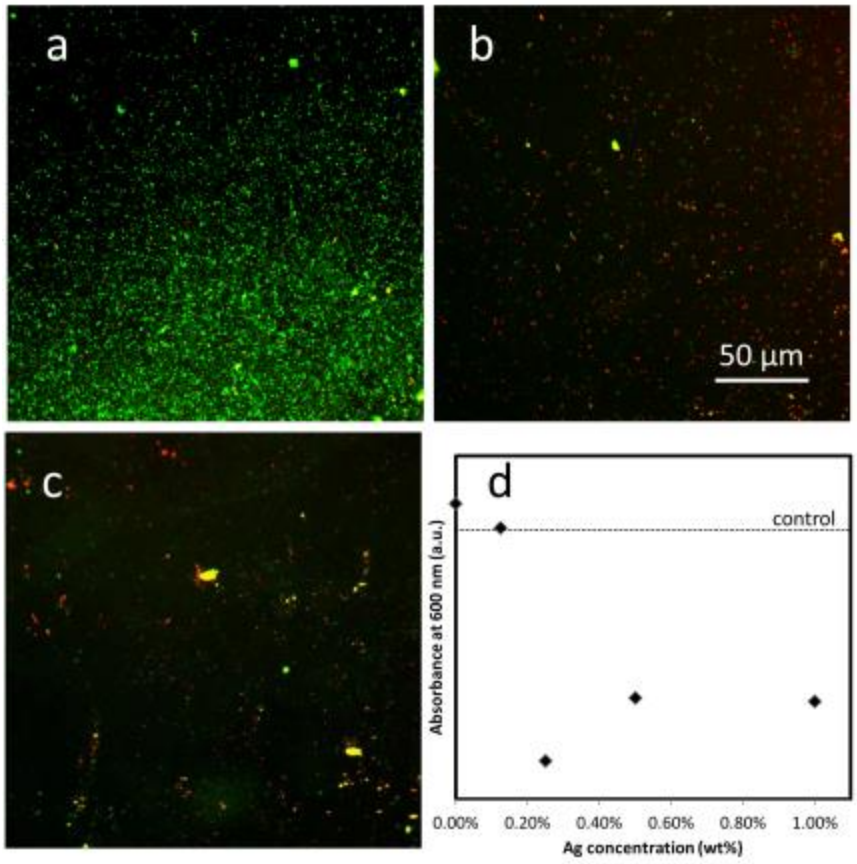

Figure 39. Fluorescent images of bacterial surface growth with live cells (green) and dead cells (red) on the surface of: (a) PDMS; (b) 0.25 wt% Ag-PDMS; (c) 1 wt% Ag-PDMS. (d) UV-Vis absorbance measurements of E. coli growth in broth containing the different concentration of Ag-PDMS nanocomposites.

3.3 In vivo microbial growth and diversity investigation on the surface of nanocomposite membranes

The effects of different wt% concentrations of Ag nanoparticle impregnation on the microbial communities growing on the surface of the intra-ruminal materials were assessed over 28 days with a SEM study and denaturing gradient gel electrophoresis (DGGE) analysis. The SEM images shown in Fig. 40 were taken to evaluate the relative surface coverage as well as colony morphology for the different wt% concentrations of Ag impregnation. The images shown are representative of the average coverage seen in the many images taken. Any Ag nanoparticle impregnation has visually reduced the surface coverage and the size of the microbial colonies, with the images of the control PDMS showing much larger colonies than the others. The images suggest an inhibition of the microbial growth rate and therefor the size of colonies that were formed. Total surface coverage is achieved by the microbial growth on the reference PDMS after 21 days (Fig. 40g). When comparing surface coverage and colony size of microorganisms on membranes with Ag nanoparticles, a substantial difference can be seen between the two concentrations shown. The 0.25 wt% Ag-PDMS shows far less microbial surface coverage than the material that contains four times more Ag implying an optimal loading of Ag in the PDMS matrix that allows for the maximum antimicrobial effect.

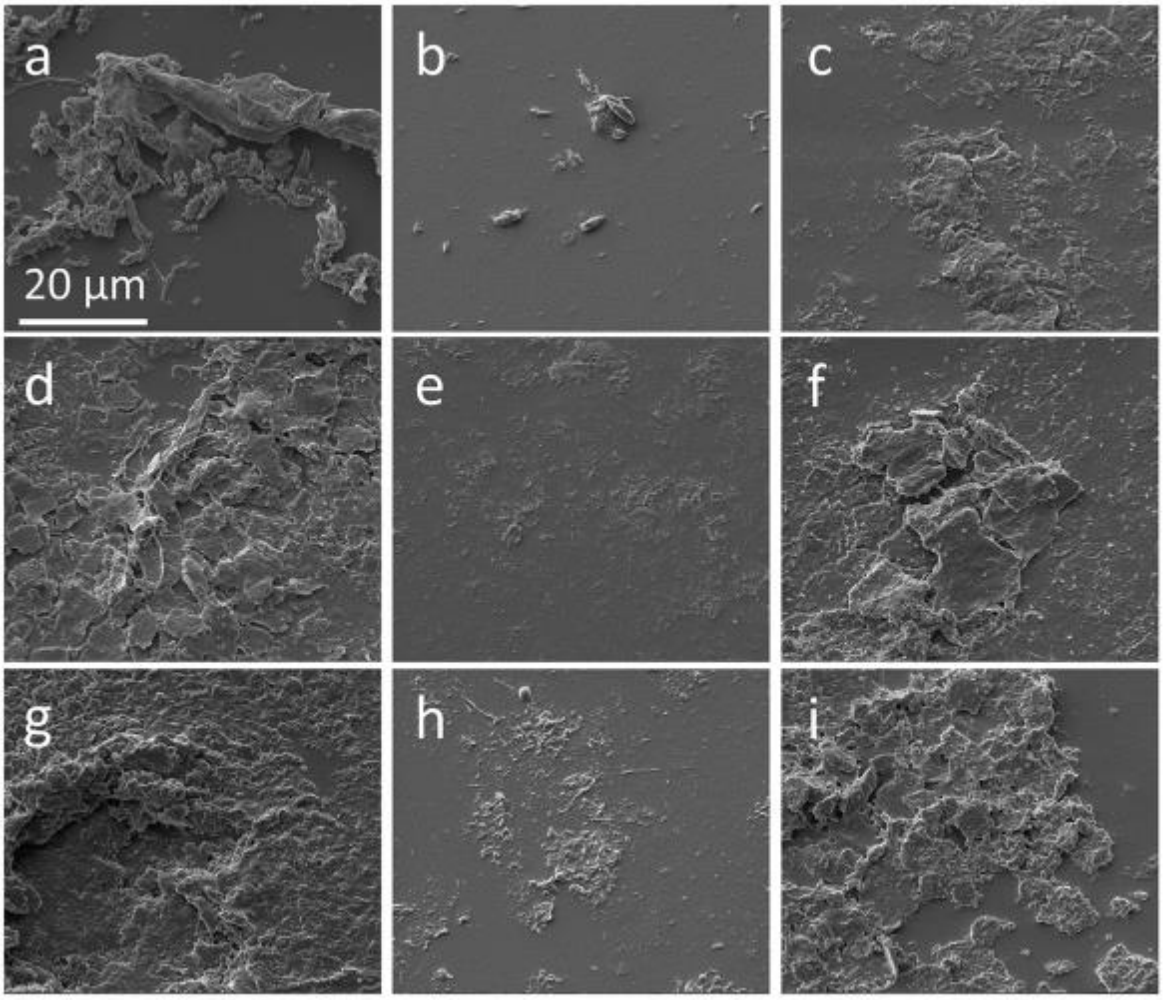

Figure 40.SEM images of microbial surface growth from in vivo study: (a) PDMS at 4 days; (b) 0.25 wt% Ag-PDMS at 4 days; (c) 1 wt% Ag-PDMS at 4 days; (d) PDMS at 14 days; (e) 0.25 wt% Ag-PDMS at 14 days; (f) 1 wt% Ag-PDMS at 14 days; (g) PDMS at 21 days; (h) 0.25 wt% Ag-PDMS at 21 days and (i) 1 wt% Ag-PDMS at 21 days

A cumulative DGGE gel was prepared and analysed to assess the overall effects on the bacterial community growing on these membranes. Fig. 41a suggests that the bacterial community growing on the membranes with 0.25 wt% Ag nanoparticles impregnation were more similar to one another (65-77% similarity) than the bacterial groups on the control PDMS without Ag nanoparticles (0%) or those with higher Ag nanoparticle concentration (~50% similarity). Day 7 to Day 28 bacterial communities on 0.25 wt% Ag nanoparticle impregnated nanocomposite also formed largely different clusters compared to the control PDMS and 1 wt% Ag-PDMS. Principal component analysis (PCA) of the data also validated this trend showing two distinct groups. Group 1 consisted of 0.25 wt% Ag nanoparticles samples while group 2 consists of all other samples (Fig. 41b)

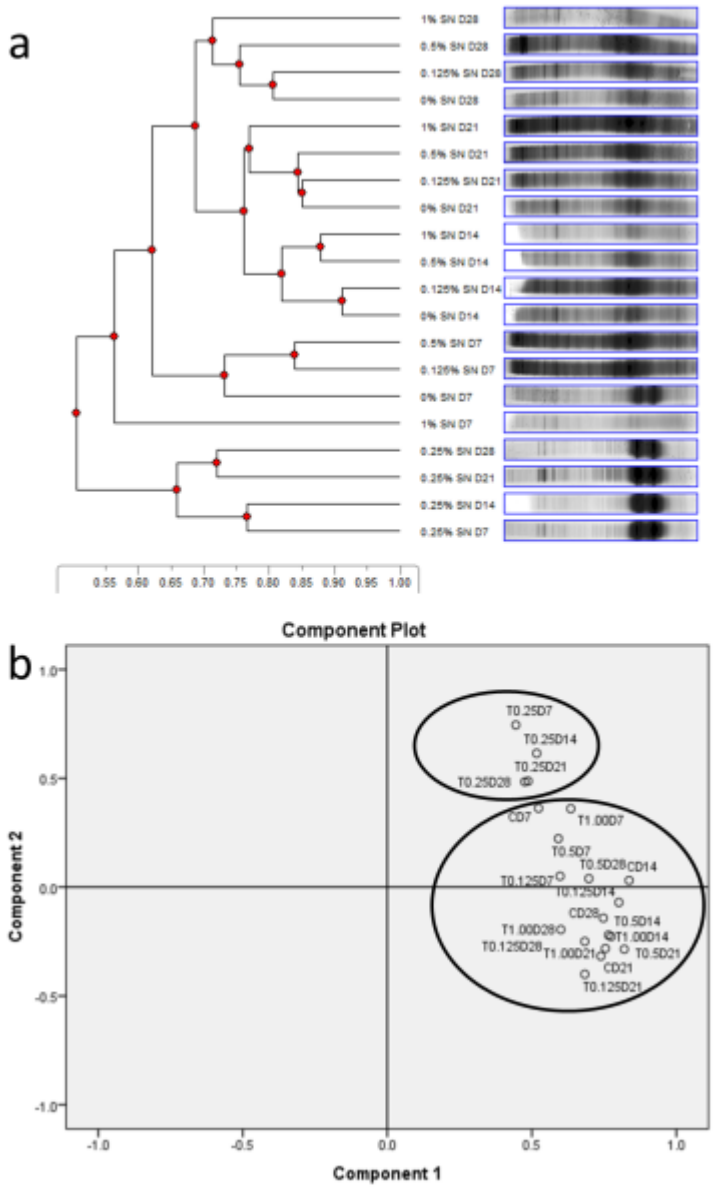

Figure 41. (a) UPGMA dendrogram derived from cumulative DGGE profiles of Ag nanoparticle impregnated PDMS membranes retrieved from the rumen of fistulated steer over 28 days. 0, 0.125, 0.25, 0.5 and 1 wt% refer to the level of Ag nanoparticle impregnation while D refers to day. Scale is indicative of similarity levels; (b) Principal component analysis of microbial communities on Ag nanoparticle impregnated PDMS membranes retrieved from the rumen of fistulated steer over 28 days. T0.125, T0.25, T0.50 and T1.00 refer to 0.125, 0.25, 0.50 and 1 wt% Ag nanoparticles impregnation respectively while D refers to day. C refers to controls of pristine PDMS.

The differences between PDMS membranes with 0 wt% and 0.25 wt% Ag nanoparticles were further investigated by using DGGE to compare the community profiles of these respective materials. The UPGMA dendrogram generated from these profiles showed that two distinct clusters were formed. These clusters were based on the presence or absence of Ag nanoparticles (Fig. 42a). The difference between the controls and nanocomposites with 0.25 wt% Ag nanoparticle impregnation was further validated with PCA plots (Fig. 42b) which also showed two distinct groups based on presence and absence of Ag nanoparticles. DGGE-based Shannon Weaver bacterial community diversity analysis indicated that the presence of 0.25 wt% Ag nanoparticles caused a reduction in bacterial diversity compared to the control

over 28 days (Table 5). At each time point, the bacterial community diversity (H′) in membranes with Ag nanoparticles was lower than the diversity on the control PDMS membranes. For example, on Day 7 and Day 28, the H′ for control samples (without Ag nanoparticles) were 3.05 and 3.01 compared to 2.43 and 2.70 for samples with 0.25 wt% of Ag nanoparticles (Table 5).

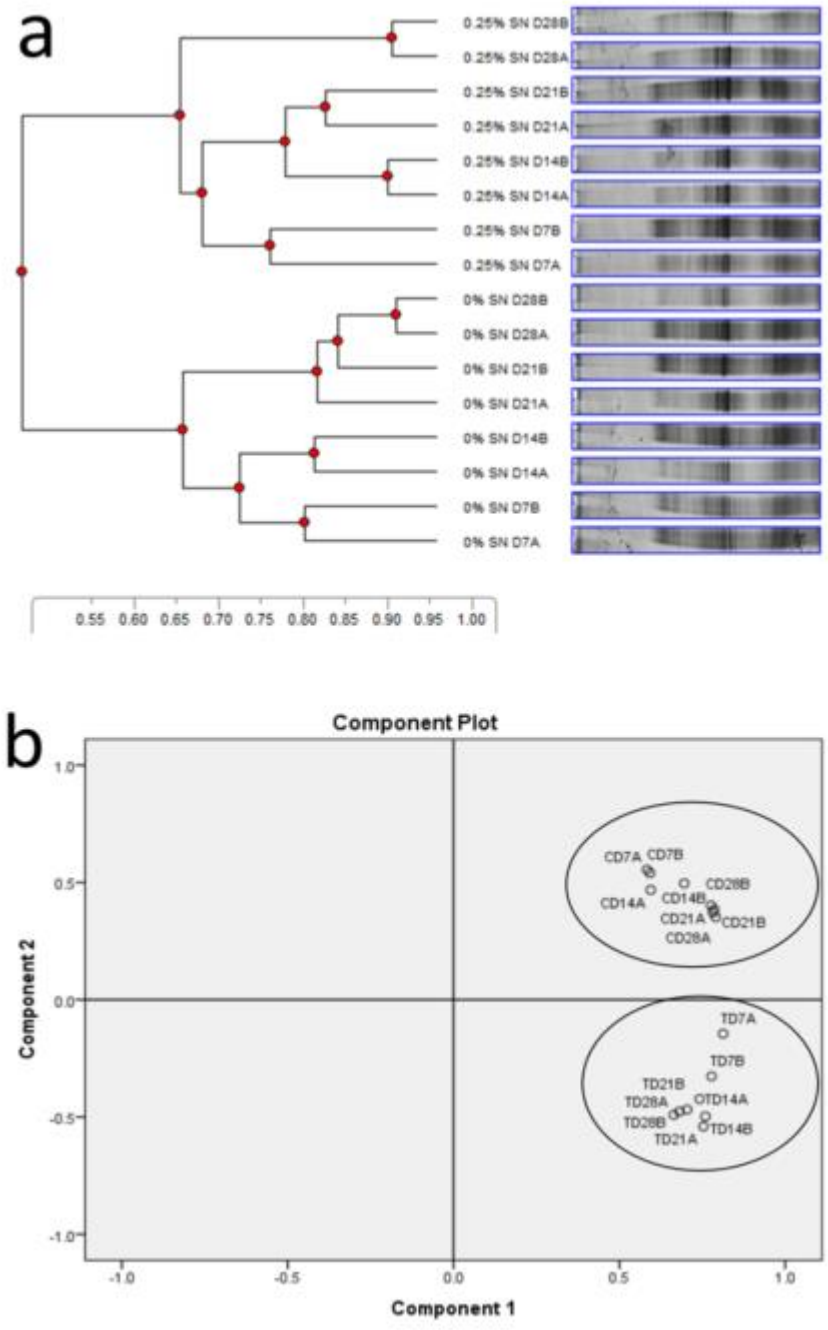

Figure 42. (a) UPGMA dendrogram derived from cumulative DGGE profiles of Ag nanoparticle impregnated PDMS membranes retrieved from the rumen of fistulated steer over 28 days. 0, and 0.25 *wt*% refer to the level of Ag nanoparticle impregnation while D refers to day. Scale is indicative of similarity levels; (b) Principal component analysis of microbial communities on Ag nanoparticle impregnated PDMS membranes retrieved from the rumen of fistulated steer over 28 days. T refers to 0.25 *wt*% Ag nanoparticles impregnation while D refers to day. C refers to controls of pristine PDMS.

Table 5. The effects of Ag concentration on bacterial community diversity on nanocomposite membranes placed in the rumen of a fistulated steer for up to 28 days.

Time (days)	0 *wt*% Ag (H′)	0.25 *wt*% Ag (H′)
0	0	0
7	3.05 ± 0.11	2.85 ± 0.10
14	2.90 ± 0.35	2.52 ± 0.13
21	2.92 ± 0.26	2.89 ± 0.18
28	3.01 ± 0.13	2.70 ± 0.07

The Ag-PDMS nanocomposite material has shown very interesting antibacterial properties with Ag nanoparticle loading within the PDMS matrix, appearing to have reduced the amount of bacteria that adheres to the surface by ten-fold (Fig. 39) and has decreased the diversity of bacteria growing on the material (Table 5). Interestingly, the 0.25 wt% Ag-PDMS nanocomposite showed the least surface coverage or fewest bacterial colonies. This can be ascribed to the maximum concentration of Ag^{+} ions leaching (Fig. 38a) from the nanocomposite which not only affects cells in contact with the surface but those within the surrounding media as well (Fig. 39d). The greatest performance at 0.25 wt% is due to an optimal loading of Ag nanoparticles where dispersion is at a maximum. Higher concentrations of Ag loading resulted in agglomeration of nanoparticles, reducing the number of active particles within the polymer matrix, which could interact with the outside environment. This effect of difference in nanoparticle dispersion with loading concentrations was also validated through the catalysis data (Fig. 38f).

Earlier work has focused on surface modification of antimicrobial materials by adding metallic silver coatings. However, *in vivo* studies of such coatings demonstrated limited success that was associated of low activity of the coatings in the release of silver ions due to rapid oxidation. More recently, it has been shown through *in vivo*studies of patients with ventilator-associated pneumonia that Ag-coated endotracheal tubes reduced the rate of mortality from 36 % to 14%. Catheters containing Ag were also found to significantly reduce the incidence of asymptomatic bacteriuria in hospitalized adults and may be more beneficial than antibiotic-coated catheters when used > 1 week. In another study, based on the guinea pig model ear, pressure equalization (PE) silicone tubes with and without impregnated Ag revealed that all the tubes except the Ag-loaded silicone tube demonstrated dense inflammatory film adhesion after 10 days.

This concentration of 0.25 *wt*% Ag-PDMS nanocomposite possesses an enhanced *in vivo* antimicrobial property which at low Ag concentrations is of potential interest to many medical, agricultural and purification technologies and applications. With such low concentrations of Ag impregnation showing efficient antimicrobial properties, these nanocomposites can have many benefits in regards to production costs and reducing any potential toxic effects from high quantities of Ag. Care must be taken when considering increasing the quantity of Ag within these materials for health and environmental risks associated with Ag toxicity.

3.4 Associate the micro-organisms to the gas constituents of the environment using the systems that incorporate the membranes

3.4.1. *Ex situ* measurements of gas produced from the rumen

Fig.43 shows the CH_4 and CO_2 gas concentrations produced by the rumen liquor for the period of over 60 hours. It is observed that it takes approximately 12 h for the rumen microflora to start producing CO_2 gas, which is an important food source for methanogens to be converted, together with the H_2 gas, into CH_4 gas. Interestingly, a significant level of CH_4 gas started to be observed at the 24 h incubation time, suggesting that the growth of methanogens in the liquor reaches a concentration that ample CH_4 gas was released.

In order to evaluate the effect of the defrosting time on the quality of the rumen liquor, CH_4 and CO_2 gas concentration measurements were performed for the rumen liquor samples deforested for 2 and 24 hours, respectively. From Fig. 44, it is seen that there is a delay of 2 and 4 hours for CO_2 and CH_4 gas productions, for the 2 and 24 h defrosted samples, respectively. This indicates the importance of the defrosting time on the gas production kinetics.

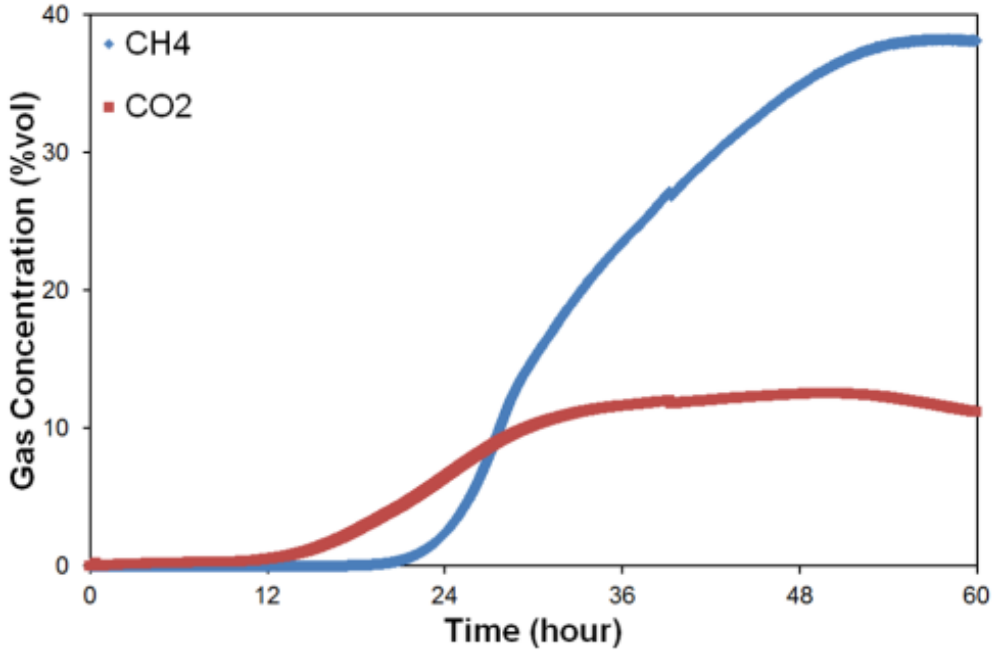

Figure 43. CH_4 and CO_2 gas concentrations produced by the rumen liquor samples in Menke buffer incubated at 40 ºC for the period of 60 h.

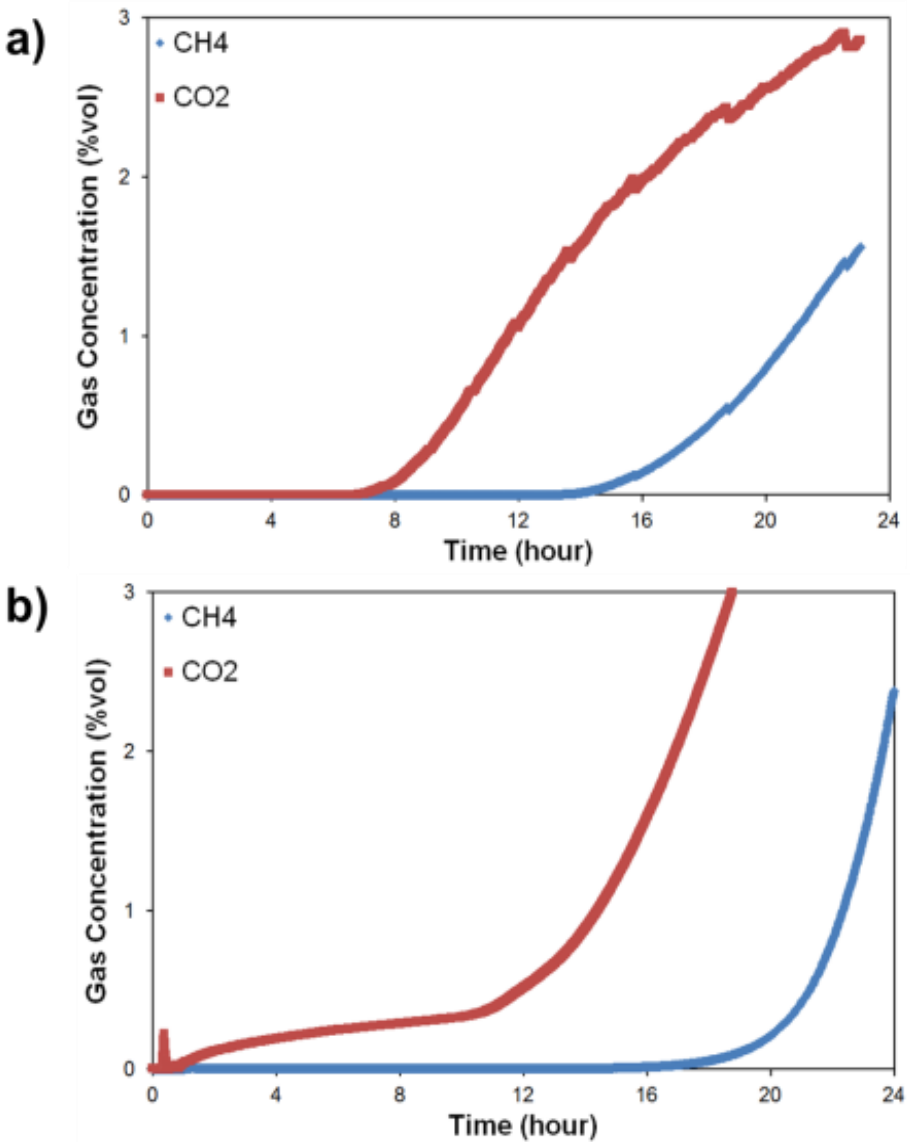

Figure 44. CH_4 and CO_2 gas concentration measurements produced by the rumen liquor samples defrosted for (a) 2 and (b) 24 h.

3.4.2. Associate the type of micro-organisms to the *ex situ* produced gas constituents

Microbial changes associated with the produced gas constituents are investigated over the 48 hour period of incubation under similar experimental conditions as in Section 5.4.1. Two microbial groups (bacteria and archaea (methanogens)) are targeted because of their roles in methane generation. Rumen bacteria are important because they are involved in the production of H_2 and CO_2 gas molecules in the rumen, being used by rumen methanogens for CH_4 production.

Community fingerprinting analyses showed substantial changes in the population of methanogens and total bacteria at 12 h of incubation (60% and 58% similarity between 0 and 12 h communities for methanogens and bacteria respectively) (Figs. 45 and 46). However, between 12 and 48 h there are minor changes in the microbial population suggesting that the microbial population is largely stable after 12 h (75% to 80% similarities). Analysis of the total population of methanogens shows an increase in their population from ~200,000 gene copies ml^{-1} at 0 h to 1554134 gene copies ml^{-1} by 48 h (Fig. 47). This is a six-fold increase in the population of methanogens over 48 h. This increase in number of methanogens can be associated with increased methane production after 24 h.

As CO_2 gas is a common fermentation by-product gas of different microbiota in the rumen, the correlation between types of micro-organisms and the CO_2 gas production cannot be extracted from this study. Identification of some of the bands detected on the community profile of rumen methanogens over 48 h showed that they largely belonged to the genus *Methanobrevibacter* sp, *M. ruminantium* and *Methanosarcina* sp. These groups are commonly found in bovine rumen and are believed to have a strong presence in our case for CH_4 production.

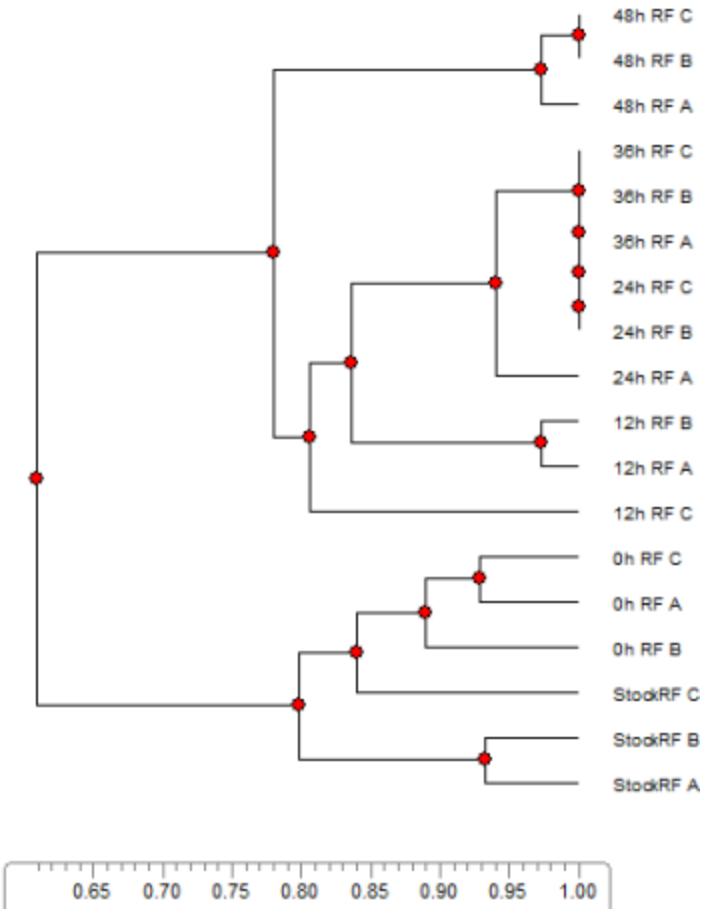

Figure 45. Community profiles of methanogens over a 48 h experimental period. StockRF refers to the original population in the rumen fluid. 0 h, 12 h, 24 h and 48 h RF refer to sampling periods in hours while letters A, B and C represent replicate samples.

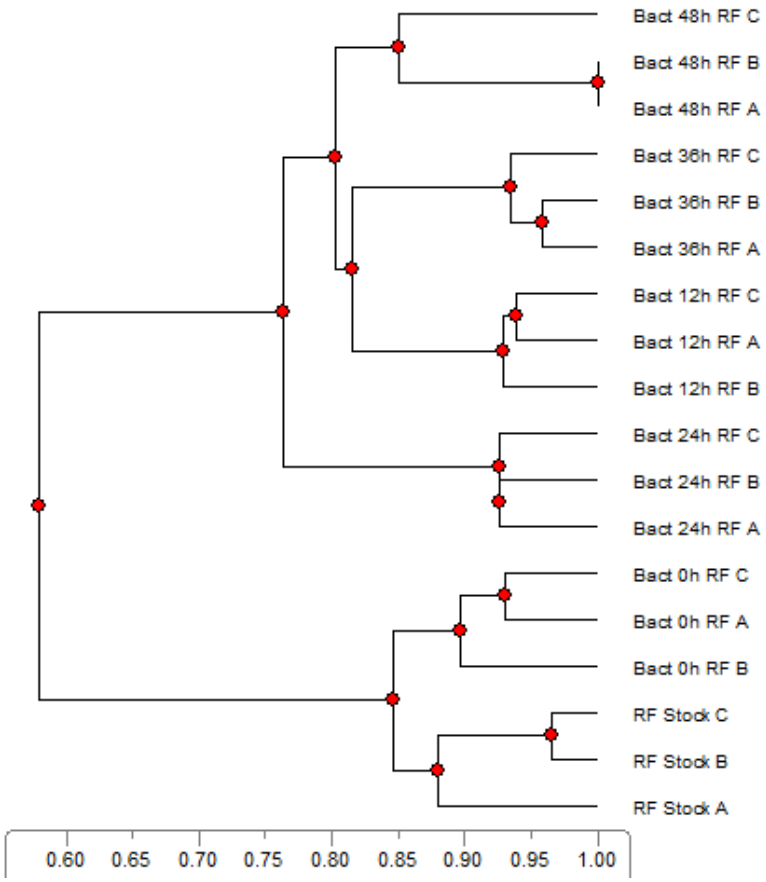

Figure 46. Community profiles of rumen bacteria over a 48 h experimental period. RF Stock refers to the original population in the rumen fluid. Batch 0 h, 12 h, 24 h and 48 h RF refer to sampling periods in hours while letters A, B and C represent replicate samples.

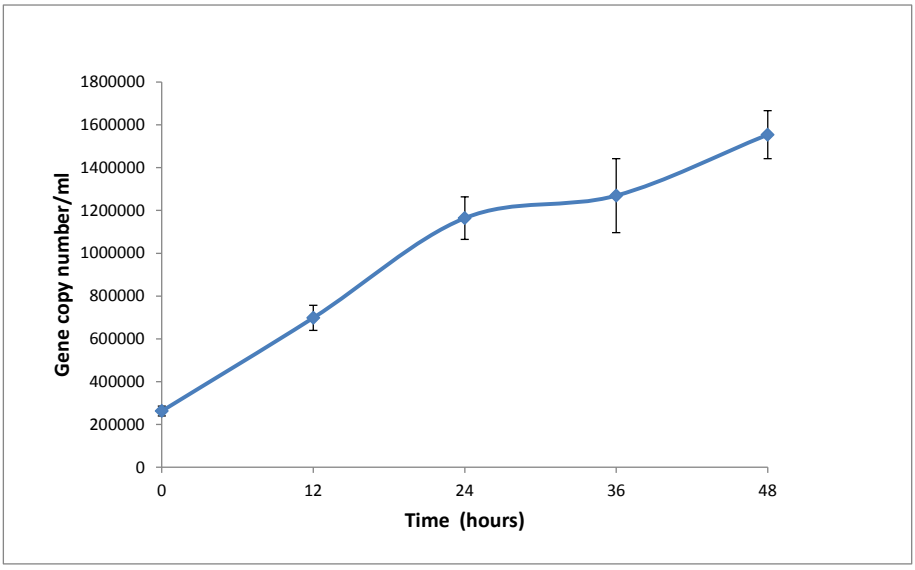

Figure 47. Quantitative PCR assay of population of methanogens over a 48 h experimental period. N (Sample number) =3.

The main members of methanogens include genus *Methanobrevibacter* sp, *M. ruminantium* and *Methanosarcina* sp. By comparing with Figure 43 at the similar time scale, the number of methanogens has a proportional relationship to the produced CH_4 gas concentration.

3.4.3. *In situ* measurements of gas produced from the rumen

The in situ measurements of gas produced from the rumen were carried out by placing gas capsules accommodating IR CH_4/CO_2 dual gas sensors in a fistulated cow. The membranes utilized here were 0.25%wt Ag/PDMS nanocomposite membranes with the same characteristics to those utilized during the *ex situ* gas measurements (Section 5.4.1). The assembly of the gas capsules and the detailed measurements were carried out by CSIRO colleagues in Armidale. The cow is fed once a day. The *in situ* CH_4 and CO_2 gas measurements for the period of 14 days (336 h) were obtained for several fistulated animals by Dr. Chris McSweeney and his group. The degradation of the sensor response after 10 days can be largely due to the drained battery. For the first 4 days (96 h), there are four complete CH_4 and CO_2 gas production cycles in which their production kinetics are very similar to those of *ex situ* gas measurements. Details and figures are presented in the associated project by Dr. Chris McSweeney and his group. The CO_2 gas is observed to be always produced first and then is utilized as the food source for methanogens to produce CH_4 gas.

3.4.4. Methanogens associated with CH_4 gas production in the rumen *(in situ)*

As demonstrated in Section 5.4.3, the produced CH_4 gas concentration had been associated to the number of methanogens (mainly genus *Methanobrevibacter* sp, *M. ruminantium* and *Methanosarcina* sp) for *ex situ* gas measurement of rumen liquor samples. Therefore in this section, only the identification of the specific types of methanogens during *in situ* gas measurements was carried out.

Methanogens were identified by Next Generation Sequencing (NGS) using MiSeq on illumina platform. DNA was extracted and purified from rumen samples. The 16S rRNA gene V4 variable region PCR primers Met86F and Met448R with barcode on the forward primer were used in a 30 cycle PCR using the HotStarTaq Plus Master Mix Kit (Qiagen, USA). After amplification, PCR products are checked in 2% agarose gel to determine the success of amplification and the relative intensity of bands. Multiple samples are pooled together (e.g., 100 samples) in equal proportions based on their molecular weight and DNA concentrations. Pooled samples are purified using calibrated Ampure XP beads. Then the pooled and purified PCR product is used to prepare DNA library by following Illumina TruSeq DNA library preparation protocol. Sequencing was performed at MR DNA (www.mrdnalab.com, Shallowater, TX, USA) on a MiSeq following the manufacturer's guidelines. Sequence data were processed using a proprietary analysis pipeline (MR DNA, Shallowater, TX, USA). In summary, sequences were depleted of barcodes then sequences <150bp removed, sequences with ambiguous base calls removed. Sequences were denoised, OTUs generated and chimeras removed. Operational taxonomic units (OTUs) were defined by clustering at 3% divergence (97% similarity). Final OTUs were taxonomically classified using BLASTn against a curated GreenGenes database (DeSantis et al 2006). Amplicons were used for NGS based analyses. According to Table 4, it is found that the methanogenic community associated with *in situ* CH_4 gas production are dominated by methanogens putatively identified as *Methanobrevibacter* spp followed by *Methanomicrobium* spp.

Table 6. Methanogenic species identification in percentage during *in situ* gas measurements

methanosarcina spp.	0.0043448
methanobrevibacter spp.	83.943054
methanimicrococcus spp.	0.043448
methanobrevibacter gottschalkii	0.0695169
methanomicrobium spp.	14.84909
methanosphaera spp.	0.7139961
methanobacteriaceae spp.	0.3765496

4. Discussion

This project achieved all its milestones in producing nanostructured membranes and assessing them. It was demonstrated that incorporating nanomaterials allowed the permeation tuning for different gas species while keeping the surface of membranes clean for a long time. This helped in establishing both *in vivo* and *in vitro* gas sensing systems for more accurate performance and longer lifetime.

The outcomes of this project are significance for the Australian agriculture and farming industries as measuring farming gas species are instrumental in assessing the productivity and greenhouse emission, which help in finding solutions to meet the industry obligations and the policies governing the industries.

The key findings of the project and the implications and limitations of those findings are as presented as follows:

The outcomes of this project provide significant input for the development of the gas capsules that can be potentially use in farming sectors and also assessing human's state of health. We showed that the membranes can efficiently help in obtaining information regarding the concentrations of the fermentation gases inside the rumen or gastrointestinal tract. The information appears as the concentration of three important gas species for metabolic activities of the microorganisms of the rumen (or gastrointestinal tract, which includes H_2, CH_4 and CO_2. CH_4 is a potent enteric greenhouse gas and its measurement is a preclude to its mitigation.

The incorporation of nanomaterials into membranes were shown to be important due to the following aspects : (1) They can block selected harmful gas species such as H_2S that naturally reduce the lifetime of sensors by corroding their components; (2) They can tune the permeation of gas towards the desired gas species and hence more accurate sensing with the transducers can be obtained and (3) The anti-bacterial functionality of the nanomaterials can keep the surface of the membranes clean to allow the accurate and consistent passage of the gasses through the membranes for a longer period.

In capsules, by incorporating membranes, the more accurate operation provide correct profiles of gas concentrations and CH_4/CO_2 or H_2/CH_4 ratios which are used for farming productivity assessments (gas production, production efficiency, greenhouse gas information and animals' state of health). While directly the gas production could not be measured it could be estimated through algorithms that provide the relation between the gas production and the relative pressure and size of the animals. The membranes were able to directly improve and impact the in vitro measurements.

We also presented a full investigation on the profile of the membranes both ex situ and in situ, in rumen liquid environment, and associated the type and number of microbial consortia to CH_4 production.

A patent was lodged based on the outcomes of this project and so far 6 journal papers were produced (three fully accepted and three under final stages of the review process).

5. Future research needs

More work should be done regarding the test of the capsules with their incorporated membranes. It is envisaged that the commercialisation path is facilitated through introducing the human capsules for human diagnostics and assessing the state of health. Exposure to a much larger human market will allow the rapid expansion of the capsule system and its future commercialisation. The capsules then at much lower costs can be fed back to the farming industries. The same can also be true for in vitro measurements, that can be tested for human medical investigations to become more widespread and then return to Agriculture sectors.

The human market will present an enormous opportunity and that can potentially attract many industrial partners to be involved in the commercialisation processes. At the moment, several overseas companies including Sunsclinic (China), Pharmbio (Korea) and Otsuka Pharmaceuticals (USA/Japan) have engaged with us for human trials and large scale device production. We intend to apply for a GrantReady fund to support the establishment of an Australian company that can partner with these overseas investors. The successful commercialisation of the gas measurement systems, with their incorporated nanocomposite membranes, will significantly reduce the individual unit cost and generate significant revenue, which will eventually be critical to large scale implementation of similar systems in Australian farms and the outcomes will be fed back into Australian agriculture research and industry divisions.

6. Publications

1. M. Nour, K. Berean, A. Chrimes, A. Sabirin Zoolfakar, K. Latham, C. McSweeney, M. R. Field, S. Sriram, K. Kalantar-zadeh and J. Z. Ou, “Silver nanoparticle/PDMS nanocomposite membranes for H_2S gas separation”, *Journal of Membrane Science*, 2014, 470, 346-355.

2. M. Nour, K. Berean, S. Balendhran, J. Z. Ou, J. Du Plessis, C. McSweeney, M. Bhaskaran, S. Sriram and K. Kalantar-zadeh, “CNT/PDMS composite membranes for H_2 and CH_4 gas separation”, *International Journal of Hydrogen Energy*, 2013, 38, 10494-10501.

3. J. Z. Ou, C. K. Yao, A. Rotbart, J. G. Muir, P. R. Gibson, K. Kalantar-zadeh, “Human intestinal gas measurement systems: in vitro fermentation and gas capsules”, *Trends in Biotechnology*, 2015, 33, 208-213.

4. K. Berean, J. Z. Ou, M. Nour, M. R. Field, M. Alsaif, Y. Wang, R. Ramanathan, V. Bansal, C. McSweeney, R. Kaner and K. Kalantar-zadeh, “Enhanced gas permeation of graphene nanocomposite membranes”, under review in *Journal of Physical Chemistry C* , 2015, pubs.acs.org/doi/abs/10.1021/acs.jpcc.5b02995

5. K. Berean, E. Adetutu, J. Z. Ou, M. Nour, E. Nguyen, D. Paull, J. Mcleod, R. Ramanathan, V. Bansal, K. Latham, G. Bishop-Hurley, C. McSweeney, A. Ball and K. Kalantar-zadeh, “A unique *in vivo* approach for investigating antimicrobial materials utilizing fistulated animals”, under review in *Scientific Reports* (ISI impact factor >5).

6. K. J. Berean, J. Z. Ou, T. Daeneke, B. Carey, E. Nguyen, Y. Wang, K. Kalantar-zadeh, “2D MoS_2 PDMS nanocomposites for NO_2 separation”, under review in *Small* (ISI impact factor >7).

7. APPENDICES

7.1 Suggestion for the correction of responses using the ruminant capsules

The intra-ruminal measurements constantly show the accumulative concentration of gas species (CH_4+CO_2) as over 100% which is practically impossible. CH_4 concentration showed a decrease when the feed was introduced. This is against the previous reports of any chamber measurements that always demonstrate an increase.

Three issues were identified. One was the calibration effect and the other two issues originated from the fact that the production value and concentration measured by sensors were two different entities. The difference affected the deciphering of the measured values in terms of pressure and volume effects:

1- Sensor calibration problems: A set of experiments were conducted to assess whether they not correctly calibrated for the condition when both gas species of CH_4 and CO_2 were present. The problem was identified as the calibration curve incorrectness. At 50% CH_4 and 50% CO_2 the system showed 115% concentration response. As such, the calibration curve needed an adjustment.

2- Pressure effect: in a constant volume chamber we increased both CO_2 and CH_4 production rate to simulate a feeding event. N2 gas was the ambient gas and we kept a steady production of N_2 to limit variables. We always kept the production rate of CO_2, 10 times that of CH_4 and increased the production of these two gas species stepwise. The sensor measurements showed decrease in the concentration of CH_4 present in the chamber. We present the following actual measurement to show the effect of 110% change in pressure. If consider simulating a cow's rumen volume as 100 L, after 4 hours it accommodates 110 L if we only take into consideration the pressure increase. In this case, CO_2 shows 20% increase from 40% to 60% which accounts for (40 L to 60% of 110L = 66 L) = 26 L increase. While CH_4 shows 10% decrease from 30% to 20% (30 L to 20% of 110L = 22 L) = 8 L decrease which is still a decrease in CH_4 magnitude. Although the CH_4 reduction effect has been ameliorated. This means that at least a third effect, in addition to sensor calibration effect and pressure, should play a role as well.

3- Effect of the released gas: average domestic cow rumen volume is approximately 185L and varies in the range of 150-200L. Normally the volume is divided to gas, new hay mostly dry and day before hay mostly wet. Average domestic sheep rumen volume is approximately 30L vary in the range of 20-40 L, with the same mechanism. It is suggested that the gas volume can be as small as 15% of the rumen just after the feed. An example is presented and simulated to show the effect. For a simulated cow rumen with 185 L rumen volume, we assumed that the gas volume, immediately after feeding, is no more than 15% (28 L) of the total volume. If we assume that non-gas materials are decreased by 12% during the digestion process (density of organic materials is approximated as 1 kg/L), then we can conclude the gas volume increased by 60% (i.e. from 28L to 45 L and assume a near linear increase). 11.2 L to 60% of 45 L at 110% pressure is 30 L = increase by 18.8 L, CH_4 shows 10% decrease from 30% to 20% 8.5 L to 20% of 45 L at 110% pressure = 10 L) = increase by 1.5 L. This is an increase in the concentration of both gas species. Considering a 10% increase in pressure. Altogether, CO_2 shows 20% increase. A minimum of 15% increase in the gas volume in 4 hours is needed to assure that the concentration of the CH_4 is increased by calculations within the volume of the rumen.

Considering the constant gas evacuation in the digestion process, the production is always positive. The above three effects were included in a computer written program that can be fed into intra-ruminal measurements.

7.2 The effect of oxygen on the recovery kinetics of the H_2 gas sensor

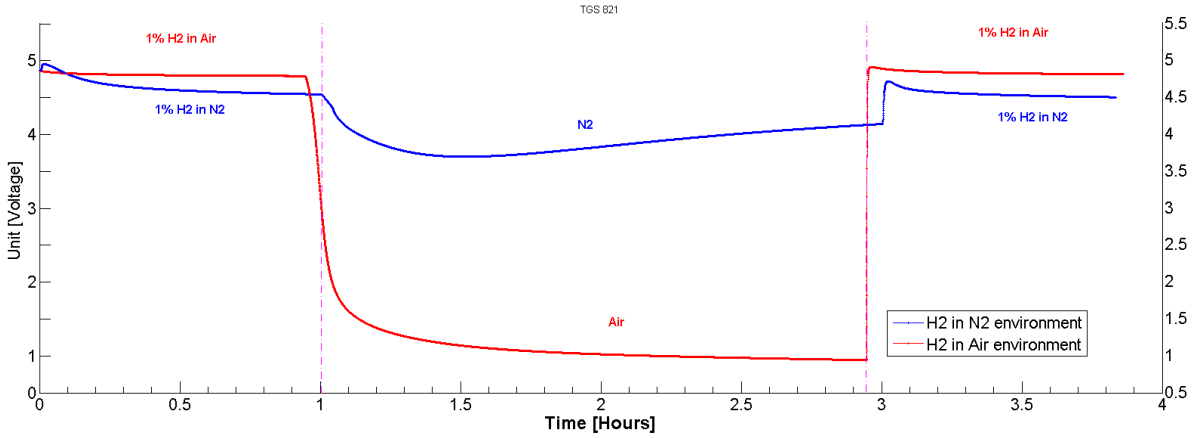

Figure A4. The difference of the recovery kinetics of the H_2 gas sensor in the presence of N_2 (Blue line) and air (Red line). The H_2 gas sensor response was not fully recovered in N_2 environment as the oxygen molecules were crucial in the recovery process.

8. Bibliography

1. Adamson, D.H.*, et al.* Functional graphene-rubber nanocomposites, EP2070093A1.

2. Afessa, B.*, et al.* (2010) Association between a silver-coated endotracheal tube and reduced mortality in patients with ventilator-associated pneumonia. *CHEST Journal* 137, 1015-1021.

3. Agarwal, R.*, et al.* (2006) Phonon dispersion in poly(dimethylsilane). *J. Organomet. Chem* 691, 2902-2908.

4. Ahmed, I.*, et al.* (2013) An investigation of fecal volatile organic metabolites in irritable bowel syndrome. *PLoS ONE* 8, e58204.

5. Ahn, J.*, et al.* (2008) Polysulfone/silica nanoparticle mixed-matrix membranes for gas separation. *J. Membr. Sci.* 314, 123-133.

6. Akhavan, O. (2010) The effect of heat treatment on formation of graphene thin films from graphene oxide nanosheets. *Carbon* 48, 509-519.

7. Anderson, M.R.*, et al.* (1991) Gas separation membranes: A novel application for conducting polymers. *Synthetic Met.* 41, 1151-1154.

8. Arasaradnam, R.P.*, et al.* (2014) Review article: Next generation diagnostic modalities in gastroenterology - Gas phase volatile compound biomarker detection. *Aliment. Pharmacol. Ther.* 39, 780-789.

9. Aroon, M.*, et al.* (2010) Performance studies of mixed matrix membranes for gas separation: A review. *Sep. Purif. Technol.* 75, 229-242.

10. Atayde, C. and and Doi, I. (2010) Highly stable hydrophilic surfaces of PDMS thin layer obtained by UV radiation and oxygen plasma treatments. *Phys Status Solidi C* 7, 189-192.

11. Bae, S.C.*, et al.* (2005) Chemical imaging in a surface forces apparatus: Confocal raman spectroscopy of confined poly(dimethylsiloxane). *Langmuir* 21, 5685-5688.

12. Baker, J. and Dudley, L. (1998) Biofouling in membrane systems—a review. *Desalination* 118, 81-89.

13. Banihashemi, F.*, et al.* (2011) CO_2 Separation Using PDMS/ZSM-5 Zeolite Composite Membrane. *Sep. Purif. Technol* 79, 293-302.

14. Barritault, P.*, et al.* (2013) Low power CO_2 NDIR sensing using a micro-bolometer detector and a micro-hotplate IR-source. *Sens Actuators B Chem.* 182, 565-570.

15. Basu, S.*, et al.* (2010) Membrane-based technologies for biogas separations *Chem. Soc. Rev.* 39, 750-768.

16. Beamson, G. and Briggs, D. (1992) *High resolution XPS of organic polymers : the Scienta ESCA300 database*. Wiley.

17. Beauchemin, K.A.*, et al.* (2008) Nutritional management for enteric methane abatement: a review. *Aust. J.Exp. Agr.* 48, 21-27.

18. Bechert, T.*, et al.* (2000) A new method for screening anti-infective biomaterials. *Nature Med.* 6, 1053-1056.

19. Berean, K.*, et al.* (2014) The effect of crosslinking temperature on the permeability of PDMS membranes: evidence of extraordinary CO_2 and CH_4 gas permeation. *Sep. Purif. Technol.* 122, 96-104.

20. Berger, T.*, et al.* (1976) Electrically generated silver ions: quantitative effects on bacterial and mammalian cells. *Antimicrob. Agents Chemother.* 9, 357.

21. Bernardo, P.*, et al.* (2009) Membrane gas separation: A review/state of the Art. *Ind. Eng. Chem. Res.* 48, 4638-4663.

22. Bhadra, M. and Mitra, S. (2013) Nanostructured membranes in analytical chemistry. *Trac-Trend. Anal. Chem* 45, 248-263.

23. Binks, B.P.*, et al.* (2012) Membrane permeation of testosterone from either solutions, particle dispersions, or particle-stabilized emulsions. *Langmuir* 28, 2510-2522.

24. Bjarnsholt, T.*, et al.* (2013) The *in vivo* biofilm. *Trends Microbiol.* 21, 466-474.

25. Blankenburg, S.*, et al.* (2010) Porous graphene as an atmospheric nanofilter. *Small* 6, 2266-2271.

26. Blume, I.*, et al.* (1991) Vapour sorption and permeation properties of poly (dimethylsiloxane) films. *J. Membr. Sci* 61, 85-97.

27. Bodas, D. and Khan-Malek, C. (2006) Formation of More Stable Hydrophilic Surfaces of PDMS by Plasma and Chemical Treatments. *Microelectron. Eng* 83, 1277-1279.

28. Bondarenko, O.*, et al.* (2013) Toxicity of Ag, CuO and ZnO nanoparticles to selected environmentally relevant test organisms and mammalian cells *in vitro*: a critical review. *Arch. Toxicol.* 87, 1181-1200.

29. Bondi, A. (1964) Van der Waals volumes and radii. *J. Phys. Chem-US* 68, 441-451.

30. Brosnahan, J.*, et al.* (2004) Types of urethral catheters for management of short‐term voiding problems in hospitalised adults. In *The Cochrane Library*.

31. Brown, G. (2012) The New Zealand Ruminant Methane Measurement Centre. Ag Research http://www.agresearch.co.nz/our-science/land-environment/greenhouse-gas/Pages/methane-measurement.aspx.

32. Bunch, J.S.*, et al.* (2008) Impermeable atomic membranes from graphene sheets. *Nano Lett.* 8, 2458-2462.

33. Buret, A.*, et al.* (1991) An *in vivo* model to study the pathobiology of infectious biofilms on biomaterial surfaces. *J. Biomed. Mater. Res.* 25, 865-874.

34. Canani, R.B.*, et al.* (2002) Nitric oxide production in rectal dialysate is a marker of disease activity and location in children with inflammatory bowel disease. *Am. J. Gastroenterol.* 97, 1574-1576.

35. Candau, S.*, et al.* (1982) *Structural, Elastic and Dynamic Properties of Swollen Polymer Networks*. Springer.

36. Carbonero, F.*, et al.* (2012) Contributions of the microbial hydrogen economy to colonic homeostasis. *Nat. Rev. Gastroenterol. Hepatol.* 9, 504-518.

37. Carey, B.J.*, et al.* (2015) Two solvent grinding sonication method for the synthesis of two-dimensional tungsten disulphide flakes. *Chem. Commun.* 51, 3770-3773.

38. Chambon, F. and Winter, H.H. (1987) Linear Viscoelasticity at the Gel Point of a Crosslinking PDMS with Imbalanced Stoichiometry. *J. Rheol* 31, 683-697.

39. Chan, S.-H.*, et al.* (1993) Cholesterol oxidation in whole milk powders as influenced by processing and packaging. *Food Chem.* 47, 321-328.

40. Chassé, W., *et al.* (2011) Cross-link density estimation of PDMS networks with precise consideration of networks defects. *Macromolecules* 45, 899-912.

41. Chen, J.-T., *et al.* (2013) Surface modification of poly(dimethylsiloxane) by atmospheric pressure high temperature plasma torch to prepare high-performance gas separation membranes. *J. Membr. Sci* 440, 1-8.

42. Chen, L., *et al.* (2002) Absorption of NO_2 in a packed tower with Na_2SO_3 aqueous solution. *Environ. Prog.* 21, 225-230.

43. Chen, X., *et al.* (1993) Effects of structure and annealing on the surface composition of Multiblock copolymers of bisphenol apolycarbonate and poly(dimethylsiloxane). *Macromolecules* 26, 4601-4605.

44. Cho, B., *et al.* (2015) Charge-transfer-based gas densing using stomic-layer MoS_2. *Sci. Rep.* 5, 8052.

45. Cho, I. and Blaser, M.J. (2012) The human microbiome: at the interface of health and disease. *Nat. Rev. Genet.* 13, 260-270.

46. Chrimes, A.F., *et al.* (2013) Microfluidics and Raman microscopy: current applications and future challenges. *Chem. Soc. Rev.* 42, 5880-5906.

47. Chung, T.-S., *et al.* (2007) Mixed matrix membranes (MMMs) comprising organic polymers with dispersed inorganic fillers for gas separation. *Prog. Polym. Sci.* 32, 483-507.

48. Clemente, Jose C., *et al.* (2012) The impact of the gut microbiota on human health: An integrative view. *Cell* 148, 1258-1270.

49. Coenye, T. and Nelis, H.J. (2010) *In vitro* and *in vivo* model systems to study microbial biofilm formation. *J. Microbiol. Methods* 83, 89-105.

50. Cong, H., *et al.* (2007) Brominated poly (2, 6-diphenyl-1, 4-phenylene oxide) and its silica nanocomposite membranes for gas separation. *Ind. Eng. Chem. Res.* 46, 2567-2575.

51. Cong, H. and Pan, T. (2008) Photopatternable conductive PDMS materials for microfabrication. *Adv. Funct. Mater.* 18, 1912-1921.

52. Costa, S., *et al.* (2008) Characterization of carbon nanotubes by Raman spectroscopy *Mater Sci-Poland* 26, 433-441.

53. Daima, H.K., *et al.* (2014) Synergistic influence of polyoxometalate surface corona towards enhancing the antibacterial performance of tyrosine-capped Ag nanoparticles. *Nanoscale* 6, 758-765.

54. Davoudi, Z.M., *et al.* (2014) Antibacterials: Hybrid Antibacterial Fabrics with Extremely High Aspect Ratio Ag/AgTCNQ Nanowires *Adv. Funct. Mater.* 24, 1030-1030.

55. De Greef, A., *et al.* (2009) Towards flexible medical instruments: Review of flexible fluidic actuators. *Precis. Eng.* 33, 311-321.

56. De Lacy Costello, B., *et al.* (2008) An analysis of volatiles in the headspace of the faeces of neonates. *J. Breath Res.* 2, 037023.

57. De Lacy Costello, B.P.J., *et al.* (2013) The importance of methane breath testing: A review. *J. Breath Res.* 7, 024001.

58. De Meij, T.G., *et al.* (2014) Electronic nose can discriminate colorectal carcinoma and advanced adenomas by fecal volatile biomarker analysis: Proof of principle study. *Int. J. Cancer* 134, 1132-1138.

59. de Menezes Atayde, C. and Doi, I. (2010) Highly stable hydrophilic surfaces of PDMS thin layer obtained by UV radiation and oxygen plasma treatments. *Phys. Status Solidi(c)* 7, 189-192.

60. Di Natale, C.*, et al.* (2014) Solid-state gas sensors for breath analysis: A review. *Anal. Chim. Acta* 824, 1-7.

61. Dixon, E.*, et al.* (2011) Solid-phase microextraction and the human fecal VOC metabolome. *PLoS ONE* 6, e18471.

62. Dollase, T.*, et al.* (2003) Effect of Interfaces on the Crystallization Behavior of PDMS. *Inter. Sci.*11, 199-209.

63. Dowling, D.*, et al.* (2001) Deposition of anti-bacterial silver coatings on polymeric substrates. *Thin Solid Films* 398, 602-606.

64. Dresselhaus, M.S.*, et al.* (2005) Raman spectroscopy of carbon nanotubes. *Phys Rep* 409, 47-99.

65. Dresselhaus, M.S.*, et al.* (2010) Perspectives on carbon nanotubes and graphene Raman spectroscopy. *Nano Lett.* 10, 751-758.

66. Du, H.*, et al.* (2011) Separation of hydrogen and nitrogen gases with porous graphene membrane. *J. Phys. Chem. C* 115, 23261-23266.

67. Dull, T.*, et al.* (2001) Determination of pore size in mesoporous thin films from the annihilation lifetime of positronium. *J. Phys. Chem. B* 105, 4657-4662.

68. Eklund, P.C.*, et al.* (1995) Vibrational modes of carbon nanotubes; Spectroscopy and theory. *Carbon* 33, 959-972.

69. Eldrup, M.*, et al.* (1981) The temperature dependence of positron lifetimes in solid pivalic acid. *Chem. Phys* 63, 51-58.

70. Elechiguerra, J.L.*, et al.* (2005) Interaction of silver nanoparticles with HIV-1. *J. Nanobiotechnol.* 3, 1-10.

71. Esteves, A.*, et al.* (2009) Influence of cross-linker concentration on the cross-linking of PDMS and the network structures formed. *Polymer* 50, 3955-3966.

72. F. Tuinstra, J.L.K. (1970) Raman spectrum of graphite. *J. Chem. Phys.* 53, 1126-1130.

73. Favre, E. (1996) Swelling of crosslinked polydimethylsiloxane networks by pure solvents: influence of temperature. *Eur. Polym. J.* 32, 1183-1188.

74. Ferrari, A.*, et al.* (2006) Raman spectrum of graphene and graphene layers. *Phys. Rev. Lett.* 97, 187401.

75. Finster, J.*, et al.* (1990) ESCA and SEXAFS investigations of insulating materials for ULSI microelectronics. *Vacuum* 41, 1586-1589.

76. Freeman, B.D. (1999) Basis of permeability/selectivity tradeoff relations in polymeric gas separation membranes. *Macromolecules* 32, 375-380.

77. Fu, Y.-J.*, et al.* (2010) Effect of UV-ozone treatment on poly(dimethylsiloxane) membranes: surface characterization and gas separation performance. *Langmuir* 26, 4392-4399.

78. Fujita, H. (1961) Diffusion in polymer-diluent systems. In *Fortschr. Hochpolym. Forsc*, pp. 1-47, Springer.

79. Furno, F.*, et al.* (2004) Silver nanoparticles and polymeric medical devices: a new approach to prevention of infection? *J. Antimicrob. Chemoth.* 54, 1019-1024.

80. Gabriel, M.M.*, et al.* (1995) Effects of silver on adherence of bacteria to urinary catheters: in vitro studies. *Curr. Microbiol.* 30, 17-22.

81. Garner, C.E.*, et al.* (2007) Volatile organic compounds from feces and their potential for diagnosis of gastrointestinal disease. *FASEB J.* 21, 1675-1688.

82. Ghadimi, A.*, et al.* (2010) Prediction of ternary gas permeation through synthesized PDMS membranes by using principal component analysis (PCA) and fuzzy logic (FL). *J Membrane Sci* 360, 509-521.

83. Ghule, K.*, et al.* (2006) Preparation and characterization of ZnO nanoparticles coated paper and its antibacterial activity study. *Green Chem.* 8, 1034-1041.

84. Gilbert, R.E. and Harden, M. (2008) Effectiveness of impregnated central venous catheters for catheter related blood stream infection: a systematic review. *Curr. Opin. Infect.Dis.* 21, 235-245.

85. Girshevitz, O.*, et al.* (2008) Solution-deposited amorphous titanium dioxide on silicone rubber: A conformal, crack-free antibacterial coating. *Chem. Mater.* 20, 1390-1396.

86. Girvan, M.S.*, et al.* (2003) Soil type is the primary determinant of the composition of the total and active bacterial communities in arable soils. *Appl. Environ. Microbiol.* 69, 1800-1809.

87. Gong, C. and Fréchet, J.M.J. (2000) End functionalization of hyperbranched poly(siloxysilane): novel crosslinking agents and hyperbranched–linear star block copolymers. *J. Polym. Sci. Pol. Chem* 38, 2970-2978.

88. Gong, X. and Wen, W. (2009) Polydimethylsiloxane-based conducting composites and their applications in microfluidic chip fabrication. *Biomicrofluidics* 3, 012007.

89. Government, A. (2012) AUSTRALIAN NATIONAL GREENHOUSE ACCOUNTS: Quarterly Update of Australia's National Greenhouse Gas Inventory. (June Quarter edn) (Efficiency, D.o.C.C.a.E., ed).

90. Goyal, A.*, et al.* (2009) *In situ* synthesis of metal nanoparticle embedded free standing multifunctional PDMS films. *Macromol. Rapid Comm.* 30, 1116-1122.

91. Gunatillake, P.A.*, et al.* (2003) Designing biostable polyurethane elastomers for biomedical implants. *Aust. J. Chem.* 56, 545-557.

92. Han, J.T.*, et al.* (2013) Dispersant-free conducting pastes for flexible and printed nanocarbon electrodes. *Nat. Commun.* 4, 2491.

93. Hankel, M.*, et al.* (2012) Asymmetrically decorated, doped porous graphene as an effective membrane for hydrogen isotope separation. *J. Phys. Chem. C* 116, 6672-6676.

94. Hao, J.*, et al.* (2002) Upgrading low-quality natural gas with H_2S and CO_2 selective polymer membranes Part I. Process design and economics of membrane stages without recycle streams. *J. Memb. Sci.* 209, 177-206.

95. He, Z.*, et al.* (2002) Nanostructured poly (4-methyl-2-pentyne)/silica hybrid membranes for gas separation. *Desalination* 146, 11-15.

96. Hodgkinson, J. and Tatam, R.P. (2013) Optical gas sensing: A review. *Meas. Sci. Technol.* 24, 012004.

97. Hong, M.*, et al.* (2004) Highly Selective H_2 Separation Zeolite Membranes for Coal Gasification Membrane Reactor Applications. In *Technical Report*, University of Colorado

98. Horn, M. (2004) *Fraunhofer Magazine* 1, 48.

99. Houghton, J.T.*, et al.* (2001) *Climate Change 2001: The Scientific Basis*. Cambridge University Press Cambridge.

100. Hu, S.*, et al.* (2014) Proton transport through one-atom-thick crystals. *Nature*516, 227–230.

101. Huertas, R.M.*, et al.* (2012) Preparation and gas separation properties of partially pyrolyzed membranes (PPMs) derived from copolyimides containing polyethylene oxide side chains. *J. Membr. Sci* 409, 200-211.

102. Iijima, S. and Ichihashi, T. (1986) Structural instability of ultrafine particles of metals. *Phys. Rev. Lett.* 56, 616.

103. Ismail, A.F.*, et al.* (2009) Transport and separation properties of carbon nanotube-mixed matrix membrane. *Sep and Purif Technol* 70, 12-26.

104. Iverson, C. (2009) Cow digestive tract. Science-Art http://www.science-art.com/image/?id=4245#.UV4pRZNkN8F.

105. Jami, E.*, et al.* (2013) Exploring the bovine rumen bacterial community from birth to adulthood. *ISME J.* 7, 1069-1079.

106. Jia, M.-D.*, et al.* (1992) Preparation and characterization of thin-film zeolite–PDMS composite membranes. *J. Membr. Sci.* 73, 119-128.

107. Jiang, D.*, et al.* (2009) Porous graphene as the ultimate membrane for gas separation. *Nano Lett.* 9, 4019-4024.

108. Jin, M.*, et al.* (2005) Super‐hydrophobic PDMS surface with ultra‐low adhesive force. *Macromol. Rapid Comm.* 26, 1805-1809.

109. John, D.*, et al.* (2003) Carbon dioxide-induced plasticization of polyimide membranes: pseudo-equilibrium relationships of diffusion, sorption, and swelling. *Macromolecules* 36, 6433-6441.

110. José, N.M.*, et al.* (2005) Partially pyrolysed membranes based on PDMS: Analysis of the morphological changes by SAXS/WAXS. pp. 929, HASYLAB.

111. Ju, H.*, et al.* (2010) Characterization of sodium chloride and water transport in crosslinked poly (ethylene oxide) hydrogels. *J. Membr. Sci.* 358, 131-141.

112. Jullok, N.*, et al.* (2013) A Biologically Inspired Hydrophobic Membrane for Application in Pervaporation. *Langmuir* 29, 1510-1516.

113. Kaali, P.*, et al.* (2010) Antimicrobial properties of Ag^{+} loaded zeolite polyester polyurethane and silicone rubber and long-term properties after exposure to*in vitro* ageing. *Polym. Degrad. Stabil.* 95, 1456-1465.

114. Kalantar-zadeh, K. and Fry, B. (2007) *Nanotechnology Enabled Sensors*. Springer.

115. Kalantar-Zadeh, K.*, et al.* Australian Government. Gas sensor nanocomposites membranes, 2014903506.

116. Kansy, J. (1996) Microcomputer program for analysis of positron annihilation lifetime spectra. *Nucl. Intrum. Meth. A* 374, 235-244.

117. Kim, H.*, et al.* (2010) Graphene/polymer nanocomposites. *Macromolecules* 43, 6515-6530.

118. Kim, H.W.*, et al.* (2013) Selective gas transport through few-layered graphene and graphene oxide membranes. *Science* 342, 91-95.

119. Kim, I.-H. and Jeong, Y.G. (2010) Polylactide/exfoliated graphite nanocomposites with enhanced thermal stability, mechanical modulus, and electrical conductivity. *J. Polym. Sci. B: Polym. Phys.* 48, 850-858.

120. Kim, K.H.*, et al.* (2012) A review of breath analysis for diagnosis of human health. *Trends Analyt. Chem.* 33, 1-8.

121. Kim, S.*, et al.* (2007) Scalable fabrication of carbon nanotube/polymer nanocomposite membranes for high flux gas transport. *Nano Lett* 7, 2806-2811.

122. Kim, S.*, et al.* (2006) Poly(imide siloxane) and carbon nanotube mixed matrix membranes for gas separation. *Desalination* 192, 330-339.

123. Kleiber, M.*, et al.* (1943) Bloat in Cattle and Composition of Rumen Gases. *Journal Dairy Science* 26, 929-933.

124. Koros, W.J. and Hellums, M.W. (1989) *Encyclopedia of Polymer Science and Engineering*. Wiley.

125. Korotcenkov, G. (2007) Metal oxides for solid-state gas sensors: What determines our choice? *Mater. Sci. Eng. B Solid State Mater. Adv. Technol.* 139, 1-23.

126. Korotcenkov, G.*, et al.* (2009) Review of electrochemical hydrogen sensors. *Chem. Rev.* 109, 1402-1433.

127. Kozakiewicz, J. and Przybylski, J. (2003) WAXS and SAXS study of (m) TMXDI-PDMS siloxane-urethaneureas. *Fibres Text. East. Eur* 11, 44.

128. Kruse, J.*, et al.* (2007) Free volume in C60 modified PPO polymer membranes by positron annihilation lifetime spectroscopy. *J. Phys. Chem. B* 111, 13914-13918.

129. Kurian, A.*, et al.* (2010) Unusual surface aging of poly(dimethylsiloxane) elastomers. *Macromolecules* 43, 2438-2443.

130. Lai, J.J.*, et al.* (2011) MEMS integrated narrow band infrared emitter and detector for infrared gas sensor. *J. Phys. Conf. Ser.* 276, 012129

131. Lalezari, D. (2012) Gastrointestinal pH profile in subjects with irritable bowel syndrome. *Ann. Gastroenterol.* 25, 333-337.

132. Lansdown, A. (2006) Silver in health care: antimicrobial effects and safety in use. In *Biofunctional Textiles and the Skin* (Hipler, U.-C. and Elsner, P., eds), pp. 17-34, Karger.

133. Late, D.J.*, et al.* (2013) Sensing behavior of atomically thin-layered MoS_2 transistors. *ACS Nano* 7, 4879-4891.

134. Lebeaux, D.*, et al.* (2013) From *in vitro* to *in vivo* models of bacterial biofilm-related infections. *Pathogens* 2, 288-356.

135. Lebrun, L.*, et al.* (2006) Elaboration and characterisation of PDMS-$HTiNbO_5$nanocomposite membranes. *Eur. Polym. J* 42, 1975-1985.

136. Lee, C.*, et al.* (2008) Measurement of the elastic properties and intrinsic strength of monolayer graphene. *Science* 321, 385-388.

137. Lee, D.S.*, et al.* (1992) Gas transport in polyurethane-polystyrene interpenetrating polymer network membranes. II. Effect of crosslinked state and annealing. *J. Membr. Sci.* 75, 15-27.

138. Leenaerts, O.*, et al.* (2008) Graphene: A perfect nanoballoon. *Appl. Phys. Lett.* 93, 193107.

139. Leenaerts, O., *et al.* (2009) Water on graphene: Hydrophobicity and dipole moment using density functional theory. *Phys. Rev. B* 79, 235440.

140. Li, H., *et al.* (1999) Design and synthesis of an exceptionally stable and highly porous metal-organic framework. *Nature* 402, 276-279.

141. Li, H., *et al.* (2012) From bulk to monolayer MoS2: evolution of Raman scattering. *Adv. Funct. Mater.* 22, 1385-1390.

142. Li, L., *et al.* (2004) Composite PDMS membrane with high flux for the separation of organics from water by pervaporation. *J. Membr. Sci* 243, 177-187.

143. Li, Y., *et al.* (2013) Recent advances in the fabrication of advanced composite membranes. *J. Mater. Chem. A* 1, 10058-10077.

144. Li, Y., *et al.* (2013) Improving the flux of PDMS membranes via localized heating through incorporation of gold nanoparticles. *J. Membr. Sci.* 428, 63-69.

145. Lin, H. and Freeman, B.D. (2005) Materials selection guidelines for membranes that remove CO_2 from gas mixtures. *J. Mol. Struct.* 739, 57-74.

146. Lin, H., *et al.* (2006) Transport and structural characteristics of crosslinked poly (ethylene oxide) rubbers. *J. Membr. Sci.* 276, 145-161.

147. Linden, D.R. (2014) Hydrogen sulfide signaling in the gastrointestinal tract. *Antioxid. Redox Signal.* 20, 818-830.

148. Lisensky, G. (2008) Cross-linking of Polydimethylsiloxane. The Board of Regents of the University of Wisconsin System. http://education.mrsec.wisc.edu/nanolab/PDMS/PDMS.html.

149. Liu, C. (2007) Recent developments in polymer MEMS. *Adv. Mater.* 19, 3783-3790.

150. Liu, L., *et al.* (2007) Paperlike thermochromic display. *Appl. Phys. Lett.* 90, -.

151. Liu, P.-T., *et al.* (2006) Activation of carbon nanotube emitters by using supercritical carbon dioxide fluids with propyl alcohol. *Electrochem. Solid-State Lett* 9, 124-126.

152. Liu, X., *et al.* (2012) A survey on gas sensing technology. *Sensors* 12, 9635-9665.

153. Lötters, J., *et al.* (1997) The mechanical properties of the rubber elastic polymer polydimethylsiloxane for sensor applications. *J. Micromech. Microeng.* 7, 145.

154. Lozupone, C.A., *et al.* (2012) Diversity, stability and resilience of the human gut microbiota. *Nature* 489, 220-230.

155. Lue, S.J., *et al.* (2010) Tailoring permeant sorption and diffusion properties with blended polyurethane/poly (dimethylsiloxane)(PU/PDMS) membranes. *J. Membr. Sci* 356, 78-87.

156. Lundberg, J.O., *et al.* (2005) Technology insight: Calprotectin, lactoferrin and nitric oxide as novel markers of inflammatory bowel disease. *Nat. Clin. Pract. Gastroenterol. Hepatol.* 2, 96-102.

157. Maggos, T., *et al.* (2007) Application of photocatalytic technology for NO_x removal. *App. Phys. A* 89, 81-84.

158. Maji, D., *et al.* (2012) Study of hydrophilicity and stability of chemically modified PDMS surface using piranha and KOH solution. *Surf. Interface Anal* 44, 62-69.

159. Makhluf, S., *et al.* (2005) Microwave-assisted synthesis of nanocrystalline MgO and its use as a bacteriocide. *Adv. Func. Mater.*15, 1708-1715.

160. Mannoor, M.S., *et al.* (2012) Graphene-based wireless bacteria detection on tooth enamel. *Nat. Commun.* 3, 763.

161. Mansoori, S., *et al.* (2011) CO_2 Selectivity of a New PDMS/PSF Membrane Prepared at Different Conditions. *J. Membr. Sci. Technol* 1, 2.

162. Marinkovic, S.N. (2008) Review carbon nanotubes. *J. Serb. Chem. Soc.* 8–9, 891–913.

163. Mark, J. and Sullivan, J. (1977) Model networks of end‐linked polydimethylsiloxane chains. I. Comparisons between experimental and theoretical values of the elastic modulus and the equilibrium degree of swelling. *J. Chem. Phys.* 66, 1006-1011.

164. Masse, A., *et al.* (2000) Prevention of pin track infection in external fixation with silver coated pins: clinical and microbiological results. *J.biomed. mater.res.* 53, 600-604.

165. Mata, A., *et al.* (2005) Characterization of polydimethylsiloxane (PDMS) properties for biomedical micro/nanosystems. *Biomed. Microdevices* 7, 281-293.

166. Mathews, S.M., *et al.* (2006) Prevention of bacterial colonization of contact lenses with covalently attached selenium and effects on the rabbit cornea. *Cornea* 25, 806-814.

167. Mathias, U. (2006) Advanced functional polymer membranes. *Polymer* 47, 2217–2262.

168. McKay, L.F., *et al.* (1985) Methane excretion in man - A study of breath, flatus, and faeces. *Gut* 26, 69-74.

169. McNally, T., *et al.* (2005) Polyethylene multiwalled carbon nanotube composites. *Polymer* 46, 8222-8232.

170. Medani, M., *et al.* (2011) Emerging role of hydrogen sulfide in colonic physiology and pathophysiology. *Inflamm. Bowel Dis.* 17, 1620-1625.

171. Merkel, T., *et al.* (2000) Gas sorption, diffusion, and permeation in poly(dimethylsiloxane). *J. Polym. Sci. B: Polym. Phys.* 38, 415-434.

172. Merkel, T., *et al.* (2002) Ultrapermeable, reverse-selective nanocomposite membranes. *Science* 296, 519-522.

173. Merkel, T.C., *et al.* (2001) Mixed-gas permeation of syngas components in poly(dimethylsiloxane) and poly(1-Trimethylsilyl-1-Propyne) at elevated temperatures. *J. Membr. Sci* 191, 85-94.

174. Moaddeb, M. and Koros, W.J. (1997) Gas transport properties of thin polymeric membranes in the presence of silicon dioxide particles. *J.Membr.Sci.* 125, 143-163.

175. Mokwa, W. and Schnakenberg, U. (2001) Micro-transponder systems for medical applications. *IEEE Intsru. Meas. Mag.* 50, 1551-1555.

176. Moore, T.T. and Koros, W.J. (2005) Non-Ideal effects in organic–inorganic materials for gas separation membranes. *J. Mol. Struct.* 739, 87-98.

177. Morones, J.R., *et al.* (2005) The bactericidal effect of silver nanoparticles. *Nanotechnology* 16, 2346.

178. Morra, M., *et al.* (1990) On the aging of oxygen plasma-treated polydimethylsiloxane surfaces. *J Colloid Interf Sci* 137, 11-24.

179. Mouri, S., *et al.* (2013) Tunable Photoluminescence of Monolayer MoS_2 via Chemical Doping. *Nano Lett.* 13, 5944-5948.

180. Muehlhoff, L.*, et al.* (1986) Comparative electron spectroscopic studies of surface segregation on SiC(0001) and SiC(0001). *J Appl Phys* 60, 2842-2853.

181. Nakagawa, T.*, et al.* (2002) Morphology and gas permeability in copolyimides containing polydimethylsiloxane block. *J. Membr. Sci.* 206, 149-163.

182. Nakatsuka, S. and Andrady, A.L. (1992) Permeability of vitamin B‐12 in chitosan membranes. Effect of crosslinking and blending with poly (vinyl alcohol) on permeability. *J. Appl. Polym. Sci.* 44, 17-28.

183. Narimissa, E.*, et al.* (2012) Influence of nano-graphite platelet concentration on onset of crystalline degradation in polylactide composites. *Polym. Degrad. Stab*97, 829–832.

184. Newaz, A.*, et al.* (2013) Electrical control of optical properties of monolayer MoS_2. *Solid State Commun.* 155, 49-52.

185. Ng, L.Y.*, et al.* (2013) Polymeric membranes incorporated with metal/metal oxide nanoparticles: a comprehensive review. *Desalination* 308, 15-33.

186. Nguyen, E.*, et al.* (2013) Assessment of a Raman micro-spectroscopy/microfluidics unit using a model E. coli/glucose bio-system. In *Nano/Molecular Medicine and Engineering (NANOMED), 2013 IEEE 7th International Conference on*, pp. 157-162, IEEE.

187. Nguyen, E.P.*, et al.* (2014) Investigation of two-solvent grinding assisted liquid phase exfoliation of layered MoS2. *Chem. Mater.* 27, 53-59.

188. Nicholson, J.K.*, et al.* (2012) Host-gut microbiota metabolic interactions. *Science* 336, 1262-1267.

189. Nour, M.*, et al.* (2013) CNT/PDMS composite membranes for H_2 and CH_4 gas separation. *Int. J. Hydrogen Energ.* 38, 10494-10501.

190. Nour, M.*, et al.* (2014) Silver nanoparticle/PDMS nanocomposite catalytic membranes for H_2S gas removal. *J. Memb. Sci.* 470, 346-355.

191. Nour, M.*, et al.* (2012) Nanocomposite carbon-PDMS membranes for gas separation. *Sensor. Actuat. B-Chem.* 161, 982-988.

192. Novak, B.M. (1993) Hybrid nanocomposite materials—between inorganic glasses and organic polymers. *Adv Mater* 5, 422-433.

193. Novoselov, K.S.*, et al.* (2004) Electric field effect in atomically thin carbon films. *Science* 306, 666-669.

194. Nyczyk, A.*, et al.* (2012) Cross-Linking of linear vinylpolysiloxanes by hydrosilylation – FTIR spectroscopic studies. *Vib. Spectrosc* 59, 1-8.

195. O'Neill, A.*, et al.* (2012) Preparation of high concentration dispersions of exfoliated MoS2 with increased flake size. *Chem. Mater.* 24, 2414-2421.

196. Osswald, S.*, et al.* (2007) Monitoring oxidation of multiwalled carbon nanotubes by Raman spectroscopy. *J Raman Spectrosc* 38, 728-736.

197. Ozbas, B.*, et al.* (2012) Multifunctional elastomer nanocomposites with functionalized graphene single sheets. *Journal of Polymer Science Part B: Polymer Physics* 50, 910-916.

198. Ozhikandathil, J.*, et al.* (2011) Synthesis and characterization of silver-PDMS nanocomposite for the biosensing applications. In *Photonics North 2011, International Society for Optics and Photonics*, pp. 800707-800706.

199. Pal, S.*, et al.* (2007) Does the Antibacterial Activity of Silver Nanoparticles Depend on the Shape of the Nanoparticle? A Study of the Gram-Negative Bacterium Escherichia coli. *Appl. Environ. Microbiol.* 73, 1712-1720.

200. Pan, G. and Wang, L. (2012) Swallowable wireless capsule endoscopy: Progress and technical challenges. *Gastroenterol. Res. Pract.* 2012, 841691.

201. Pandey, P. and Chauhan, R.S. (2001) Membranes for gas separation. *Prog. Polym. Sci.* 26, 853-893.

202. Park, N.H.*, et al.* (2014) Calorimetric thermoelectric gas sensor for the detection of hydrogen, methane and mixed gases. *Sensors* 14, 8350-8362.

203. Park, S.S.*, et al.* (2009) Dual electrochemical microsensor for simultaneous measurements of nitric oxide and oxygen: Fabrication and characterization. *Electrochem Commun* 11, 2040-2043.

204. Pimentel, M.*, et al.* (2013) Gas and the microbiome. *Curr. Gastroenterol. Rep.* 15, 356.

205. Pinnau, I. and He, Z. (2004) Pure and Mixed-Gas Permeation Properties of Polydimethylsiloxane for Hydrocarbon/Methane and Hydrocarbon/Hydrogen Separation. *J. Membr. Sci* 244, 227-233.

206. Probert, C.S.J. (2011) Role of faecal gas analysis for the diagnosis of IBD. *Biochem. Soc. Trans.* 39, 1079-1080.

207. Queiroz, D.P. and Norberta de Pinho, M. (2005) Structural Characteristics and Gas Permeation Properties of Polydimethylsiloxane/Poly(propylene oxide) Urethane/Urea Bi-Soft Segment Membranes. *Polymer* 46, 2346-2353.

208. Ramanathan, T.*, et al.* (2008) Functionalized graphene sheets for polymer nanocomposites. *Nature Nanotech.* 3, 327-331.

209. Rao, H.-X.*, et al.* (2007) Preparation and Oxygen/Nitrogen Permeability of PDMS Crosslinked Membrane and PDMS/Tetraethoxysilicone Hybrid Membrane. *J. Membr. Sci* 303, 132-139.

210. Rattray, N.J.W.*, et al.* (2014) Taking your breath away: metabolomics breathes life in to personalized medicine. *Trends Biotechnol.* 32, 538-548.

211. Rivera, L.R.*, et al.* (2011) The involvement of nitric oxide synthase neurons in enteric neuropathies. *Neurogastroenterol. Motil.* 23, 980-988.

212. Robeson, L.M. (1991) Correlation of separation factor versus permeability for polymeric membranes. *J. Membr. Sci.* 62, 165-185.

213. Robeson, L.M. (1999) Polymer Membranes for Gas Separation. *Curr. Opin. Solid St. M* 4, 549-552.

214. Russell, A.D. and Hugo, W.B. (1994) 7 Antimicrobial Activity and Action of Silver. In *Progress in Medicinal Chemistry* (Ellis, G.P. and Luscombe, D.K., eds), pp. 351-370, Elsevier.

215. Ryczkowski, J. (2001) IR spectroscopy in catalysis. *Catal. Today* 68, 263-381.

216. S. Costa, E.B.-P., M. Kruszynska, A. Bachmatiuk, R. J. Kalenczu (2008) Characterization of carbon nanotubes by Raman spectroscopy. *Materials Science-Poland* 26, 433-441.

217. Saad, R.J. and Hasler, W.L. (2011) A technical review and clinical assessment of the wireless motility capsule. *Gastroenterol. Hepato.* 7, 795-804.

218. Sadrzadeh, M.*, et al.* (2009) Effect of operating parameters on pure and mixed gas permeation properties of a synthesized composite PDMS/PA membrane. *J. Membr. Sci* 342, 327-340.

219. Safadi, B.*, et al.* (2002) Multiwalled carbon nanotube polymer composites: Synthesis and characterization of thin films. *J Appl Polym Sci* 84, 2660-2669.

220. Sahakian, A.B.*, et al.* (2010) Methane and the gastrointestinal tract. *Digest. Dis. Sci.* 55, 2135-2143.

221. Saidi, I.S.*, et al.* (1999) *In vivo* resistance to bacterial biofilm formation on tympanostomy tubes as a function of tube material. *Otolaryngol Head Neck Surg.* 120, 621-627.

222. Sanders, E.S. (1988) Penetrant-induced plasticization and gas permeation in glassy polymers. *J.Membr. Sci.* 37, 63-80.

223. Saner, B.*, et al.* (2010) Utilization of multiple graphene layers in fuel cells. 1. An improved technique for the exfoliation of graphene-based nanosheets from graphite. *Fuel* 89, 1903-1910.

224. Sanip, S.M.*, et al.* (2011) Gas separation properties of functionalized carbon nanotubes mixed matrix membranes. *Sep. Purif. Technol.* 78, 208-213.

225. Schiavon, M.*, et al.* (2002) Investigation on kinetics of thermal decomposition in polysiloxane networks used as precursors of silicon oxycarbide glasses. *J. Non-Cryst. Solids* 304, 92-100.

226. Schmolke, H.*, et al.* (2010) Polyelectrolyte multilayer surface functionalization of poly(dimethylsiloxane) (PDMS) for reduction of yeast cell adhesion in microfluidic devices. *Biomicrofludics* 4, 044113.

227. Scholz, J.*, et al.* (2005) Investigations on fabrics coated with precious metals using the magnetron sputter technique with regard to their anti-microbial properties. *Surf. Coat. Tech.* 192, 252-256.

228. Scott, A.*, et al.* (2010) A simple water-based synthesis of Au nanoparticle/PDMS vomposites for water purification and targeted drug release. *Macromol. Chem. Physic.* 211, 1640-1647.

229. Serp, P.*, et al.* (2003) Carbon nanotubes and nanofibers in catalysis. *Appl. Cata.l A-Gen.* 253, 337-358.

230. Shah, V.M.*, et al.* (1993) Solubility of carbon doxide, methane and propane in silicone polymers. effect of polymer backbone chains. *J. Polym. Sci. B: Polym. Phys* 31, 313-317.

231. Shepherd, S.F.*, et al.* (2014) The use of a gas chromatograph coupled to a metal oxide sensor for rapid assessment of stool samples from irritable bowel syndrome and inflammatory bowel disease patients. *J. Breath Res.* 8, 026001

232. Shin, W. (2014) Medical applications of breath hydrogen measurements *Anal. Bioanal. Chem.* 406, 3931-3939.

233. Shin, W.*, et al.* (2009) Fabrication of thermoelectric gas sensors on micro-hotplates. *Sens Actuators B Chem.* 139, 340-345.

234. Shin, Y.J.*, et al.* (2010) Surface-energy engineering of graphene. *Langmuir* 26, 3798-3802.

235. Sia, S.K. and Whitesides, G.M. (2003) Microfluidic devices fabricated in poly (dimethylsiloxane) for biological studies. *Electrophoresis* 24, 3563-3576.

236. Simon, P.*, et al.* (2014) Where do batteries end and supercapacitors begin? *Science* 343, 1210-1211.

237. Singh, A.*, et al.* (1998) Pure and mixed gas acetone/nitrogen permeation properties of polydimethylsiloxane (PDMS). *J. Polym. Sci. B: Polym. Phys* 36, 289-301.

238. Skoog, D.A.*, et al.* (2007) *Principles of Instrumental Analysis*. Thomson Higher Education.

239. Skoog, D.A.*, et al.* (2013) *fundamentals of analytical chemistry*. Cengage Learning.

240. Sobko, T.*, et al.* (2005) Gastrointestinal bacteria generate nitric oxide from nitrate and nitrite. *Nitric Oxide-Biol. Ch.* 13, 272-278.

241. Sommer, F. and Bäckhed, F. (2013) The gut microbiota-masters of host development and physiology. *Nat. Rev. Microbiol.* 11, 227-238.

242. Sommer, S.*, et al.* (2010) A preliminary study on the properties and fouling-release performance of siloxane–polyurethane coatings prepared from poly (dimethylsiloxane)(PDMS) macromers. *Biofouling* 26, 961-972.

243. Stafie, N.*, et al.* (2005) Effect of PDMS cross-linking degree on the permeation performance of PAN/PDMS composite nanofiltration membranes. *Sep. Purif. Technol.* 45, 220-231.

244. Stern, S.A.*, et al.* (1963) Performance of a versatile variable-volume permeability cell. comparison of gas permeability measurements by the variable-volume and variable-pressure Methods. *J. Appl. Polym. Sci* 7, 2035-2051.

245. Stern, S.A.*, et al.* (1987) Structure-permeability relationships in silicone polymers. *J. Polym. Sci. B: Polym. Phys* 25, 1263-1298.

246. Stetter, J.R. and Li, J. (2008) Amperometric gas sensors - A review. *Chem. Rev.* 108, 352-366.

247. Stoller, M.D.*, et al.* (2008) Graphene-based ultracapacitors. *Nano Lett.* 8, 3498-3502.

248. Suarez, F.L. and Levitt, M.D. (2000) An understanding of excessive intestinal gas. *Curr. Gastroenterol. Rep.* 2, 413-419.

249. Tao, S. (1972) Positronium annihilation in molecular substances. *J. Chem. Phys* 56, 5499.

250. Thompson, W.G.*, et al.* (1999) Functional bowel disorders and functional abdominal pain. *Gut* 45, II43-II47.

251. Tieszer, C.*, et al.* (1998) XPS and SEM detection of surface changes on 64 ureteral stents after human usage. *J. Biomed. Mater. Res.* 43, 321-330.

252. Tokunaga, O. and Suzuki, N. (1984) Radiation chemical reactions in NO_x and SO_2 removals from flue gas. *Radiat. Phys. Chem.* 24, 145-165.

253. Triantafyllou, K.*, et al.* (2014) Methanogens, methane and gastrointestinal motility. *Neurogastroenterol. Motil.* 20, 31-40.

254. Tsai, M.H.*, et al.* (2012) Transparent polyimide nanocomposites with improved moisture barrier using graphene. *Polym. Int.* 62, 1302-1309.

255. Tsujita, Y.*, et al.* (1993) Structure and gas permeability of siloxane-imide block copolymer membranes: 1. Effect of siloxane content. *Polymer* 34, 2597-2601.

256. Uyanik, N.*, et al.* (1999) Synthesis and characterization of poly (dimethyl siloxane) containing poly (vinyl pyrrolidinone) block copolymers. *J. Appl. Polym. Sci.* 71, 1915-1922.

257. Veldsink, J.*, et al.* (1994) An experimental study of diffusion and convection of multicomponent gases through catalytic and non-catalytic membranes. *J. Membr. Sci.* 92, 275-291.

258. Vijay, Y. (2002) The titanium-coated polymeric membranes for hydrogen recovery. *Int J Hydrogen Energ* 27, 905-908.

259. Walton, C.*, et al.* (2013) Analysis of volatile organic compounds of bacterial origin in chronic gastrointestinal diseases. *Inflamm. Bowel Dis.* 19, 2069-2078.

260. Wang, H.*, et al.* (2007) Preparation and characterization of silver nanocomposite textile. *J. Coat. Technol. Res.* 4, 101-106.

261. Wang, Q.H.*, et al.* (2012) Electronics and optoelectronics of two-dimensional transition metal dichalcogenides. *Nat. Nano* 7, 699-712.

262. Wang, Y.*, et al.* (2009) Application of graphene-modified electrode for selective detection of dopamine. *Electrochemistry Communications* 11, 889-892.

263. Weinkauf, D. and Paul, D. (1990) Effects of structural order on barrier properties. *ACS Sym. Ser.* 423, 61-91.

264. Wen, Y.*, et al.* (2011) Preparation and visible light photocatalytic activity of Ag/TiO_2/graphene nanocomposite. *Nanoscale* 3, 4411-4417.

265. Willey, J. (2008) *Prescott, Harley, and Klein's Microbiology-7th international ed./Joanne M. Willey, Linda M. Sherwood, Christopher J. Woolverton*. New York [etc.]: McGraw-Hill Higher Education.

266. Wu, G.D.*, et al.* (2011) Linking long-term dietary patterns with gut microbial enterotypes. *Science* 334, 105-108.

267. Xiangli, F.*, et al.* (2008) Optimization of preparation conditions for polydimethylsiloxane(PDMS)/ceramic composite pervaporation membranes using response surface methodology. *J. Membr. Sci* 311, 23-33.

268. Xiao, D.Q.*, et al.* (2002) Chemical modification of the surface of poly(dimethylsiloxane) by atom-transfer radical polymerization of acrylamide. *Langmuir* 18, 9971-9976.

269. Xu, T.*, et al.* (2014) Electrochemical sensors for nitric oxide detection in biological applications. *Electroanal.* 26, 449-468.

270. Xu, W.W.*, et al.* (2011) Extreme hardening of PDMS thin films due to high compressive strain and confined thickness. *Langmuir* 27, 8470-8477.

271. Y.-H. Liu, B.Y., Z.-G. Shao, D. Xing, H. Zhang (2006) *Solid-State Lett*.,588.

272. Yacamán, M.J.*, et al.* (2001) Structure shape and stability of nanometric sized particles. *J. Vac. Sci. Technol. B* 19, 1091-1103.

273. Yao, C.K.*, et al.* (2014) Ranking fermentability of fibre supplements using a gas production screening tool. *Proc. Nutr. Soc. Australia.* 38, 118.

274. Yeh, G.S.Y.*, et al.* (1976) Annealing effects of polymers and their underlying molecular Mechanisms. *Polymer* 17, 309-318.

275. Yoo, K.P.*, et al.* (2011) Fabrication, characterization and application of a microelectromechanical system (MEMS) thermopile for non-dispersive infrared gas sensors. *Meas. Sci. Technol.* 22, 115206.

276. Yoo, S.H.*, et al.* (2006) Mechanical and swelling properties of PDMS interpenetrating polymer networks. *Polymer* 47, 6226-6235.

277. Yuce, M.R. and Dissanayake, T. (2012) Easy-to-swallow wireless telemetry. *IEEE Micow. Mag.* 13, 90-101.

278. Yue, Q.*, et al.* (2013) Adsorption of gas molecules on monolayer MoS_2 and effect of applied electric field. *Nanoscale Res. Lett.* 8, 1-7.

279. Zeng, Y.*, et al.* (2010) Increasing the electrical conductivity of carbon nanotube/polymer composites by using weak nanotube–polymer interactions. *Carbon* 48, 3551-3558.

280. Zhan, X. (2009) Pervaporation properties of PDMS membranes cured with different cross-linking reagents for ethanol concentration from aqueous solutions. *Chinese J Polym Sci* 27, 533.

281. Zhang, H.-B.*, et al.* (2002) Raman spectra of MWCNTs and MWCNT-based H2-adsorbing system. *Carbon* 40, 2429-2436.

282. Zhao, S.*, et al.* (2014) Gas adsorption on MoS_2 monolayer from first-principles calculations. *Chem. Phys. Lett.* 595–596, 35-42.

283. Zhao, W.*, et al.* (2012) Evolution of electronic structure in atomically thin sheets of WS_2 and WSe_2. *ACS Nano* 7, 791-797.

284. Zimmerman, C.M.*, et al.* (1997) Tailoring mixed matrix composite membranes for gas separations. *J. Membr. Sci* 137, 145-154.